Parallel 3-D Method of Characteristics with Linear Source and Advanced Transverse Integration

by

Andrew P. Fitzgerald

A dissertation submitted in partial fulfillment
of the requirements for the degree of
Doctor of Philosophy
(Nuclear Engineering and Radiological Sciences)
in the University of Michigan
2019

Doctoral Committee:

Professor Brendan Kochunas, Chair,
Professor Thomas Downar,
Professor Edward Larsen,
Professor Venkat Raman, Dr. Rodolfo Ferrer,

apfitzge@umich.edu
ORCID ID: 0000-0002-4066-0949

2019

TABLE OF CONTENTS

List of Algorithms

LIST OF APPENDICES

LIST OF ABBREVIATIONS

MoC Method of Characteristics

FS flat source

LS linear source

FSA flat-source approximation

LSA linear-source approximation

FSMoC flat-source method of characteristics

LSMoC linear-source method of characteristics

LIFA linear isotropic flat anisotropic

CASL Consortium for the Advanced Simulation of Light Water Reactors

LWR Light Water Reactor

NEAMS Nuclear Energy Advanced Modeling and Simulation Program

PDE Partial Differential Equation

ODE Ordinary Differential Equation

P_N Spherical Harmonics

SSpherical Harmonics (P_N) Simplified P_N

CP Collision Probability

CDP method of Characteristic Direction Probabilities

S_N Discrete Ordinates

NDA non-linear diffusion acceleration

CMFD coarse mesh finite-difference

T/H thermal-hydraulic

TCP0 transport-corrected P_0

DNPL direct neutron path linking

MRMB memory reduction technique for macroband

MRT modular ray-tracing

VERA Virtual Environment for Reactor Analysis

UO_2 uranium oxide

CPU central processing unit

GPU graphics processing unit

GPGPU general purpose graphics processing unit

RSB recursive spectral bisection

RIB recursive intertial bisection

REB recursive expansion bisection

SOI sphere of influence

MMR maximum-to-minimum ratio

ARA axially and radially aligned

RA radially aligned

UR unrestricted

B&W Babcox and Wilcox

FLOP floating point operation

EFPD effective full power days

GWDMT gigawatt-days per metric ton heavy metal

pcm per cent mille

HFP hot full power

CTF COBRA-TF

KAIST Korea Advanced Institute of Science and Technology

KAERI Korea Atomic Energy Research Institute

CHAPTER 1

Introduction

1.1 Motivation

Computer simulations have played an important role in the design and analysis of nuclear reactor systems over the past 60 years [1]. The methods used by these simulations have always been limited by the available computational resources; as such, in the 1950's two-group diffusion theory was used as a basis for simulation tools [1]. As computers became more powerful, multigroup diffusion calculations became the method of choice for Light Water Reactor (LWR) design calculations.

More accurate and detailed simulation tools allow for designs to have higher power density, and thus be more profitable, without compromising safety. However, computational resources have always limited the level of detail of simulation tools. Exponential increases in computing power, and high-performance computing clusters have made whole-core transport calculations possible [2–9]. Programs such as Consortium for the Advanced Simulation of Light Water Reactors (CASL) and Nuclear Energy Advanced Modeling and Simulation Program (NEAMS) have focused on development of modern advanced simulation tools to address certain challenge problems. Large computing clusters are generally unavailable to reactor analysts in industry, and so using direct whole-core 3-D transport methods is not common outside academia or national laboratories.

The "gold standard" of deterministic methods has been the 3-D Method of Characteristics (MoC) [10] due to its' ability to exactly model complicated geometries. At the time of writing, whole-core 3-D MoC calculations are generally not possible without use of large computing clusters. This is due to the large discretizations that are necessary for the neutron transport equation, which has a 6-dimensional phase space for steady-state eigenvalue problems. In the past decade, there has been renewed interest in making 3-D MoC more efficient and performant by using parallelism [11], modern graphics processing unit (GPU) architectures [7], and ray-tracing storage techniques [12, 13]. There has also been work done to make MoC faster by improving the efficiency of the calculations by using higher-order approximations [9, 14].

The bulk of this thesis work is comprised of three distinct, yet connected, topics, all with a focus

on improving the feasibility of 3-D MoC calculations. It is the author's opinion, that improving efficiency of 3-D MoC calculations should be the primary focus of current research, as it is not feasible for industry to use thousands of processors. Thus, two techniques are utilized as part of this thesis work: the linear-source approximation (LSA), and the macroray.

The LSA has been studied by other research groups [9, 14, 15], and has been worked on as part of this thesis project; specifically, this work has led to improvements of the method for stability in near-void regions [16], and efficiency in multi-physics simulations [17]. The LSA is an approximation that is used to improve MoC efficiency by reducing the number of computational cells required for accurate results.

The macroray is a new ray-tracing technique under development as part of this thesis work; this technique is an extension of the two-dimensional macroband [18] ray-tracing technique. This technique has been shown to reduce the number of characteristic rays required for accurate results in two-dimensional flat-source calculations [19, 20]. To the best of the author's knowledge, there have been no studies of this ray-tracing technique in three-dimensional ray-tracing calculations. Fewer characteristic rays results in more efficient calculations; the improvement in efficiency is expected to be more significant in 3-D calculations due to the square scaling of tracks with ray-spacing, rather than linear scaling in 2-D. Additionally, efficiency should be improved further by the linear source (LS) which allows for coarser cells and fewer track-segments.

The third contribution of this thesis is work in improving parallel efficiency. While large scale parallelism on thousands of processors may not be feasible for industry, some degree of parallelism is necessary for whole-core calculations due to memory constraints. An automated spatial decomposition scheme based on graph theory, is developed leading to significantly improved parallel efficiency [21, 22].

1.2 Outline

Bibliography

[1] G. C. Bilodeau et al. *PDQ: An IBM-704 Code to Solve the Two-dimensional Few-group Neutron-Diffusion Equations*. Tech. rep. Bettis Plant, Westinghouse Electrice Corporation, 1957.

[2] Kord Smith and Joel D. Rhodes. "CASMO-4 Characteristic Methods for Two-Dimensional PWR and BWR Core Calculations". In: *Transactions of the American Nuclear Society*. 2000.

[3] Richard Sanchez et al. "APOLLO2 Year 2010". In: *Journal of Nuclear Engineering and Technology* 42.5 (2010), pp. 474–499.

[4] Han Gyu Joo et al. "Methods and performance of a three-dimensional whole-core transport code DeCART". In: *PHYSOR 2004*. 2004, pp. 21–34. ISBN: 0894486837. URL: http://www.scopus.com/inward/record.url?eid=2-s2.0-22344449157{\&}partnerID=tZOtx3y1.

[5] Thomas M. Evans et al. "Denovo: A New Three-Dimensional Parallel Discrete Ordinates Code in SCALE". In: *Nuclear Technology* 171.2 (2010), pp. 171–200. ISSN: 0029-5450. DOI: 10.13182/nt171-171.

[6] W. S. Yang et al. "Neutronics modeling and simulation of sharp for fast reactor analysis". In: *Nuclear Engineering and Technology* 42.5 (2010), pp. 520–545. ISSN: 17385733. DOI: 10.5516/NET.2010.42.5.520.

[7] William Boyd et al. "The OpenMOC method of characteristics neutral particle transport code". In: *Annals of Nuclear Energy* 68 (2014), pp. 43–52. ISSN: 03064549. DOI: 10.1016/j.anucene.2013.12.012.

[8] Benjamin Collins et al. "Stability and accuracy of 3D neutron transport simulations using the 2D/1D method in MPACT". In: *Journal of Computational Physics* 326 (2016), pp. 612–628. ISSN: 10902716. DOI: 10.1016/j.jcp.2016.08.022.

[9] Geoffrey Alexander Gunow. "Full Core 3D Neutron Transport Simulation Using the Method of Characteristics with Linear Sources". Doctoral. Massachusetts Institute of Technology, 2018.

[10] J.R. Askew. *A Characteristics Formulation of the Neutron Transport Equation in Complicated Geometries*. 1972.

[11] Brendan Matthew Kochunas. "A Hybrid Parallel Algorithm for the 3-D Method of Characteristics Solution of the Boltzmann Transport Equation on High Performance Compute Clusters". Doctoral. University of Michigan, 2013, pp. 1–194.

[12] Daniele Sciannandrone, Simone Santandrea, and Richard Sanchez. "Optimized tracking strategies for step MOC calculations in extruded 3D axial geometries". In: *Annals of Nuclear Energy* 87 (2016), pp. 49–60. ISSN: 18732100. DOI: 10.1016/j.anucene.2015.05.014.

[13] Geoffrey Gunow et al. "Reducing 3D MOC Storage Requirements with Axial On- the-fly Ray Tracing". In: *Physics of Reactors 2016, PHYSOR 2016: Unifying Theory and Experiments in the 21st Century*. Sun Valley: American Nuclear Society, 2016. URL: http://hdl.handle.net/1721.1/109864{\%}0ACreative.

[14] Rodolfo M. Ferrer and Joel D. Rhodes. "A Linear Source Approximation Scheme for the Method of Characteristics". In: *Nuclear Science and Engineering* 182.2 (2016), pp. 151–165. ISSN: 0029-5639. DOI: 10.13182/NSE15-6.

[15] Rodolfo M. Ferrer and Joel D. Rhodes. "The linear source approximation and particle conservation in the Method of Characteristics for isotropic and anisotropic sources". In: *Annals of Nuclear Energy* 115 (2018), pp. 209–219. ISSN: 03064549. DOI: 10.1016/j.anucene.2018.01.023.

[16] Andrew Fitzgerald and Brendan Kochunas. "Fast Exponential Function Approximations for the Method of Characteristics with Linear Source". In: *Transactions of the American Nuclear Society*. Orlando, USA, 2018, pp. 645–648.

[17] Andrew P Fitzgerald, Brendan Kochunas, and Thomas Downar. "Improved Formulation of the Method of Characteristics with Linear Source for 2D/1D and Multiphysics Calculations". In: *M&C*. Portland, OR, 2019, pp. 1093–1103.

[18] Eduardo A. Villarino et al. "HELIOS: Angularly Dependent Collision Probabilities". In: *Nuclear Science and Engineering* 112.1 (1992), pp. 16–31. ISSN: 0029-5639. DOI: 10.13182/NSE112-16.

[19] Akio Yamamoto et al. "Non-Equidistant Ray Tracing for the Method of Characteristics". In: *M&C 2005* (2005), pp. 1–10.

[20] François Févotte, Simone Santandrea, and Richard Sanchez. "Advanced Transverse Integration for the Method of Characteristics". In: *M&C 2007*. 2007, pp. 1–12. ISBN: 0894480596.

[21] Andrew Fitzgerald et al. “Automated Decomposition of a Structured Grid”. In: *Transactions of the American Nuclear Society*. Vol. 117. Washington D.C., 2017, pp. 731–734.

[22] Andrew P Fitzgerald et al. “Spatial decomposition of structured grids for nuclear reactor simulations”. In: *Annals of Nuclear Energy* 132 (2019), pp. 686–701. ISSN: 0306-4549. DOI: 10.1016/j.anucene.2019.06.054.

CHAPTER 2

Neutron Transport Theory

In this chapter, the basic theory behind the neutron transport equation, and the numerical methods used to solve it are introduced.

2.1 Neutron Transport Equation

The mean behavior of neutrons in a (steady-state) system are described by the Boltzmann transport equation:

$$\begin{aligned}\Big[\widehat{\boldsymbol{\Omega}}\cdot\boldsymbol{\nabla}+\Sigma_t(\boldsymbol{x},E)\Big]\psi(\boldsymbol{x},\widehat{\boldsymbol{\Omega}},E)=&\\ \frac{1}{4\pi}\Bigg[&Q(\boldsymbol{x},\widehat{\boldsymbol{\Omega}},E)\\ &+\int_0^\infty\int_{4\pi}\Sigma_s(\boldsymbol{x},\widehat{\boldsymbol{\Omega}}'\cdot\widehat{\boldsymbol{\Omega}},E'\to E)\psi(\boldsymbol{x},\widehat{\boldsymbol{\Omega}}',E')\,\mathrm{d}\Omega'\,\mathrm{d}E'\\ &+\chi(\boldsymbol{x},E)\int_0^\infty\nu\Sigma_f(\boldsymbol{x},E')\int_{4\pi}\psi(\boldsymbol{x},\widehat{\boldsymbol{\Omega}}',E')\,\mathrm{d}\Omega'\,\mathrm{d}E'\Bigg],\\ \forall\boldsymbol{x},\quad\forall\widehat{\boldsymbol{\Omega}}\in 4\pi,\quad\forall E\in[0,\infty),\quad\forall t\geq 0,&\end{aligned}\tag{2.1}$$

where $\boldsymbol{x}$ is the position vector, $\widehat{\boldsymbol{\Omega}}$ is the direction vector, E is the neutron energy, Σ quantities are the macroscopic cross sections, ψ is the angular flux, ν is the average number of neutrons produced per fission, and χ is the fission neutron energy spectrum.

The position vector, $\boldsymbol{x}$, is a column vector of the spatial coordinates:

$$\boldsymbol{x}\equiv\begin{bmatrix}x\\y\\z\end{bmatrix}.\tag{2.2}$$

The direction vector, $\widehat{\mathbf{\Omega}}$, is a column unit-vector which gives the direction of flight for neutrons, and is defined by

$$\widehat{\mathbf{\Omega}} \equiv \begin{bmatrix} \Omega_x \\ \Omega_y \\ \Omega_z \end{bmatrix} = \begin{bmatrix} \sqrt{1-\mu^2}\cos(\varphi) \\ \sqrt{1-\mu^2}\sin(\varphi) \\ \mu \end{bmatrix}, \tag{2.3a}$$

where φ is the azimuthal angle, and μ is the cosine of the polar angle θ,

$$\mu \equiv \cos(\theta). \tag{2.3b}$$

This spatial and angular coordinates system is depicted visually in Fig. 2.1.

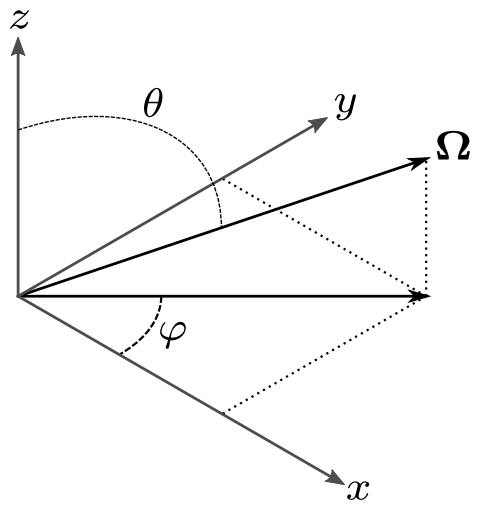

Figure 2.1: Depiction of the spatial and directional coordinate system used in the neutron transport equation.

The transport equation, given by Eq. (2.1), is an equation that represents the balance of neutrons. The streaming term, $\widehat{\mathbf{\Omega}} \cdot \boldsymbol{\nabla}\psi(\boldsymbol{x}, \widehat{\mathbf{\Omega}}, E)$, gives the rate at which neutrons are moving in or out of the of a point in phase-space due to motion. The collision term, $\Sigma_t(\boldsymbol{x}, E)\psi(\boldsymbol{x}, \widehat{\mathbf{\Omega}}, E)$, gives the rate at which neutrons have interactions (collisions) with a nucleus of the surrounding material. The source terms make up the right-hand side of the equation, and are separated into three components: an external source, the scattering source, and the fission source. The scattering source, $\int_0^\infty \int_{4\pi} \Sigma_s(\boldsymbol{x}, \widehat{\mathbf{\Omega}}' \cdot \widehat{\mathbf{\Omega}}, E' \rightarrow E)\psi(\boldsymbol{x}, \widehat{\mathbf{\Omega}}', E')\,\mathrm{d}\Omega'\,\mathrm{d}E'$, gives the rate at which neutrons are scattered into the given direction and energy at a set point in space. The fission source, $\chi(\boldsymbol{x}, E)\int_0^\infty \nu\Sigma_f(\boldsymbol{x}, E')\int_{4\pi}\psi(\boldsymbol{x}, \widehat{\mathbf{\Omega}}', E')\,\mathrm{d}\Omega'\,\mathrm{d}E'$, gives the production rate of neutrons due to fission events. The vast majority of fission events are prompt, though a small fraction of fission events emit *delayed* neutrons. Generally, in steady-state calculations the difference between prompt and delayed fission neutrons is ignored. However, for transient calculations, capturing this difference is

essential. The external source, $Q(\boldsymbol{x}, \widehat{\boldsymbol{\Omega}}, E)$, is a generic term that accounts for neutrons produced by all other processes that are not dependent on the angular flux.

Generally, reactor physicists are interested in reaction rates, that are useful for determining power production, rather than the angular flux. A reaction rate at a specific point, direction, and energy can be computed as the product of the reaction cross section and the angular flux. Integration over a volume, energy range, and direction gives a total reaction rate. These quantities are the primary figures of merit for engineering applications. For convenience, it is useful to define derived quantities that are used in these calculations. The *scalar flux*

$$\phi(\boldsymbol{x}, E) \equiv \int_{4\pi} \psi(\boldsymbol{x}, \widehat{\boldsymbol{\Omega}}, E)\, \mathrm{d}\Omega, \tag{2.4}$$

is the zeroth order angular moment. The neutron *current* is a vector quantity, and is the first order angular moment of the angular flux

$$\boldsymbol{J}(\boldsymbol{x}, E) \equiv \int_{4\pi} \widehat{\boldsymbol{\Omega}} \psi(\boldsymbol{x}, \widehat{\boldsymbol{\Omega}}, E)\, \mathrm{d}\Omega. \tag{2.5}$$

Generally, the angular moments of the angular flux are defined as

$$\Phi_\ell^n(\boldsymbol{x}, E) \equiv \int_{4\pi} R_\ell^n(\widehat{\boldsymbol{\Omega}}) \psi(\boldsymbol{x}, \widehat{\boldsymbol{\Omega}}, E)\, \mathrm{d}\Omega, \tag{2.6}$$

where $R_\ell^n(\widehat{\boldsymbol{\Omega}})$ are the real spherical harmonics functions defined by

$$R_\ell^n(\widehat{\boldsymbol{\Omega}}) \equiv \sqrt{(2 - \delta_{n,0}) \frac{(\ell - |n|)!}{(\ell + |n|)!}} P_\ell^{|n|}(\mu) \mathcal{T}(\varphi), \tag{2.7a}$$

where $P_\ell^{|n|}(\mu)$ is the Ferrer definition [1] of the associated Legendre Polynomial defined as

$$P_\ell^{|n|}(\mu) \equiv \left(1 - \mu^2\right)^{n/2} \frac{\mathrm{d}^n}{\mathrm{d}\mu^n} P_\ell(\mu), \quad n \geq 0, \tag{2.7b}$$

and

$$\mathcal{T}(\varphi) \equiv \begin{cases} \cos(n\varphi), & \text{if } n \geq 0, \\ \sin(|n|\varphi), & \text{otherwise.} \end{cases} \tag{2.7c}$$

2.2 k-Eigenvalue Problems

One of the most common calculations in reactor analysis is the simulation of reactor systems at operating conditions. A reactor operating at normal conditions is effectively unchanging in time. The common technique for solving this class of problems is to transform Eq. (2.1) into an eigenvalue problem, such that the fission source is scaled to preserve neutron balance:

$$\begin{aligned}\left[\widehat{\boldsymbol{\Omega}}\cdot\boldsymbol{\nabla}+\Sigma_t(\boldsymbol{x},E)\right]\psi(\boldsymbol{x},\widehat{\boldsymbol{\Omega}},E) = \frac{1}{4\pi}\Bigg[&Q(\boldsymbol{x},\widehat{\boldsymbol{\Omega}},E)\\ &+\int_0^\infty\int_{4\pi}\Sigma_s(\boldsymbol{x},\widehat{\boldsymbol{\Omega}}'\cdot\widehat{\boldsymbol{\Omega}},E'\to E)\psi(\boldsymbol{x},\widehat{\boldsymbol{\Omega}}',E')\,\mathrm{d}\Omega'\,\mathrm{d}E' \\ &+\frac{\chi(\boldsymbol{x},E)}{k_{\text{eff}}}\int_0^\infty\nu\Sigma_f(\boldsymbol{x},E')\phi(\boldsymbol{x},E')\,\mathrm{d}E'\Bigg],\end{aligned} \tag{2.8}$$

$$\forall\boldsymbol{x},\quad \forall\widehat{\boldsymbol{\Omega}}\in 4\pi,\quad \forall E\in[0,\infty),$$

where k_{eff} is the inverse of the largest eigenvalue of the system λ_1. The multiplication factor, k_{eff}, indicates the criticality of the system. If k_{eff} is one, then the system is *critical* and will remain at the current conditions unless otherwise changed. A k_{eff} less than one means that the system is *subcritical* and indicates the reactor system is unable to sustain the chain reaction of nuclear fission reactions to produce power. Finally, a k_{eff} greater than one indicates that a system is *supercritical* and, if not changed, the neutron population will increase.

Generally, this class of problems are solved iteratively. This will be discussed in more detail in Section 2.5, which lists algorithms for this iteration process. Still, Eq. (2.8) has a six-dimensional phase space and cannot, in general systems, be solved exactly. Numerical techniques must be used to obtain approximate solutions to this equation in calculations for realistic reactor systems. In the Section 2.3, an overview of several methods for solving this equation, or approximate forms of this equation, is provided.

2.3 Computational Transport Methods

Generally, transport methods are divided into two broad categories: stochastic and deterministic. Stochastic methods, also called "Monte Carlo" methods, rely on random sampling to emulate the "life" of individual neutrons. Deterministic methods rely on discretization of the transport equation. The process of discretization introduces approximations. An overview of these different approaches is given in the following subsections.

2.3.1 Monte Carlo

Stochastic, or "Monte Carlo" methods are methods that simulate individual neutrons in the system. The simulation of each neutron relies on the random sampling of probability distributions for all aspects such as, where the *free* neutron is born, which direction it is traveling in, the energy of the neutron, the distance to the next collision, and the type of collision event. This process is repeated until the neutron leaks out of the system or is absorbed, possibly inducing a fission event with other neutrons to simulate, for many different neutrons.

Monte Carlo methods give a probabilistic estimate of the true solution as well as an associated uncertainty in that result. This class of methods is generally considered to be the most accurate because they are capable of representing the phase-space continuously. As more particles are simulated the uncertainty in the estimated solution is reduced.

For whole-core reactor analysis, the quantities of interest would typically require an extremely large number of individual neutron histories to be simulated, typically trillions. Variance reduction techniques are an area of active research that allow for quantities of interest to be estimated accurately with fewer histories. However, generally Monte Carlo methods remain too expensive for whole-core calculations, and have challenges with multiphysics and time-dependent problems.

2.3.2 Deterministic Methods

In deterministic methods, it is generally not possible to represent the phase-space continuously. Thus these methods rely on discretization of the transport equation. In particular, spatial, directional, and energy discretization are common in these methods.

2.3.2.1 The Multigroup Approximation

The multigroup approximation is an approximation that is common in nearly every deterministic neutron transport method. This approximation discretizes the energy variable into discrete energy groups. Generally, cross sections have strong dependence on the energy of incident neutrons; this dependence is typically not smooth due to the presence of resonances. Around resonance energies, the cross sections are increased significantly, as observed in Fig. 2.2.

The complicated dependence on energy would require hundreds of thousands of energy points to faithfully represent all the resonances of interest in thermal reactors. Modeling of this many energy points in whole-core simulations would be computationally impractical. The multigroup eigenvalue transport equation can be found by integrating the Eq. (2.8) over an energy energy

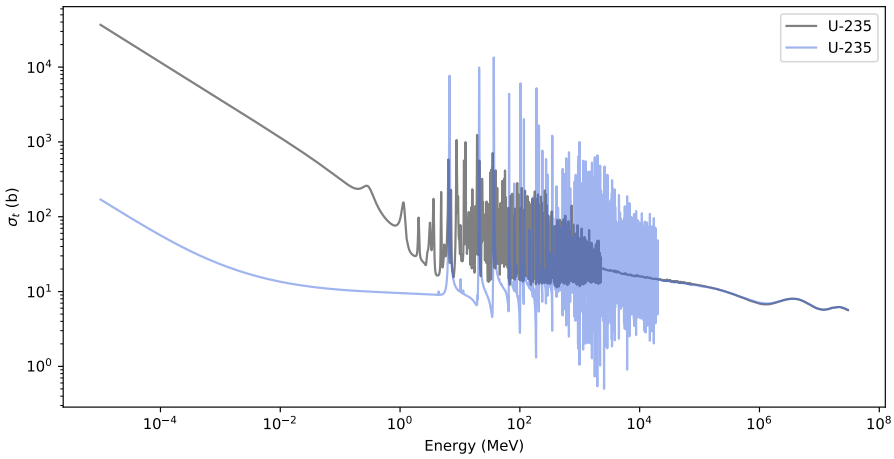

Figure 2.2: Uranium 235 and 238 total microscopic cross sections as a function of energy. Data provided through the ENDF-8.0 nuclear reaction data library [2].

interval $[E_g, E_{g-1})$, where $E_g > E_{g-1}$.

$$\left[\widehat{\boldsymbol{\Omega}} \cdot \boldsymbol{\nabla} + \Sigma_t^g(\boldsymbol{x}, \widehat{\boldsymbol{\Omega}})\right] \psi^g(\boldsymbol{x}, \widehat{\boldsymbol{\Omega}}) = \frac{1}{4\pi}\left[\sum_{g'=1}^{G} \int_{4\pi} \Sigma_s^{g' \to g}(\boldsymbol{x}, \widehat{\boldsymbol{\Omega}}, \widehat{\boldsymbol{\Omega}}') \psi^{g'}(\boldsymbol{x}, \widehat{\boldsymbol{\Omega}}') \, \mathrm{d}\Omega' + \frac{\chi^g(\boldsymbol{x})}{k_{\text{eff}}} \sum_{g'=1}^{G} \nu \Sigma_f^{g'}(\boldsymbol{x}, \widehat{\boldsymbol{\Omega}}) \phi^{g'}(\boldsymbol{x})\right] \tag{2.9}$$

$$\forall \boldsymbol{x}, \quad \forall \widehat{\boldsymbol{\Omega}} \in 4\pi, \quad \forall g \in \{1, 2, \ldots, G\},$$

where the multigroup quantities are defined by

$$\psi^g(\boldsymbol{x}, \widehat{\boldsymbol{\Omega}}) \equiv \int_{E_g}^{E_{g-1}} \psi(\boldsymbol{x}, \widehat{\boldsymbol{\Omega}}, E) \, \mathrm{d}E, \tag{2.10a}$$

$$\chi^g(\boldsymbol{x}) \equiv \int_{E_g}^{E_{g-1}} \chi(\boldsymbol{x}, E) \, \mathrm{d}E, \tag{2.10b}$$

$$\Sigma_t^g(\boldsymbol{x}, \widehat{\boldsymbol{\Omega}}) \equiv \frac{\int_{E_g}^{E_{g-1}} \Sigma_t(\boldsymbol{x}, E) \psi(\boldsymbol{x}, \widehat{\boldsymbol{\Omega}}, E) \, \mathrm{d}E}{\psi^g(\boldsymbol{x}, \widehat{\boldsymbol{\Omega}})}, \tag{2.10c}$$

$$\nu\Sigma_f^g(\boldsymbol{x}, \widehat{\boldsymbol{\Omega}}) \equiv \frac{\int_{E_g}^{E_{g-1}} \nu\Sigma_f(\boldsymbol{x}, E) \psi(\boldsymbol{x}, \widehat{\boldsymbol{\Omega}}, E) \, \mathrm{d}E}{\psi^g(\boldsymbol{x}, \widehat{\boldsymbol{\Omega}})}, \tag{2.10d}$$

$$\Sigma_s^{g'\to g}(\boldsymbol{x},\widehat{\boldsymbol{\Omega}},\widehat{\boldsymbol{\Omega}}') \equiv \frac{\int_{E_g}^{E_{g-1}}\int_{E_{g'}}^{E_{g'-1}} \Sigma_s(\boldsymbol{x},\widehat{\boldsymbol{\Omega}}'\cdot\widehat{\boldsymbol{\Omega}},E'\to E)\psi(\boldsymbol{x},\widehat{\boldsymbol{\Omega}}',E')\,\mathrm{d}E'\,\mathrm{d}E}{\psi^{g'}(\boldsymbol{x},\widehat{\boldsymbol{\Omega}}')}. \tag{2.10e}$$

By defining the cross sections in this way, no approximations have been made, and the reaction rates of each energy group are preserved. However, this approach has two issues: the cross sections are dependent on the angular flux which is not known *a priori*, and have dependence on the neutron direction of flight. Generally, the dependence on the angular flux is addressed by solving a *spatially* simplified problem to generate a continuous or fine-group neutron energy spectrum. This spectrum is then used as the weighting function (in place of $\psi^g(\boldsymbol{x},\widehat{\boldsymbol{\Omega}})$) to "collapse" the cross sections into coarser multigroup values [3]. This introduces an approximation into the transport equation.

To eliminate the directional dependence of the multigroup cross sections, an additional approximation is made: isotropic angular flux spectrum,

$$\psi(\boldsymbol{x},\widehat{\boldsymbol{\Omega}},E) \approx \frac{1}{4\pi}\Phi(\boldsymbol{x},E). \tag{2.11}$$

Using this approximate angular flux as the weighting function for multigroup cross sections in Eq. (2.9) and Eqs. (2.10) can be simplified to

$$\begin{aligned}\left[\widehat{\boldsymbol{\Omega}}\cdot\boldsymbol{\nabla}+\Sigma_t^g(\boldsymbol{x})\right]\psi^g(\boldsymbol{x},\widehat{\boldsymbol{\Omega}}) = \frac{1}{4\pi}\Bigg[&\sum_{g'=1}^{G}\int_{4\pi}\Sigma_s^{g'\to g}(\boldsymbol{x},\widehat{\boldsymbol{\Omega}}'\cdot\widehat{\boldsymbol{\Omega}})\psi^{g'}(\boldsymbol{x},\widehat{\boldsymbol{\Omega}}')\,\mathrm{d}\Omega' \\ &+\frac{\chi^g(\boldsymbol{x})}{k_{\text{eff}}}\sum_{g'=1}^{G}\nu\Sigma_f^{g'}(\boldsymbol{x})\int_{4\pi}\psi^{g'}(\boldsymbol{x},\widehat{\boldsymbol{\Omega}}')\,\mathrm{d}\Omega'\Bigg], \\ \forall\boldsymbol{x},\quad \forall\widehat{\boldsymbol{\Omega}}\in 4\pi,\quad &\forall g\in\{1,2,\ldots,G\},\end{aligned} \tag{2.12}$$

where the approximated multigroup cross sections are defined as

$$\Sigma_t^g(\boldsymbol{x}) \equiv \frac{\int_{E_g}^{E_{g-1}}\Sigma_t(\boldsymbol{x},E)\Phi(\boldsymbol{x},E)\,\mathrm{d}E}{\int_{E_g}^{E_{g-1}}\Phi(\boldsymbol{x},E)\,\mathrm{d}E}, \tag{2.13a}$$

$$\nu\Sigma_f^g(\boldsymbol{x}) \equiv \frac{\int_{E_g}^{E_{g-1}}\nu\Sigma_f(\boldsymbol{x},E)\Phi(\boldsymbol{x},E)\,\mathrm{d}E}{\int_{E_g}^{E_{g-1}}\Phi(\boldsymbol{x},E)\,\mathrm{d}E}, \tag{2.13b}$$

$$\Sigma_s^{g'\to g}(\boldsymbol{x},\widehat{\boldsymbol{\Omega}}'\cdot\widehat{\boldsymbol{\Omega}}) \equiv \frac{\int_{E_g}^{E_{g-1}}\int_{E_{g'}}^{E_{g'-1}}\Sigma_s(\boldsymbol{x},\widehat{\boldsymbol{\Omega}}'\cdot\widehat{\boldsymbol{\Omega}},E'\to E)\Phi(\boldsymbol{x},E')\,\mathrm{d}E'\,\mathrm{d}E}{\int_{E_{g'}}^{E_{g'-1}}\Phi(\boldsymbol{x},E')\,\mathrm{d}E'}. \tag{2.13c}$$

For thermal reactors, the weighting spectrum, $\Phi(\boldsymbol{x},E)$, is well approximated by a spatially uniform spectrum, $\Phi(E)$. This justifies the use of the spectrum of the spatially simplified system.

However, this is not the case for other systems, such as fast reactors. In such systems, the spatial dependence of the weighting spectrum plays is important to capture accurately, and the above methods cannot be used.

2.3.2.2 Spatial Discretization

Nearly all computational transport methods involve some form of spatial discretization. Reactor designs include many different material regions, and nearly all simulation tools will discretize the spatial domain into these different material regions. Deterministic methods will generally apply a finer meshing within these material regions, to discretize them into *transport cells*. For the purposes of this work, a cell $\mathcal{R}_i$ is indexed with i. A visualization of the material and hypothetical meshing of a characteristics based transport method for a single pin-cell are shown in Fig. 2.3. In deterministic codes, the typical assumption is that material properties (cross sections) are constant within each computational cell.

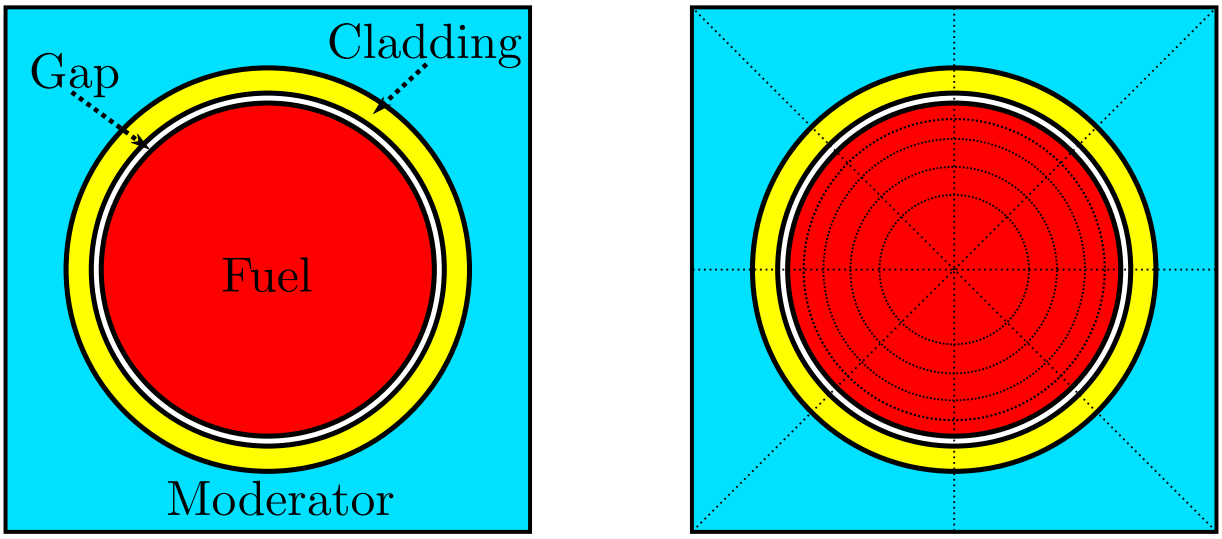

(a) Material regions

(b) Hypothetical computational cell mesh

Figure 2.3: Material and mesh spatial discretization examples for a single pin cell.

2.3.2.3 Directional Discretization

Typically, the directional variable cannot be treated exactly in deterministic methods. There are two common methods of approximating the solution as a function of direction $\widehat{\Omega}$:

1. Spherical Harmonics (P_N) Expansion
2. Discrete Ordinates (S_N)

Spherical Harmonics (P_N) Expansion Expansion in spherical harmonics, often referred to as P_N, is one of the oldest transport methods, where N indicates the order of the expansion. In this method, the angular flux is expanded as a linear combination of spherical harmonics moments:

$$\psi_m^g(\boldsymbol{x}) = \sum_{l=0}^{\infty} \sum_{n=-l}^{l} \Phi_\ell^n(\boldsymbol{x}, E) R_\ell^n(\widehat{\boldsymbol{\Omega}}), \tag{2.14}$$

where the spherical harmonics,$R_\ell^n(\widehat{\boldsymbol{\Omega}})$, are defined by Eqs. (2.7). No approximation has been introduced at this point, but in practice this series is truncated at some finite number N:

$$\psi_m^g(\boldsymbol{x}) \approx \sum_{l=0}^{N} \sum_{n=-l}^{l} \Phi_\ell^n(\boldsymbol{x}, E) R_\ell^n(\widehat{\boldsymbol{\Omega}}). \tag{2.15}$$

The P_N equations can be found by multiply the multi-group transport equation (Eq. (2.12)) by $R_\ell^n(\widehat{\boldsymbol{\Omega}})$ for each valid (l, n) pair under the specified order, and integrating over 4π. This yields a system of $(N+1)^2$ equations for each energy group; the number of equations increases quadratically with increasing orders, making P_N methods less feasible for large calculations.

Discrete Ordinates (S_N) The Discrete Ordinates (S_N) method is a discretization of the directional variable $\widehat{\boldsymbol{\Omega}}$ by a quadrature. Let the $\mathcal{M}_N$ be the set of discrete directions, and weights,

$$\mathcal{M}_N \equiv \left\{ \widehat{\boldsymbol{\Omega}}_m \in \{\widehat{\boldsymbol{\Omega}}_1, \widehat{\boldsymbol{\Omega}}_2, \ldots, \widehat{\boldsymbol{\Omega}}_N\}, w_m \in \{w_1, w_2, \ldots, w_N\} \right\}, \tag{2.16a}$$

such that a directional integration can be approximated as

$$\int_{4\pi} f(\widehat{\boldsymbol{\Omega}}) \, \mathrm{d}\Omega \approx 4\pi \sum_{m \in \mathcal{M}_N} w_m f(\widehat{\boldsymbol{\Omega}}_m), \tag{2.16b}$$

where

$$\sum_{m \in \mathcal{M}_N} w_m = 1. \tag{2.16c}$$

There are two common forms of quadrature sets that are commonly used in transport calculations: level-symmetric and product quadratures. The level-symmetric quadratures include directions that are evenly distributed over the unit-sphere; this is optimal in situations where each direction has similar variation. However, typical reactor designs have significantly less variation in the axial (z) direction which fuel rods are oriented along. In this situation, neutrons with directions close to the z-axis are modeled poorly because there are few azimuthal angles at these polar levels, as is demonstrated in Fig. 2.4a. These steep polar angles are important in reactor analysis due to

self-shielding effects, which are strongly dependent on polar angle.

Product quadratures are generated by a multiplicative combination of separate quadrature sets in the azimuthal and polar directions. The azimuthal quadrature set is generated over the domain $[0, 2\pi]$, while the polar quadrature set is generated for the polar cosine, μ, over the domain $[-1, 1]$. This quadrature generation technique does not suffer from the same issue for steep polar directions, as each polar level has the same number of azimuthal directions. A common choice for the azimuthal quadrature generation is the Chebyshev quadrature, which gives evenly spaced azimuthal angles with equal weights. The polar cosine quadrature set typically uses a Gauss-Legendre quadrature, or an optimized quadrature such as the Tabuchi-Yamamoto quadrature [4]. Figure 2.4b shows an example of a product quadrature's set of directions using a Chebyshev azimuthal quadrature and Gauss-Legendre polar quadrature.

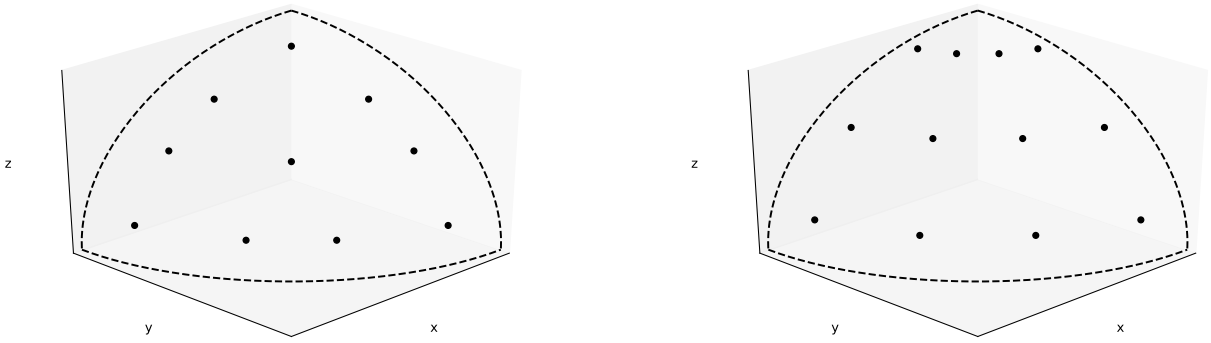

(a) Level-Symmetric Quadrature (S_8)

(b) Chebyshev-Gauss Product Quadrature with 4 azimuthal and 3 polar angles

Figure 2.4: (a) Level-Symmetric and (b) product quadrature direction set examples shown for a single octant of the unit-sphere.

2.4 State-of-the-Art 3-D Computational Transport Methods

Until recently, whole-core neutronics calculations were carried out primarily through a two-step procedure. First, a transport method was used to compute homogenized cross section data for assemblies, and then 3-D diffusion was used to solve the problem. More recently, however, research has been focused on a one-step approach, so called direct whole-core transport. In such an approach, the 3-D reactor is directly modeled using transport methods. There are many different transport methods which are currently being researched; this section seeks to give an overview of several state-of-the-art 3-D transport methods.

2.4.1 SP_N

The Simplified P_N (SP_N) method was introduced by Gelbard [5] in 1961, and was seen as a middle ground between diffusion and transport [6]. The SP_N equations were first derived by examining the form of the 1-D P_N equations; in fact, the 1-D SP_N and P_N equations are equivalent. While the original derivation Gelbard [5] lacked theoretical justification, the SP_N method has since been shown to be an asymptotic correction to standard diffusion theory [7].

The mono-energetic planar geometry P_N equations can be written as

$$\frac{\mathrm{d}}{\mathrm{d}z}\left[\frac{l}{2l+1}\phi_{l-1}+\frac{l+1}{2l+1}\phi_{l+1}\right]+\Sigma_t\phi_l=\Sigma_{s,l}\phi_l+Q\delta_{l,0},\quad \text{for}\quad 0\leq l\leq N, \tag{2.17a}$$

where $\Sigma_{s,l}$ is the lth order scattering moment and Q is either an external source or fission source. The expansion is generally truncated by assuming that $\phi_{N+1}=0$.

The 1-D P_1 equation can be written as

$$-\frac{\mathrm{d}}{\mathrm{d}z}\frac{\mathrm{d}}{\mathrm{d}z}\phi_0+\Sigma_t\phi_0=\Sigma_{s,0}\phi_0+Q, \tag{2.18}$$

where

$$\equiv\frac{1}{3(\Sigma_t-\Sigma_{s,1})}. \tag{2.19}$$

The 3-D P_1 equations simply replace the derivative term operator of Eq. (2.18) with the 3-D diffusion operator,

$$\frac{\mathrm{d}}{\mathrm{d}z}\frac{\mathrm{d}}{\mathrm{d}z}\rightarrow\boldsymbol{\nabla}\cdot\boldsymbol{\nabla},$$

yielding the 3-D P_1 (diffusion) equation:

$$-\boldsymbol{\nabla}\cdot\boldsymbol{\nabla}\phi_0+\Sigma_t\phi_0=\Sigma_{s,0}\phi_0+Q. \tag{2.20}$$

This simple relation between 1-D and 3-D equations only holds for the special P_1 case. The SP_N method uses a similar modification for higher-order P_N equations. This results in some lost accuracy compared to P_N, but the SP_N equations are significantly simpler to solve [5, 6]. Unlike P_N, SP_N equations do not converge to the transport solution as $N\rightarrow\infty$, but do generally have higher accuracy than diffusion (for orders of $N>1$). Generally, SP_3 or SP_5 are considered to have sufficient accuracy, and are generally less computationally intensive than transport methods.

The mono-energetic SP_N equations can be written as

$$-\boldsymbol{\nabla}\cdot\frac{1}{3\Sigma_{tr,1}}\boldsymbol{\nabla}\phi_0-\boldsymbol{\nabla}\cdot\frac{2}{3\Sigma_{tr,1}}\boldsymbol{\nabla}\phi_2+\Sigma_{tr,0}\phi_0=Q, \tag{2.21a}$$

$$
\begin{aligned}
&- \boldsymbol{\nabla} \cdot \left(\frac{n(n-1)}{(2n+1)(2n-1)\Sigma_{tr,n-1}} \right) \boldsymbol{\nabla} \phi_{n-2} \\
&- \boldsymbol{\nabla} \cdot \left(\frac{(n+1)(n+2)}{(2n+1)(2n+3)\Sigma_{tr,n+1}} \right) \boldsymbol{\nabla} \phi_{n+2} \\
&- \boldsymbol{\nabla} \cdot \left(\frac{n^2}{(2n+1)(2n-1)\Sigma_{tr,n-1}} + \frac{(n+1)^2}{(2n+1)(2n+3)\Sigma_{tr,n+1}} \right) \boldsymbol{\nabla} \phi_n \\
&+ \Sigma_{tr,n} \phi_n = 0, \quad \text{for} \quad n = 2, 4, ..., N-1,
\end{aligned}
\tag{2.21b}
$$

where

$$
\Sigma_{tr,n} \equiv \Sigma_t - \Sigma_{s,n}. \tag{2.21c}
$$

[CURRENT RESEARCH]

2.4.2 2D/1D Methods

The 2D/1D methods were first developed by researchers at Korea Advanced Institute of Science and Technology (KAIST) [8] and Korea Atomic Energy Research Institute (KAERI) [9], in the CRX and DeCART codes, respectively. Though different, these two methods followed the same fundamental approach to solving 3-D reactor transport problems:

1. Divide the core into separate axial slices/planes,
2. Perform 2-D transport calculations within each plane,
3. Couple the planes with transverse leakages.

These methods were based on the assumption that reactors may be very heterogeneous in the radial direction, but in the axial direction they are relatively homogeneous. The primary difference between these two methods is in the transverse leakage terms; in CRX the transverse leakages are anisotropic, but in DeCART the leakages are isotropic. To distinguish these methods, they will be referred to as anisotropic and isotropic 2D/1D methods.

Following the relative success of these methods, other research groups have followed in their paths. nTRACER [10], and MPACT [11] used the isotropic 2D/1D method. The PANX [CITATION], STREAM [12], and APOLLO3 [13] have also implemented 2D/1D methods.

Stimpson [14] implemented an anisotropic 2D/1D method in MPACT using a Fourier expansion of the azimuthal angles for the axial and radial transverse leakages. Jarrett [15] further improved upon Stimpson's [14] work by introducing a 2D/1D method using P_3 in the axial direction.

[FAILINGS] [DERIVATION]

2.4.3 Extruded 3-D Methods

Proteus - FEM STREAM - Linear orthogonal polynomials APOLLO - ? Nick H. - Legendre Expansion SooYoung - Diamond-Difference

2.4.4 Method of Characteristics

The Method of Characteristics (MoC) is a technique used in mathematics to solve Partial Differential Equations (PDEs), by transforming a PDE into a system of Ordinary Differential Equations (ODEs). The method was first applied to the neutron transport problem by Askew in 1972 [16], but only began to see real use in the 1980's [17]. The MoC transforms the transport equation into the characteristic form, by examining the equation along straight neutron paths through the spatial domain.

By examining the equation along one of these characteristic "tracks" or "rays", the average angular flux along the track within a cell can be calculated. The scalar flux can then be found by collecting the average angular flux along all tracks passing through this region, in a numerical integration over space and angle.

Like the Collision Probability (CP) method, MoC is able to handle completely arbitrary geometry; however, unlike the CP method, it is also able to account for anisotropic scattering in a straightforward manner. Additionally, the MoC does not produce the large matrices in realistic applications as the CP method does. For problems that contain more than a few hundred cells, the MoC is generally preferred over CP methods [18].

The method of Characteristic Direction Probabilities (CDP) is a method similar to both CP method and the MoC [19, 20]. The CDP uses ray-tracing to evaluate transmission probabilities between cells. However, it only considers transmission probabilities between cells which are traversed by a shared characteristic ray, rather than considering the transmission probability between all cells as in the CP methods. This significantly cuts down on the computational resources required by traditional CP methods. This method has also shown improvements over MoC in cases with few unique geometries and constant material properties throughout the simulation; however these conditions are not applicable in problems of interest to industry.

The MoC is the primary subject of this thesis work. As such, Chapter 3 has been devoted to the details of the method, and Section 3.4 expands upon the details of current ray-tracing techniques used in MoC. Chapter 5 details improvements made to the MoC in this thesis work, and Chapter 6 details a newly investigated ray-tracing method.

2.5 Source Iteration

Generally, the k-eigenvalue transport problems, introduced in Section 2.2, are solved iteratively. Given an initial guess for the k-eigenvalue, boundary conditions, and interior flux-moments, an estimate of the source can be computed. A transport "sweep" can be performed, in which updated boundary conditions and flux-moments are computed. Given these updated flux-moments a new estimate of the eigenvalue can be calculated. This process can be repeated until the eigenvalue and flux-moments are converged within some tolerance. For simplicity, this process is shown for a isotropic mono-energetic, continuous-space, one-dimensional transport problem in Algorithm 1.

Algorithm 1 Source Iteration algorithm for the k-eigenvalue transport problem.

1: Begin iteration j with a known boundary conditions, scalar flux estimate, $\phi^{(j)}(x)$, and a k-eigenvalue estimate, k_{eff}^{j}.
2: Perform a transport sweep:

$$\left[\mu\frac{\partial}{\partial x} + \Sigma_t(x)\right]\psi^{(j+1)}(x,\mu) = \frac{1}{2}\left[\Sigma_s(x) + \frac{1}{k_{\text{eff}}^{(j)}}\nu\Sigma_f(x)\right]\phi^{(j)}(x), \tag{2.22}$$

$$\forall x \in [0, X], \quad \forall \mu \in [-1, 1].$$

3: Update the scalar flux, and the eigenvalue for the next iteration:

$$\phi^{(j+1)}(x) = \int_{-1}^{1}\psi^{(j+1)}(x,\mu)\,\mathrm{d}\mu\frac{\Phi_0}{\frac{1}{X}\int_0^X\int_{-1}^{1}\psi^{(j+1)}(x',\mu)\,\mathrm{d}\mu\,\mathrm{d}x'}, \tag{2.23a}$$

$$k_{\text{eff}}^{(j+1)} = \frac{\int_0^X \nu\Sigma_f\phi^{(j+1)}(x)\,\mathrm{d}x}{\int_0^X \Sigma_a\phi^{(j+1)}(x)\,\mathrm{d}x}. \tag{2.23b}$$

4: Repeat steps 1. - 3. until sufficient convergence.

2.5.1 Transport Acceleration

While Algorithm 1 is valid, it typically converges very slowly, requiring many iterations to get reasonable results. In full-core calculations, a single transport sweep is typically the most computationally expensive operation and using Algorithm 1 is not feasible. There has been considerable effort in developing methods that accelerate transport calculations by using a lower-order calculation, typically based on the diffusion approximation. These methods often reduce the number of iterations from O(1000) to O(10) for thermal reactor systems.

While other acceleration methods exist [21], the most common for k-eigenvalue problems are non-linear diffusion acceleration (NDA) methods [22], typically using the coarse mesh finite-

difference (CMFD) method [23]. Algorithm 2 lists the standard NDA algorithm for a 1-D mono-energetic k-eigenvalue problem. The primary difference between CMFD and NDA is that CMFD introduces the concept of a second, coarser spatial grid, while NDA uses the same mesh as the transport problem.

The CMFD acceleration method has been shown to significantly reduce computational transport run-times [22, 24, 25]. There have been several improvements upon the original CMFD formulation [23], such as pCMFD [8] and odCMFD [26]. The pCMFD method preserves partial currents rather than net currents, and has been shown to be unconditionally stable for transport problems at fixed conditions [8]. The odCMFD method generalizes the CMFD and pCMFD methods by adding an artificial term to the diffusion coefficient, and has faster convergence properties than pCMFD [26]. Recently, it was shown that the theoretical reason for this is the that most MoC methods do not preserve the linear solutions of the transport equation, resulting in the need for an unphysical correction to the diffusion coefficient to account for truncation error in the transport discretization.

Utilization of CMFD acceleration in transport calculations with thermal-hydraulic (T/H) feedback has not had the favorable stability and convergence properties as calculations without feedback [27]. Many transport codes have required under-relaxation of the scalar flux in the iteration schemes for stability in these calculations; there is ongoing research investigating a less ad-hoc approach [27]. This instability and convergence slow-down in problems with feedback has prevented full utilization of more advanced multi-level solvers [27, 28].

Algorithm 2 Non-linear Diffusion Acceleration (NDA) algorithm for the k-eigenvalue transport problem.

1: Begin iteration i with known boundary conditions, scalar flux estimate, $\phi^{(j)}(x)$, a net current estimate, $\boldsymbol{J}^{(j)}(x)$, and a k-eigenvalue estimate, k_{eff}.

2: Compute linear and non-linear correction factors for low-order diffusion equation:

$$\widehat{D}^{(j)}(x) = \frac{\frac{\mathrm{d}}{\mathrm{d}x}\left[J^{(j)}(x) + \frac{1}{3\Sigma_t(x)}\frac{\mathrm{d}\phi^{(j)}(x)}{\mathrm{d}x}\right]}{\phi^{(j)}(x)} \tag{2.24}$$

3: Solve the low-order diffusion eigenvalue problem:

$$-\frac{\mathrm{d}}{\mathrm{d}x}\frac{1}{3\Sigma_t(x)}\frac{\mathrm{d}\phi^{(j+1/2)}(x)}{\mathrm{d}x} + \left[\Sigma_a(x) + \widehat{D}^{(j)}(x)\right]\phi^{(j+1/2)}(x) = \frac{1}{k_{\text{eff}}}\nu\Sigma_f(x)\phi^{(j+1/2)}(x). \tag{2.25}$$

4: Perform a transport sweep using the scalar flux, and eigenvalue estimates from the low-order diffusion calculation:

$$\left[\mu\frac{\partial}{\partial x} + \Sigma_t(x)\right]\psi^{(j+1)}(x,\mu) = \frac{1}{2}\left[\Sigma_s(x) + \frac{1}{k_{\text{eff}}^{(j)}}\nu\Sigma_f(x)\right]\phi^{(j)}(x), \tag{2.26}$$

$$\forall x \in [0, X], \quad \forall \mu \in [-1, 1].$$

5: Update the scalar flux, current, and eigenvalue estimates for next iteration:

$$\phi^{(j+1)}(x) = \int_{-1}^{1}\psi^{(j+1)}(x,\mu)\,\mathrm{d}\mu\frac{\Phi_0}{\frac{1}{X}\int_0^X\int_{-1}^{1}\psi^{(j+1)}(x',\mu)\,\mathrm{d}\mu\,\mathrm{d}x'}, \tag{2.27a}$$

$$\boldsymbol{J}^{(j+1)}(x) = \int_{-1}^{1}\mu\psi^{(j+1)}(x,\mu)\,\mathrm{d}\mu\frac{\Phi_0}{\frac{1}{X}\int_0^X\int_{-1}^{1}\psi^{(j+1)}(x',\mu)\,\mathrm{d}\mu\,\mathrm{d}x'}, \tag{2.27b}$$

$$k_{\text{eff}}^{(j+1)} = \frac{\int_0^X \nu\Sigma_f\phi^{(j+1)}(x)\,\mathrm{d}x}{\int_0^X \Sigma_a\phi^{(j+1)}(x)\,\mathrm{d}x}. \tag{2.27c}$$

Bibliography

[1] Ladislav Trlifaj. "Some Aspects of the Spherical Harmonics Method for Neutron-Transport Problems in Cylindrical Geometry". In: *Czechoslovak Journal of Physics* 8 (1958), pp. 390–395.

[2] D. A. Brown et al. "ENDF/B-VIII.0: The 8th Major Release of the Nuclear Reaction Data Library with CIELO-project Cross Sections, New Standards and Thermal Scattering Data". In: *Nuclear Data Sheets* 148 (2018), pp. 1–142. ISSN: 00903752. DOI: 10.1016/j.nds.2018.02.001.

[3] Dave Knott and Akio Yamamoto. "Lattice Physics Computations". In: *Handbook of Nuclear Engineering* (2010), pp. 913–1239. DOI: 10.1007/978-0-387-98149-9_9.

[4] Akio Yamamoto et al. "Derivation of optimum polar angle quadrature set for the method of characteristics based on approximation error for the bickley function". In: *Journal of Nuclear Science and Technology* 44.2 (2007), pp. 129–136. ISSN: 00223131. DOI: 10.1080/18811248.2007.9711266.

[5] E. M. Gelbard. *Simplified Spherical Harmonics equations and their use in shielding problems*. Tech. rep. Bettis Atomic Power Laboratory, 1961.

[6] Ryan G. Mcclarren. "Theoretical aspects of the simplified pn equations". In: *Transport Theory and Statistical Physics* 39.2-4 (2010), pp. 73–109. ISSN: 00411450. DOI: 10.1080/00411450.2010.535088.

[7] Edward W. Larsen. "Asymptotic diffusion and simplified pn approximations for diffusive and deep penetration problems. Part 1: Theory". In: *Transport Theory and Statistical Physics* 39.2-4 (2010), pp. 110–163. ISSN: 00411450. DOI: 10.1080/00411450.2010.531878.

[8] Nam Zin Cho. "Fusion of method of characteristics and nodal method for 3-D whole-core transport calculation". In: *American Nuclear Society*. 2002, p. 322.

[9] Han Gyu Joo et al. “Methods and performance of a three-dimensional whole-core transport code DeCART”. In: *PHYSOR 2004*. 2004, pp. 21–34. ISBN: 0894486837. URL: http://www.scopus.com/inward/record.url?eid=2-s2.0-22344449157{\&}partnerID=tZOtx3y1.

[10] Yeon Sang Jung and Han Gyu Joo. “Decoupled Planar MOC Solution for Dynamic Group Constant Generation in Direct Three-Dimensional Core”. In: *M&C 2009* (2009).

[11] MPACT Team. *MPACT Theory Manual v2.2.0*. Tech. rep. Consortium for Advanced Simulation of Light Water Reactors, 2016.

[12] Youqi Zheng, Sooyoung Choi, and Deokjung Lee. “A new approach to three-dimensional neutron transport solution based on the method of characteristics and linear axial approximation”. In: *Journal of Computational Physics* 350 (2017), pp. 25–44. ISSN: 10902716. DOI: 10.1016/j.jcp.2017.08.026.

[13] Bastien Faure et al. “A 2D/1D Algorithm for Effective Cross-Section Generation in Fast Reactor Neutronic Transport Calculations”. In: *Nuclear Science and Engineering* 192.1 (2018), pp. 40–51. ISSN: 1943748X. DOI: 10.1080/00295639.2018.1480190.

[14] S.G. Stimpson. “An Azimuthal, Fourier Moment-Based Axial SN Solver for the 2D/1D Scheme”. PhD thesis. University of Michigan, 2015.

[15] Michael Gregory Jarrett. “A 2D/1D Neutron Transport Method with Improved Angular Coupling”. Doctoral. University of Michigan, 2018.

[16] J.R. Askew. *A Characteristics Formulation of the Neutron Transport Equation in Complicated Geometries*. 1972.

[17] M.J. Halsall. “CACTUS, a characteristics solution to the neutron transport equations in complicated geometries”. In: *Transactions of the American Nuclear Society*. 1980. URL: https://inis.iaea.org/search/search.aspx?orig{_}q=RN:12592444.

[18] Alain Hébert. “Multigroup Neutron Transport and Diffusion Computations”. In: *Handbook of Nuclear Engineering* (2010), pp. 751–911. DOI: 10.1007/978-0-387-98149-9_8.

[19] Ser Gi Hong and Nam Zin Cho. “Method of Characteristic Direction Probabilities for Heterogeneous Lattice Calculation”. In: *Nuclear Science and Engineering* 132.1 (2017), pp. 65–77. ISSN: 0029-5639. DOI: 10.13182/nse99-a2049.

[20] Zhouyu Liu et al. “Theory and analysis of accuracy for the method of characteristics direction probabilities with boundary averaging”. In: *Annals of Nuclear Energy* 77 (2015), pp. 212–222. ISSN: 0306-4549. DOI: 10.1016/J.ANUCENE.2014.11.016.

[21] Alain Hébert. “Acceleration of step and linear discontinuous schemes for the method of characteristics in DRAGON5”. In: *Nuclear Engineering and Technology* 49.6 (2017), pp. 1135–1142. ISSN: 2234358X. DOI: 10.1016/j.net.2017.07.004.

[22] K.S. Smith and J.D. Rhodes III. “Full-Core, 2-D, LWR Core Calculations with CASMO-4E”. In: *Physor* 1 (2002), pp. 1–13.

[23] Kord S. Smith. “Nodal method storage reduction by nonlinear iteration”. In: *Transactions of the American Nuclear Society*. Vol. 44. 1983, pp. 265–266.

[24] Dmitriy Y Anistratov. “Multi-level nonlinear diffusion acceleration method for multigroup transport k-eigenvalue problems”. In: *International Conference on Mathematics and Computational Methods Applied to Nuclear Science and Engineering, Rio de Janeiro, RJ, Brazil, May* 2 (2011), pp. 8–12.

[25] Benjamin Collins et al. “Stability and accuracy of 3D neutron transport simulations using the 2D/1D method in MPACT”. In: *Journal of Computational Physics* 326 (2016), pp. 612–628. ISSN: 10902716. DOI: 10.1016/j.jcp.2016.08.022.

[26] Ang Zhu et al. “An optimally diffusive Coarse Mesh Finite Difference method to accelerate neutron transport calculations”. In: *Annals of Nuclear Energy* 95 (2016), pp. 116–124. ISSN: 18732100. DOI: 10.1016/j.anucene.2016.05.004.

[27] Brendan Kochunas, Andrew Fitzgerald, and Edward Larsen. “Fourier analysis of iteration schemes for k-eigenvalue transport problems with flux-dependent cross sections”. In: *Journal of Computational Physics* 345 (2017), pp. 294–307. ISSN: 10902716. DOI: 10.1016/j.jcp.2017.05.028.

[28] Ben C. Yee, Brendan Kochunas, and Edward W. Larsen. “A Multilevel in Space and Energy Solver for 3-D Multigroup Diffusion and Coarse-Mesh Finite Difference Eigenvalue Problems”. In: *Nuclear Science and Engineering* 00.00 (2019), pp. 1–24. ISSN: 0029-5639. DOI: 10.1080/00295639.2018.1562777.

CHAPTER 3

The Method of Characteristics

3.1 Fundamentals

The Method of Characteristics (MoC) is a technique used in mathematics to solve PDEs, by transforming a PDE into a system of ODEs. The method was first applied to the neutron transport equation by Askew in 1972 [1], but only began to see real use in the 1980's [2]. The MoC transforms the transport equation into the characteristic form, by following the equation along straight neutron paths through the spatial domain. For brevity, the derivation of this method will begin with the multigroup S_N k-eigenvalue transport equation with spatially discretized mesh with constant material properties within each cell. Here, the spatial derivatives have not yet been discretized.

$$\left[\widehat{\boldsymbol{\Omega}}_m \cdot \boldsymbol{\nabla} + \Sigma_{t,i}^g\right] \psi_{mi}^g(\boldsymbol{x}) = \frac{1}{4\pi} q_{mi}^g(\boldsymbol{x}) \,, \tag{3.1}$$
$$\forall \boldsymbol{x} \in \mathcal{R}_i, \quad \forall m \in \mathcal{M}_N, \quad \forall i, g,$$

where $\mathcal{R}_i$ is the spatial cell, $\mathcal{M}_N$ is the directional quadrature, as described in Section 2.3.2.3, and the fixed-source, $q_{mi}^g(\boldsymbol{x})$ can be found by applying the discrete-to-moment operator, $\mathcal{S}_{i,m}^g$, defined by

$$\mathcal{S}_{i,m}^g(f) \equiv \sum_{g'} \sum_{\ell=0}^{L} \sum_{n=-\ell}^{\ell} R_\ell^n(\widehat{\boldsymbol{\Omega}}_m) \Sigma_{s,\ell,i}^{g' \to g} f_{n,i}^{\ell,g'}(\boldsymbol{x}) + \frac{\chi_i^g}{k_{\text{eff}}} \sum_{g'} \nu \Sigma_{f,i}^{g'} f_i^{g'}(\boldsymbol{x}), \tag{3.2}$$

to get

$$q_{mi}^g(\boldsymbol{x}) \equiv \left[\sum_{g'} \sum_{\ell=0}^{L} \sum_{n=-\ell}^{\ell} R_\ell^n(\widehat{\boldsymbol{\Omega}}) \Sigma_{s,\ell,i}^{g' \to g} \Phi_{i,n}^{\ell,g}(\boldsymbol{x}) + \frac{\chi_i^g}{k_{\text{eff}}} \sum_{g'} \nu \Sigma_{f,i}^{g'} \phi_i^{g'}(\boldsymbol{x}) \right], \tag{3.3}$$

where L is the maximum scattering order. If L were infinite, there would not any additional approximation to the scattering source; however, the first several orders have the most effect on the figures of merit, and in practice the sum is truncated with L typically being less than five.

Consider a point, $\boldsymbol{x}_0$, and a line passing through this point in direction $\widehat{\boldsymbol{\Omega}}_m$. Any location along

this *characteristic* line (also referred to as a ray, or track), can be described as

$$\boldsymbol{x} = \boldsymbol{x}_0 + s\widehat{\boldsymbol{\Omega}}_m, \tag{3.4}$$

where s is the distance along the track from $\boldsymbol{x}_0$. Applying this transformation, Eq. (3.1) is put into the characteristic form

$$\left[\frac{\mathrm{d}}{\mathrm{d}s} + \Sigma_{t,i}^g\right] \psi_{mi}^g\Big(\boldsymbol{x}_0 + s\widehat{\boldsymbol{\Omega}}_m\Big) = \frac{1}{4\pi} q_{mi}^g\Big(\boldsymbol{x}_0 + s\widehat{\boldsymbol{\Omega}}_m\Big)\,. \tag{3.5}$$

As stated in Section 2.1, reactor physicists are generally interested in spatially and directionally integrated angular flux quantities rather than the angular flux along a single path. Thus typical in the MoC to have many different characteristic tracks through our problem; in this work separate tracks will be subscripted with the index k. Each track is broken up into track-segments by considering the segments contained within each computational cell. The characteristic form of the transport equation then becomes

$$\left[\frac{\mathrm{d}}{\mathrm{d}s} + \Sigma_{t,i}^g\right] \psi_{mki}^g(s) = \frac{1}{4\pi} q_{mi}^g(s)\,, \tag{3.6}$$
$$\forall s \in [0, s_{mki}], \forall m \in \mathcal{M}_N, \forall i, k, g,$$

where s_{mki} is the total length of the track-segment, as depicted in Fig. 3.1.

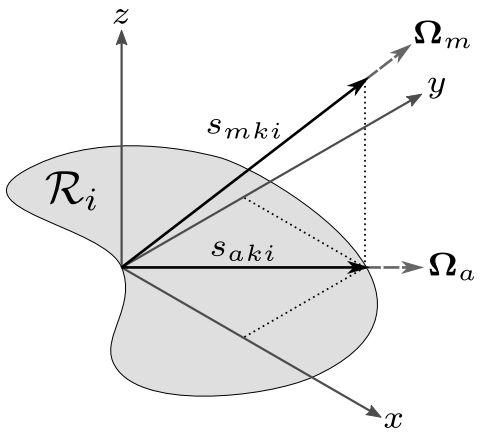

Figure 3.1: Depiction of a single characteristic track through a cell i.

Equation (3.6) can be solved analytically along a characteristic track-segment using an integrating factor,

$$M(s) = \exp\left(\int_0^s \Sigma_{t,i}^g \,\mathrm{d}s'\right) = \exp(\tau_m^g)\,, \tag{3.7}$$

where the *optical thickness*, τ_m^g, can be simplified as

$$\tau_m^g \equiv \Sigma_{t,i}^g s, \tag{3.8}$$

$$\forall s \in [0, s_{mki}],$$

assuming constant properties along the track-segment. Using this integrating factor, the generic solution to the MoC equation, given in Eq. (3.6), is

$$\psi_{mki}^g(s) = \psi_{mki}^{g,\text{in}} \exp(-\tau_m^g) + \int_0^s \frac{1}{4\pi} q_{mi}^g(s') \exp\left(-\Sigma_{t,i}^g \left[s - s'\right]\right) \mathrm{d}s', \tag{3.9}$$

where $\psi_{mki}^{g,\text{in}}$ is the incident angular flux, $\psi_{mki}^g(0)$. If a source shape is provided, Eq. (3.9) can be evaluated for every track-segment in the problem. The next subsection introduces formal methods to approximate the integration of quantities over both space and direction. These procedures can be used to determine the scalar flux or other quantities necessary in MoC calculations.

3.1.1 Track-Based Integration

Determining the angular flux along a single characteristic track is typically not very useful for reactor physics calculations. It is most often necessary to evaluate reaction rates, and therefore the scalar flux through integration of the angular flux. This section aims to provide a formal basis for the integration process used in the MoC for transport calculations.

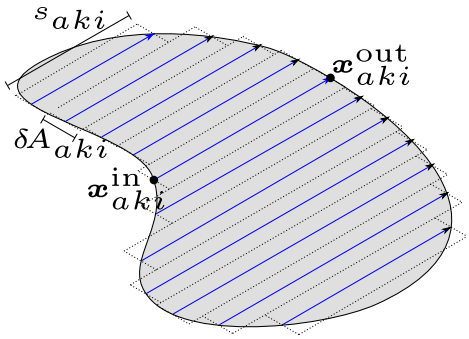

Figure 3.2: Example characteristic tracks (2D) through a cell for a single direction.

The MoC is based on the Discrete Ordinates (S_N) approximation; integration over the directional variable simply becomes a quadrature integration:

$$\int_{4\pi} f(\widehat{\boldsymbol{\Omega}}) \, \mathrm{d}\Omega \approx 4\pi \sum_m w_m f(\widehat{\boldsymbol{\Omega}}_m). \tag{3.10}$$

Within a cell, $\mathcal{R}_i$, there are many characteristic track-segments for each direction in the directional quadrature, as is shown for a single direction in Fig. 3.2. Thus, the spatial discretization is different for each direction, and spatial integration is linked with the directional integration. For a single direction, the integration over the spatial domain can be approximated by the weighted summation of track-averaged values, with the weight being equal to the area of the track-segment. The average value of a function, $f(\boldsymbol{x}, \widehat{\boldsymbol{\Omega}}_m)$, along a track-segment is denoted as

$$\Big\langle f(\boldsymbol{x}, \widehat{\boldsymbol{\Omega}}_m) \Big\rangle_{mki} \equiv \frac{1}{s_{mki}} \int_0^{s_{mki}} f(s, \widehat{\boldsymbol{\Omega}}_m)\, \mathrm{d}s, \tag{3.11}$$

where s_{mki} is the total length of the track-segment. The spatial integration for a single direction becomes

$$\frac{1}{V_i} \int_{\boldsymbol{x} \in \mathcal{R}_i} f(\boldsymbol{x}, \widehat{\boldsymbol{\Omega}}_m)\, \mathrm{d}^3\boldsymbol{x} \approx \Big\langle f(\boldsymbol{x}, \widehat{\boldsymbol{\Omega}}_m) \Big\rangle_{mi} \equiv \frac{1}{V_i} \sum_k \delta A_{mki} s_{mki} \Big\langle f(\boldsymbol{x}, \widehat{\boldsymbol{\Omega}}_m) \Big\rangle_{mki}, \tag{3.12}$$

where δA_{mki} is the cross-sectional area of the track (width in 2-D). In this notation, the integral is divided by the volume such that $\langle f \rangle_{mi}$ is approximately the mean value in the region, for the direction $\widehat{\boldsymbol{\Omega}}_m$. Finally, an integration over both space and angle can be defined as

$$\Big\langle f(\boldsymbol{x}, \widehat{\boldsymbol{\Omega}}) \Big\rangle_i = 4\pi \sum_m w_m \Big\langle f(\boldsymbol{x}, \widehat{\boldsymbol{\Omega}}_m) \Big\rangle_{mi}. \tag{3.13}$$

These integrations have been expressed as 3-D MoC equations. The general form remains the same for 2-D calculations, with minor changes. The spatial integration, Eq. (3.12), requires an additional scaling factor ($\sin(\theta_p)$), and the volume, V_i, is the area of the cell:

$$\frac{1}{V_i} \int_{\boldsymbol{x} \in \mathcal{R}_i} f(\boldsymbol{x}, \widehat{\boldsymbol{\Omega}}_m)\, \mathrm{d}^3\boldsymbol{x} \approx \Big\langle f(\boldsymbol{x}, \widehat{\boldsymbol{\Omega}}_m) \Big\rangle_{mi} \equiv \frac{\sin(\theta_p)}{V_i} \sum_k \delta A_{mki} s_{mki} \Big\langle f(\boldsymbol{x}, \widehat{\boldsymbol{\Omega}}_m) \Big\rangle_{mki} \tag{3.14}$$

The scaling factor is necessary (but not sufficient) for the integrated cell area to be preserved for each polar angle.

3.1.2 Track-Length Renormalization

In general, the spatial integration described in Section 3.1.1 does not preserve the cell volume; this is visually apparent in Fig. 3.2. In order to preserve spatial volumes within a cell, track-lengths are often "renormalized". As the area of each ray, δA_{mki} approaches zero, the renormalization becomes irrelevant; thus it is only of consequence when rays have relatively coarse spacing between each other. There are three renormalization methods which become obvious through the notation

presented in Section 3.1.1:

1. segment-volume preservation
2. direction-volume preservation
3. volume preservation

Track-length renormalization involves adjusting the lengths of track-segments such that volume is preserved. Let us define a renormalization factor, ξ_{mki}, such that the renormalized track-length is given by

$$t_{mki} = \xi_{mki} s_{mki}. \tag{3.15}$$

The spatial integration schemes given by Eqs. (3.11) and (3.12) become

$$\left\langle f(\boldsymbol{x}, \widehat{\boldsymbol{\Omega}}_m) \right\rangle_{mki} \equiv \frac{1}{t_{mki}} \int_0^{t_{mki}} f(s, \widehat{\boldsymbol{\Omega}}_m) \, \mathrm{d}t_m, \tag{3.16a}$$

and

$$\left\langle f(\boldsymbol{x}, \widehat{\boldsymbol{\Omega}}_m) \right\rangle_{mi} \equiv \frac{1}{V_i} \sum_k \delta A_{mki} t_{mki} \left\langle f(\boldsymbol{x}, \widehat{\boldsymbol{\Omega}}_m) \right\rangle_{mki}, \tag{3.16b}$$

where the spatial variable $\boldsymbol{x}$ can now be written as a function of the renormalized track-distance, t_m, as

$$\boldsymbol{x} = \boldsymbol{x}^{\text{in}}_{mki} + t_m \widehat{\boldsymbol{\Omega}}_m / \xi_{mki}, \tag{3.16c}$$

where $\boldsymbol{x}^{\text{in}}_{mki}$ is the starting point of the track-segment.

Segment-volume preservation is a renormalization method in which the track-length is adjusted such that the analytic volume within the cross-sectional area of each track-segment is preserved. This renormalization technique is the most "correct" method of renormalization, but is very expensive as each track is renormalized separately. It is also more difficult to implement, as the analytic area of each track-segment must be found. To the best of our knowledge, this method is not implemented in any production-level MoC code.

Direction-volume preservation is the next "most-correct" renormalization technique. In this method, every mono-directional spatial integration should preserve the cell volume, i.e.

$$\langle 1 \rangle_{mi} = 1. \tag{3.17}$$

This constraint leads to the renormalization factor given by

$$\xi_{mi} = \frac{V_i}{\sum_k \delta A_{mki} s_{mki}}. \tag{3.18}$$

This method is significantly less expensive in terms of memory, computational time, and difficulty of implementation.

The simplest renormalization technique, volume preservation, only preserves the volume over the spatial and directional integration, i.e.

$$\langle 1 \rangle_i = 4\pi. \tag{3.19}$$

This constraint leads to the renormalization factor given by

$$\xi_i = \frac{V_i}{\sum_m w_m \sum_k \delta A_{mki} s_{mki}}. \tag{3.20}$$

Renormalization is not the only technique used for volume preservation. Another method is to use the numerical volume, $\sum_k \delta A_{mki} s_{mki}$ in place of V_i in Eq. (3.12). This seems to be a more consistent method; however, a detailed comparison of these methods has not taken place, to the best of our knowledge. The renormalization technique generally seems to be the faster approach, and is the approach used in MPACT [3], which is used extensively in this work.

3.2 The Flat-Source Approximation

The simplest approximation to the spatial shape of the source, $q^g_{mi}(\boldsymbol{x})$, within each cell is the flat-source approximation (FSA). The MoC has been widely used in lattice physics and neutron transport codes [4], many of which have utilized the flat-source method of characteristics (FSMoC) [2, 3, 5–10].

3.2.1 Derivation

The FSA is simply the assumption that within each cell, $\mathcal{R}_i$, the source, $q^g_{mi}(\boldsymbol{x})$, is uniform. This can be expressed as

$$q^g_{mi}(\boldsymbol{x}) \approx q^g_{mi} = q^g_i + \sum_{\ell=0}^{L} \sum_{n=-\ell}^{\ell} R^n_\ell(\widehat{\boldsymbol{\Omega}}_m) q^{g,n}_{i,\ell} \tag{3.21}$$

Thus, to get a source in this form, Eq. (3.3) requires that the region averaged scalar flux and higher-order angular moments (up to order L) be determined. In mathematical terms, the flat-source can be determined as

$$q^g_{mi} = \left[\sum_{g'} \sum_{\ell=0}^{L} \sum_{n=-\ell}^{\ell} R^n_\ell(\widehat{\boldsymbol{\Omega}}_m) \Sigma^{g'\to g}_{s,\ell,i} \Phi^{\ell,g'}_{i,n} + \frac{\chi^g_i}{k_{\text{eff}}} \sum_{g'} \nu \Sigma^{g'}_{f,i} \phi^{g'}_i \right], \tag{3.22}$$

where the $\phi_i^{g'}$ is the region-averaged scalar flux, and $\Phi_{i,n}^{\ell,g'}$ are the region-averaged angular moments of the flux.

In order to get these region-averaged flux moments, the spatial and directional integration operators, introduced in Section 3.1.1, are used. The region-averaged scalar flux is given by

$$\phi_i^g = \langle \psi^g \rangle_i = \frac{4\pi}{V_i} \sum_m w_m \sum_k t_{mki} \delta A_{mki} \langle \psi^g \rangle_{mki}, \tag{3.23a}$$

and the higher-order angular moments of the flux are given by

$$\Phi_{i,n}^{\ell,g} = \left\langle R_\ell^n(\widehat{\mathbf{\Omega}}) \psi^g \right\rangle_i = \frac{4\pi}{V_i} \sum_m w_m R_\ell^n(\widehat{\mathbf{\Omega}}_m) \sum_k t_{mki} \delta A_{mki} \langle \psi^g \rangle_{mki}. \tag{3.23b}$$

To evaluate these flux moments, the track-averaged angular flux, $\langle \psi^g \rangle_{mki}$, must be found. By applying the FSA, Eq. (3.6) becomes

$$\left[\frac{\mathrm{d}}{\mathrm{d}t_m} + \Sigma_{t,i}^g \right] \psi_{mki}^g(t_m) = \overline{q}_{mi}^g, \tag{3.24}$$

where

$$\overline{q}_{mi}^g \equiv \frac{1}{4\pi} q_{mi}^g. \tag{3.25}$$

This can be solved analytically for the angular flux along the track,

$$\psi_{mki}^g(t_m) = \psi_{mki}^{g,\text{in}} + \left(\frac{\overline{q}_{mi}^g}{\Sigma_{t,i}^g} - \psi_{mki}^{g,\text{in}} \right) F_1(\tau_m^g), \tag{3.26a}$$

where

$$F_1(\tau_m^g) \equiv 1 - \exp(-\tau_m^g), \tag{3.26b}$$

and τ_m^g is the (renormalized) optical thickness,

$$\tau_m^g \equiv t_m \Sigma_{t,i}^g. \tag{3.26c}$$

One approach to find $\langle \psi^g \rangle_{mki}$, is to perform integration of Eq. (3.26a) to evaluate the track-average value, resulting in

$$\langle \psi^g \rangle_{mki} = \frac{\overline{q}_{mi}^g}{\Sigma_{t,i}^g} - \left(\frac{\overline{q}_{mi}^g}{\Sigma_{t,i}^g} - \psi_{mki}^{g,\text{in}} \right) \frac{F_1(\tau_{mki}^g)}{\tau_{mki}^g}. \tag{3.27}$$

This approach will be referred to as *explicit*, as the moment's integral is explicitly evaluated. Another, approach, which in the author's opinion is simpler, is use the track-averaging operator on

the characteristic form of the transport equation, Eq. (3.24), which simplifies to

$$\langle \psi^g \rangle_{mki} = \frac{\overline{q}^g_{mi}}{\Sigma^g_{t,i}} + \frac{\psi^{g,\text{in}}_{mki} - \psi^{g,\text{out}}_{mki}}{\tau^g_{mki}}. \tag{3.28}$$

This approach will be referred to as *implicit*, as the moment's integral is not explicitly evaluated. Note, that the resulting forms of these two approaches are equivalent; by evaluating the outgoing flux in Eq. (3.26a) at the outgoing position, Eq. (3.28) can be put into the form of Eq. (3.27). By substituting the track-averaged angular flux in Eqs. (3.23), the flux moments can be evaluated, and used to compute the source. A transport calculation may be carried out using the source iteration algorithm defined by Algorithm 1.

3.2.2 Particle Conservation

The neutron transport equation, Eq. (2.1), is a statement of particle balance within the defined phase-space. Previous works [11, 12] have examined the FSMoC with respect to *particle conservation*. Le Tellier and Hébert [11] defined necessary constraints on the directional quadrature and the characteristic tracks (trajectories) in order to ensure particle conservation for the anisotropic FSMoC. The constraints can be found by requiring

$$\frac{1}{4\pi}\left\langle R^n_\ell(\widehat{\mathbf{\Omega}}) q^g_{mi} \right\rangle_i = q^{g,n}_{i,\ell}. \tag{3.29}$$

Substituting Eq. (3.21) into Eq. (3.29), requires that

$$\sum_m w_m R^n_\ell(\widehat{\mathbf{\Omega}}_m) R^{n'}_{\ell'}(\widehat{\mathbf{\Omega}}_m) = \delta_{\ell\ell'}\delta_{nn'}, \tag{3.30a}$$

and

$$\sum_k t_{mki}\delta A_{mki} = V_i. \tag{3.30b}$$

Equation (3.30a) is a constraint on the directional quadrature, requiring orthogonality of the real spherical harmonics [11]. Equation (3.30b) requires that *at least* direction-dependent renormalization, Eq. (3.18), be used.

If the constraints on directional quadrature, and characteristic tracks, are satisfied several simplifications to Eqs. (3.23) are possible.

$$\phi^g_i = \frac{q^g_i}{\Sigma^g_{t,i}} + \frac{4\pi}{V_i \Sigma^g_{t,i}} \sum_m w_m \sum_k \delta A_{mki} \Delta\psi^g_{mki}, \tag{3.31a}$$

$$\Phi_{i,n}^{\ell,g} = \frac{q_{i,\ell}^{g,n}}{\Sigma_{t,i}^{g}} + \frac{4\pi}{V_i \Sigma_{t,i}^{g}} \sum_m w_m R_\ell^n(\widehat{\mathbf{\Omega}}_m) \sum_k \delta A_{mki} \Delta\psi_{mki}^{g}, \tag{3.31b}$$

where

$$\Delta\psi_{mki}^{g} \equiv \psi_{mki}^{g,\text{in}} - \psi_{mki}^{g,\text{out}}. \tag{3.31c}$$

3.2.3 Isotropic Simplifications

While anisotropic scattering is necessary for accurate calculations, it is also common for isotropic source calculations to be performed. Typically, these account for anisotropic behavior by using the transport-corrected P_0 (TCP0) approximation [13]. While not as accurate as truly anisotropic calculations, use of an isotropic source results in significantly fewer calculations, and allows for additional simplifications to be made.

Equation (3.29) is now only of concern for the isotropic component of the source. This results in the following constraint,

$$\sum_m w_m \sum_k t_{mki} \delta A_{mki} = V_i, \tag{3.32}$$

which is equivalent to the direction-independent renormalization, given by Eq. (3.20). These isotropic calculations become significantly less expensive, as only the scalar flux needs to be computed.

3.2.4 Applications

The FSMoC has been utilized in many MoC production codes [2, 3, 5–10]. However, previous studies on the FSMoC have found that a fine mesh must be used to obtain accurate results, particularly in the presence of control rods or blades, strong absorber rods, gadolinia poisoned fuel rods [14], as well as in the presence of large reflector regions (such as in critical experiments) [15]. As the number of mesh elements increase, so does the number of track-segments (on which the MoC computations are performed). This results in large run-times, and has motivated the development of linear-source approximations (LSAs) to the MoC, that are discussed in detail in Section 3.3.

3.3 The Linear-Source Approximation

3.3.1 Overview

The linear-source approximation (LSA), in the MoC, assumes the shape of the source along a characteristic track-segment is linear. There has long been motivation for the development of LSAs for the MoC, as previous work [16] indicated that a spatially linear source was able to achieve faster computational performance in S_N calculations. There have been many different variants of this approximation. The first instance of the LSA was the *gradient source approximation* introduced by Halsall [17]. This early linear-source method of characteristics (LSMoC) was based on the averaging of the angular flux gradient along tracks, and was implemented in the WIMS [17], and PEACH [18] MoC transport codes. These averaged gradients were then used as estimates to the gradient of the scalar flux, which were used to compute the source shape as spatially linear.

Petkov and Takeda devised a LSA that estimated the gradient of the scalar flux based on the P_1 approximation in the MARIKO code [14, 19]. In this approximation, the gradient of the scalar flux is computed from the neutron current, the total cross section, and the linearly anisotropic scattering matrix:

$$\boldsymbol{\nabla}\phi_i^g \approx -3\left(\Sigma_{t,i}^g \boldsymbol{J}_i^g - \sum_{g'} \Sigma_{s,1,i}^{g'\to g}\boldsymbol{J}_i^{g'}\right). \tag{3.33}$$

A similar approach, using the diffusion approximation to compute the scalar flux gradient, was used in the so called "quasi-linear" source implemented by Rabiti et al. [20]. In this approach, the $\Sigma_{s,1,i}^{g'\to g}$ matrix is diagonalized, turning the P_1 approximation into the diffusion approximation. Due to their basis on the P_1 and diffusion approximations, these early LSAs are inaccurate in situations where more transport-like effects are present. It can be shown, even in simple cases, that this approximation can be predict the opposite direction for the scalar flux gradient.

Santandrea and Sanchez [21] introduced the positive linear and nonlinear surface characteristics scheme, which constructed a linear source by interpolating between source values on the surfaces of cell regions. Various improvements have been made to this surface characteristics scheme for conservation [21], as well as coupling in APOLLO2 [22]. Le Tellier and Hébert [23] introduced a simplification to the linear characteristics scheme for conservation, by using a diamond-differencing scheme. This work was extended by Hébert [24], to include higher-order diamond difference schemes, as well as allowing for acceleration [25].

The most recent LSA examined in this work was introduced as a 2-D general high-order method for unstructured meshes by Masiello et al. [26]. The approximation uses track-based integration, defined in Section 3.1.1, in order to compute spatial moments of the angular flux. This LSA was shown to reduce memory and computation times in 3-D MoC calculations [27]. The general

method was simplified in the case of the isotropic and anisotropic LS by Ferrer and Rhodes [15]; this also introduced the "LS-P0" method in which the isotropic source is spatially linear, but the anisotropic source components are spatially uniform within each cell. This LSA was also shown to be consistent with particle conservation, under certain constraints, and shown to be compatible with CMFD acceleration [12].

This thesis work has made extensive use of this LSA, and has made improvements upon the method. For this reason, in the following section the formulation prior to the work of this thesis is derived.

3.3.2 Derivation

The moment-based LSA assumes the shape of the source, $q^g_{mi}(\boldsymbol{x})$, is spatially linear within each cell, $\mathcal{R}_i$. This can be expressed as

$$q^g_{mi}(\boldsymbol{x}) \approx q^g_{mi} + \boldsymbol{x} \cdot \widehat{\underline{\boldsymbol{q}}}^g_{mi}, \tag{3.34a}$$

where $\widehat{\underline{\boldsymbol{q}}}^g_{mi}$ is a column vector of source spatial expansion coefficients,

$$\widehat{\underline{\boldsymbol{q}}}^g_{mi} \equiv \begin{bmatrix} \widehat{q}^g_{mi,x} \\ \widehat{q}^g_{mi,y} \\ \widehat{q}^g_{mi,z} \end{bmatrix}, \tag{3.34b}$$

and $\boldsymbol{x}$ is the position in *local* coordinates. A similar spatial expansion of the angular moments of the flux can be performed,

$$\phi^{\ell,g}_{i,n}(\boldsymbol{x}) = \overline{\phi}^{\ell,g}_{i,n} + \boldsymbol{x} \cdot \widehat{\underline{\boldsymbol{\phi}}}^{\ell,g}_{i,n}, \tag{3.35}$$

the source can then be expressed as

$$q^g_{mi}(\boldsymbol{x}) = \sum_{g'} \sum_{\ell=0}^{L} \sum_{n=-\ell}^{\ell} R^n_\ell(\widehat{\boldsymbol{\Omega}}_m) \Sigma^{g' \to g}_{s,\ell,i} \phi^{\ell,g'}_{i,n}(\boldsymbol{x}) + \frac{\chi^g_i}{k_{\text{eff}}} \sum_{g'} \nu \Sigma^{g'}_{f,i} \phi^{g'}_i(\boldsymbol{x}), \tag{3.36}$$

and the linear expansion coefficients are explicitly given by

$$\widehat{\underline{\boldsymbol{q}}}^g_{mi} = \sum_{g'} \sum_{\ell=0}^{L} \sum_{n=-\ell}^{\ell} R^n_\ell(\widehat{\boldsymbol{\Omega}}_m) \Sigma^{g' \to g}_{s,\ell,i} \widehat{\underline{\boldsymbol{\phi}}}^{\ell,g'}_{i,n} + \frac{\chi^g_i}{k_{\text{eff}}} \sum_{g'} \nu \Sigma^{g'}_{f,i} \widehat{\underline{\boldsymbol{\phi}}}^{g}_{g'}. \tag{3.37}$$

In the spatial moment-base LSA, it is convenient to define the spatially linear source (and flux) in terms of a cell-local coordinate system. Allow $\boldsymbol{X}$ to be the position variable in the global coordinate

system, the local coordinates are then defined as

$$\boldsymbol{x} = \boldsymbol{X} - \boldsymbol{X}^{\mathrm{c}}_{mi}, \tag{3.38}$$

where $\boldsymbol{X}^{\mathrm{c}}_{mi}$ is the numerical centroid of the cell i.

These numerical centroids can be defined as either direction-dependent, or direction-independent, which will have implications on particle conservation, as is discussed in Section 3.3.3. The direction-dependent centroids are defined by

$$\boldsymbol{X}^{\mathrm{c}}_{mi} \equiv \langle \boldsymbol{X} \rangle_{mi} = \frac{1}{V_i} \sum_k \delta A_{mki} t_{mki} \boldsymbol{X}^{\mathrm{c}}_{mki}, \tag{3.39}$$

where $\boldsymbol{X}^{\mathrm{c}}_{mki}$ is the global coordinate vector of the track-segment mid-point. Similarly, the direction-independent centroids are defined by

$$\boldsymbol{X}^{\mathrm{c}}_{i} \equiv \frac{1}{4\pi} \langle \boldsymbol{X} \rangle_{i} = \frac{1}{V_i} \sum_m w_m \sum_k \delta A_{mki} t_{mki} \boldsymbol{X}^{\mathrm{c}}_{mki}. \tag{3.40}$$

Following the same approach as the FSMoC derivation, in Section 3.2.1, computing the source requires the region-averaged flux moments, $\overline{\phi}^{\ell,g}_{i,n}$, and the flux expansion coefficients, $\underline{\widehat{\phi}}^{\ell,g}_{i,n}$. The region-averaged flux moment can be found using the same definition as previously,

$$\overline{\phi}^{\ell,g}_{i,n} \equiv \left\langle R^n_\ell(\widehat{\boldsymbol{\Omega}}) \psi^g \right\rangle_i = \frac{4\pi}{V_i} \sum_m w_m R^n_\ell(\widehat{\boldsymbol{\Omega}}_m) \sum_k \delta A_{mki} t_{mki} \langle \psi^g \rangle_{mki}. \tag{3.41a}$$

In order to determine the spatial expansion coefficients of the flux moments, Eq. (3.35) is operated on by $\left\langle R^n_\ell(\widehat{\boldsymbol{\Omega}}) \boldsymbol{x}(\cdot) \right\rangle_i$. Recognizing that this should be directly proportional to angular flux operated on by $\left\langle R^n_\ell(\widehat{\boldsymbol{\Omega}}) \boldsymbol{x} \psi^g \right\rangle_i$, a system of equations is found

$$\boldsymbol{M}_i \underline{\widehat{\boldsymbol{\phi}}}^{\ell,g}_{i,n} = \left\langle R^n_\ell(\widehat{\boldsymbol{\Omega}}) \boldsymbol{x} \psi^g \right\rangle_i, \tag{3.41b}$$

where

$$\boldsymbol{M}_i \equiv \left\langle \boldsymbol{x}^T \boldsymbol{x} \right\rangle_i. \tag{3.41c}$$

The spatial angular flux moments, $\left\langle R^n_\ell(\widehat{\boldsymbol{\Omega}}) \boldsymbol{x} \psi^g \right\rangle_i$, are then defined as

$$\left\langle R^n_\ell(\widehat{\boldsymbol{\Omega}}) \boldsymbol{x} \psi^g \right\rangle_i = \frac{4\pi}{V_i} \sum_m w_m R^n_\ell(\widehat{\boldsymbol{\Omega}}_m) \sum_k \delta A_{mki} t_{mki} \left(\boldsymbol{x}^{\mathrm{in}}_{mki} \langle \psi^g \rangle_{mki} + \widehat{\boldsymbol{\Omega}}_m \langle t_m \psi^g \rangle_{mki} / \xi_{mi} \right). \tag{3.41d}$$

In order to evaluate the flux moments defined in Eqs. (3.41), the track-averaged angular flux

values, $\langle \psi^g \rangle_{mki}$, and $\langle t_m \psi^g \rangle_{mki}$, must be determined. First, the transport equation must be put into characteristic form, using Eq. (3.16c) the spatially expanded source, Eq. (3.34a), can be defined along the characteristic. The characteristic transport equation becomes

$$\left[\frac{\mathrm{d}}{\mathrm{d}t_m} + \Sigma_{t,i}^g\right] \psi_{mki}^g(s) = \overline{q}_{mki}^g + \widehat{q}_{mi}^g \left(t_m - \frac{t_{mki}}{2}\right), \tag{3.42a}$$

where

$$\overline{q}_{mki}^g \equiv \frac{1}{4\pi}\left[q_{mi}^g + \boldsymbol{x}_{mki}^{\mathrm{c}} \cdot \underline{\widehat{\boldsymbol{q}}}_{mi}^g\right], \tag{3.42b}$$

$$\widehat{q}_{mi}^g \equiv \frac{1}{4\pi}\left[\frac{\widehat{\boldsymbol{\Omega}}_m \cdot \underline{\widehat{\boldsymbol{q}}}_{mi}^g}{\xi_{mi}}\right], \tag{3.42c}$$

and $\boldsymbol{x}_{mki}^{\mathrm{c}}$ is the local-coordinate centroid of the track-segment. Substituting this assumed source shape (linear) into the generic MoC solution, given by Eq. (3.9), the angular flux along a track-segment is found to be

$$\psi_{mki}^g(s) = \psi_{mki}^{g,\mathrm{in}} + \left(\frac{\overline{q}_{mki}^g}{\Sigma_{t,i}^g} - \psi_{mki}^{g,\mathrm{in}}\right) F_1(\tau_m^g) + \frac{\widehat{q}_{mi}^g}{2(\Sigma_{t,i}^g)^2} F_2(\tau_m^g), \tag{3.43a}$$

where

$$F_1(\tau_m^g) \equiv 1 - \exp(-\tau_m^g), \tag{3.43b}$$

and

$$F_2(\tau_m^g) \equiv 2[\tau_m^g - F_1(\tau_m^g)] - \tau_{mki}^g F_1(\tau_m^g). \tag{3.43c}$$

As discussed in Section 3.2.1, there are two *equivalent* methods with which one could determine the track-averaged angular flux values. The original derivation of the LSA method by Ferrer and Rhodes [15] used the *implicit* definition for the track-average angular flux, but the *explicit* definition for the first spatial moment of the angular flux. In Chapter 5, the implicit definition is taken for the first spatial moment of the angular flux as well, which allows for additional improvements for the method in multi-physics and 2D/1D applications. For the remainder of this section, the formulation as it was originally derived by Ferrer and Rhodes [15] is shown, using the explicit form of $\langle t_m \psi^g \rangle_{mki}$.

The implicitly defined track-average flux is given by operating on Eq. (3.42a) by $\langle (\cdot) \rangle_{mki}$, and the explicitly defined first spatial moment of the angular flux is given by operating on Eq. (3.43a) by $\langle t_m (\cdot) \rangle_{mki}$. These are shown in Eqs. (3.44).

$$\langle \psi^g \rangle_{mki} = \frac{\overline{q}_{mki}^g}{\Sigma_{t,i}^g} + \frac{\Delta\psi_{mki}^g}{\tau_{mki}^g}, \tag{3.44a}$$

and

$$\langle t_m \psi^g \rangle_{mki} = \psi^{g,\text{in}}_{mki} \frac{t_{mki}}{2} + \left(\frac{\overline{q}^g_{mki}}{\Sigma^g_{t,i}} - \psi^{g,\text{in}}_{mki} \right) \frac{G_1(\tau^g_{mki})}{\Sigma^g_{t,i}} + \frac{\widehat{q}^g_{mi}}{2(\Sigma^g_{t,i})^2} t_{mki} G_2(\tau^g_{mki}). \tag{3.44b}$$

Here

$$G_1(\tau^g_{mki}) \equiv 1 + \frac{\tau^g_{mki}}{2} - \left(1 + \frac{1}{\tau^g_{mki}} \right) F_1(\tau^g_{mki}), \tag{3.45a}$$

and

$$G_2(\tau^g_{mki}) \equiv \frac{2}{3} \tau^g_{mki} - \left(1 + \frac{2}{\tau^g_{mki}} \right) G_1(\tau^g_{mki}). \tag{3.45b}$$

The original derivation further simplified Eqs. (3.41) into the following forms.

$$\overline{\phi}^{\ell,g}_{i,n} = \frac{4\pi}{\Sigma^g_{t,i} V_i} \sum_m w_m R^n_\ell(\widehat{\boldsymbol{\Omega}}_m) \Sigma^g_{t,i} \Psi^g_{mi}, \tag{3.46a}$$

$$\left\langle \boldsymbol{x} R^n_\ell(\widehat{\boldsymbol{\Omega}}) \psi^g \right\rangle_i = \frac{4\pi}{\Sigma^g_{t,i} V_i} \sum_m w_m R^n_\ell(\widehat{\boldsymbol{\Omega}}_m) \Sigma^g_{t,i} \left(\boldsymbol{\Psi}^g_{mi} + \widehat{\boldsymbol{\Omega}}_m \widehat{\Psi}^g_{mi} / \xi_i \right), \tag{3.46b}$$

where

$$\Psi^g_{mi} \equiv \frac{1}{\Sigma^g_{t,i}} \left[\frac{q^g_{mi}}{4\pi} \sum_k \delta A_{mki} t_{mki} + \frac{\widehat{\boldsymbol{q}}^g_{mi}}{4\pi} \cdot \sum_k \delta A_{mki} \boldsymbol{x}^{\text{c}}_{mki} t_{mki} + \sum_k \delta A_{mki} \Delta \psi^g_{mki} \right], \tag{3.47a}$$

$$\begin{aligned} \boldsymbol{\Psi}^g_{mi} \equiv \frac{1}{\Sigma^g_{t,i}} \Bigg[& \left(\sum_k \delta A_{mki} t_{mki} \boldsymbol{x}^{\text{in}}_{mki} \right) \frac{q^g_{mi}}{4\pi} + \left(\sum_k \delta A_{mki} t_{mki} \boldsymbol{x}^{\text{in}}_{mki} (\boldsymbol{x}^{\text{c}}_{mki})^T \right) \frac{\widehat{\boldsymbol{q}}^g_{mi}}{4\pi} \\ & + \sum_k \delta A_{mki} \boldsymbol{x}^{\text{in}}_{mki} \Delta \psi^g_{mki} \Bigg], \end{aligned} \tag{3.47b}$$

and

$$\widehat{\Psi}^g_{mi} \equiv \frac{1}{\Sigma^g_{t,i}} \left[\frac{q^g_{mi}}{4\pi} C^g_{mi} + \frac{\widehat{\boldsymbol{q}}^g_{mi}}{4\pi} \cdot \boldsymbol{C}^g_{mi} + \sum_k \delta A_{mki} t_{mki} \psi^{g,\text{in}}_{mki} H(\tau^g_{mki}) \right], \tag{3.47c}$$

where

$$C^g_{mi} \equiv \frac{1}{\Sigma^g_{t,i}} \sum_k \delta A_{mki} t_{mki} G_1(\tau^g_{mki}), \tag{3.48a}$$

$$\boldsymbol{C}^g_{mi} \equiv \frac{1}{\Sigma^g_{t,i}} \sum_k \delta A_{mki} t_{mki} \left(\boldsymbol{x}^{\text{c}}_{mki} G_1(\tau^g_{mki}) + \widehat{\boldsymbol{\Omega}}_m \frac{s_{mki}}{2} G_2(\tau^g_{mki}) \right), \tag{3.48b}$$

and

$$H(\tau^g_{mki}) \equiv \frac{\tau^g_{mki}}{2} - G_1(\tau^g_{mki}). \tag{3.49}$$

The C^g_{mi} and $\boldsymbol{C}^g_{mi}$ are dependent on both the energy group, g, and direction m, for each region, i.

If these terms are stored, this leads to considerable memory usage, and will often use more memory than the flux moments that are of interest. If cross sections are constant in the problem (no feedback, or 2D/1D transverse leakage splitting), these coefficients can be pre-computed once at the outset of the simulation. However, if this is not the case, these coefficients must be re-evaluated each time there is a change in cross sections. The re-evaluation of these coefficients can lead to significant overhead. In cases with T/H feedback, cross sections typically change each iteration.

3.3.3 Particle Conservation

When considering particle conservation, use of the LSA results in additional constraints on the calculations. Similarly to Section 3.2.2, the track-based integration of the source must exactly integrate to the spatial and angular moments of the source. The conservation of spatial moments is the basis of this LSA [12], so this constraint is satisfied without additional constraints on the method. The angular moment constraint is expressed as

$$\frac{1}{4\pi}\left\langle R_\ell^n(\widehat{\boldsymbol{\Omega}})q_{mi}^g(\boldsymbol{x})\right\rangle_i = q_{i,\ell}^{g,n}. \tag{3.50}$$

In addition to the constraints introduced in Section 3.2.2, namely direction-dependent renormalization, and directional quadrature restrictions, there is a constraint on the definition of the local coordinate system:

$$\langle \boldsymbol{x}\rangle_{mi} = 0. \tag{3.51}$$

This is equivalent to stating that the local coordinate system must be defined with respect to direction-dependent global centroids, as is given by Eq. (3.39).

3.3.4 Isotropic Simplifications

Ferrer and Rhodes [15] suggested that allowing only the flat source components to consider anisotropic scattering has performance benefits, while not significantly affecting accuracy. It was demonstrated for the Babcox and Wilcox (B&W) experiments [28] that considering anisotropic scattering only with spatially flat flux moments resulted in approximately 10 pcm error. Furthermore, by making this simplification, run-times were reduced significantly (up to 45%), while memory savings were even more significant (up to 89%) [15].

As stated in Section 3.2.3, it is very common in reactor simulations to use TCP0 cross-sections (which are isotropic). Assuming isotropic scattering, Eqs. (3.46) become

$$\phi_i^g = \frac{q_i^g}{\Sigma_{t,i}^g} + \frac{4\pi}{\Sigma_{t,i}^g V_i}\sum_m w_m \sum_k \delta A_{mki}\Delta\psi_{mki}^g, \tag{3.52a}$$

$$\langle \boldsymbol{x}\psi^g \rangle_i = \boldsymbol{C}_i^g \frac{\widehat{\boldsymbol{q}}_i^g}{\Sigma_{t,i}^g} + \frac{4\pi}{\Sigma_{t,i}^g V_i} \sum_m w_m \sum_k \delta A_{mki} \left[\boldsymbol{x}_{mki}^{\text{in}} \Delta\psi_{mki}^g + \widehat{\boldsymbol{\Omega}}_m s_{mki} \psi_{mki}^{g,\text{in}} H(\tau_{mki}^g) \right], \quad (3.52b)$$

where

$$\boldsymbol{C}_i^g \equiv \frac{1}{\Sigma_{t,i}^g V_i} \sum_{m/2} w_m \sum_k \delta A_{mki} \widehat{\boldsymbol{\Omega}}_m \widehat{\boldsymbol{\Omega}}_m^T s_{mki}^2 G_2(\tau_{mki}^g) + \frac{2}{V_i} \sum_{m/2} wt \sum_k \delta A_{mki} \boldsymbol{x}\boldsymbol{x}^T t_{mki}. \quad (3.53)$$

These $\boldsymbol{C}_i^g$ coefficients are no longer dependent on the direction, but still require significant memory usage; using more than the memory requirements of the scalar flux coefficients. However, these coefficients are still dependent on the energy group, and the same inefficiencies mentioned previously are present if cross sections are not constant through the simulation.

3.3.5 Applications

Various different LSAs to the MoC have been developed and implemented in transport codes [10, 14, 15, 17, 18, 20, 21, 29]. Results have indicated that by using a LSA, the spatial mesh discretization can be made coarser, relative to the FSA, while maintaining transport accuracy. Although each segment calculation is more expensive when using a LSA, the number of calculations (due to the coarser spatial mesh) can be significantly reduced, leading to reduced run-times. Additionally, the reduction in spatial mesh elements generally reduces the amount of memory used by the calculation.

3.4 Ray-Tracing

The Method of Characteristics (MoC) [1] is based on solving the transport equation along many characteristic tracks or rays. These rays are followed through the reactor geometry in a process generally referred to as "ray-tracing". The placement and storage of these tracks is significant with respect to both calculation accuracy as well as computational performance. This section serves to give an overview of the current state-of-the-art ray-tracing methods used for MoC-like transport calculations.

3.4.1 Modular Ray-Tracing

The most straight-forward approach to perform a MoC calculation is to create rays which span the domain of the transport problem being solved. However, in this approach, the information of each ray-segment must be stored, or computed on-the-fly. In large problems the number of ray-segments can become exceedingly large, and this approach is not feasible due to memory constraints.

This led to the development of so-called "modular" ray-tracing methods [6, 30–32], in which the regularity of reactor designs is utilized to reduce memory usages. In typical reactor designs, certain geometries (like assemblies) are repeated throughout the core. Rather than laying tracks down for the global geometry, the transport problem is partitioned into "modules" which represent a small often repeated geometries in the problem. The ray-tracing data is generated for each module, in such a way there is direct linking of tracks on module interfaces; this is the direct neutron path linking (DNPL) technique devised by Kosaka and Saji [6]. This significantly reduces the amount of ray-tracing data that needs to be stored in MoC calculations, and has been widely adopted in MoC transport codes [5, 18, 33–37]. Tracks spanning the global domain are then constructed by connecting multiple modular rays, as is depicted in Fig. 3.3.

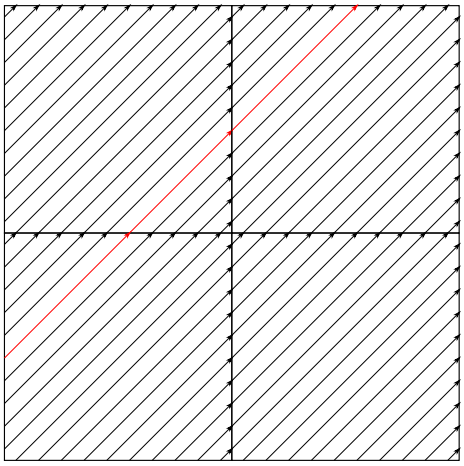

Figure 3.3: Depiction of modular ray-tracing method. Global (long) rays can be constructed by connecting multiple modular rays, as is shown in red.

The modular ray-tracing technique, with DNPL, requires that the number of tracks on a modular boundary is an integer. This additionally requires that all modules have the same spatial dimensions, given by the pitches P_x and P_y, and that the spacing between all tracks in a direction are constant. Let δA_{a0} be the desired ray-spacing for an azimuthal angle a, and φ_{a0} be the desired azimuthal angle. The number of rays on the x and y module boundaries can be determined as

$$N_x = \left\lceil \frac{P_x \sin(\varphi_{a0})}{\delta A_{a0}} \right\rceil, \tag{3.54a}$$

and

$$N_y = \left\lceil \frac{P_x \cos(\varphi_{a0})}{\delta A_{a0}} \right\rceil. \tag{3.54b}$$

The x and y distance between rays can be determined by

$$\delta_x = \frac{P_x}{N_x}, \tag{3.55a}$$

and

$$\delta_y = \frac{P_y}{N_y}. \tag{3.55b}$$

The azimuthal angle is then "corrected" to represent the true angle at which the rays are placed,

$$\varphi_a = \tan^{-1}\left(\frac{\delta_y}{\delta_x}\right), \tag{3.56}$$

and the corrected ray-spacing is then given by

$$\delta A_a = \delta_x \sin(\varphi_a). \tag{3.57}$$

Due to the constraint of DNPL, the directional quadrature is perturbed in the process of ray-tracing. As described in Section 3.2.2, this has implications on particle conservation in calculations. To maintain accuracy, a higher-order directional quadrature may need to be used would otherwise have been necessary.

3.4.2 Mobile Chords

The mobile chord method was introduced by Villarino et al. [38] in the HELIOS code for CP calculations, and adapted to the MoC by Yamamoto [39]. In the typical equidistant ray-tracing method, a ray is placed at the center of the ray-width. The mobile chord method offsets the ray from the center, with differing offsets in each direction. This has generally shown to be more accurate than the typical equidistant ray-tracing method [39], but is not directly compatible with the DNPL technique. While ray widths are still linked, the ray-traces are not; though, this does not seem to introduce significant discretization errors [39].

3.4.3 Macroband

The *macroband* method was originally proposed by Villarino et al. [38] for CP calculations in HELIOS. In this method, characteristic rays placed within "macrobands" which are separated by tangential and intersection points in the mesh. There is no material or geometric discontinuities within each macroband segment (macrosegment), and thus the direction-of-flight averaged angular flux in each macrosegment is smooth with regards to the transverse direction. Since integration in

the MoC is akin to a quadrature integration, this indicates that a more advanced quadrature, for ray placement and width, can be used to reduce discretization error [40].

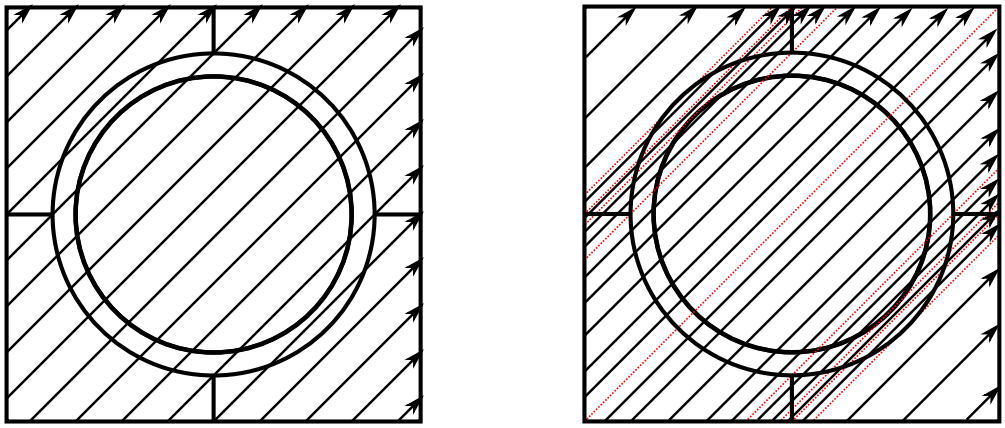

(a) Equidistant (b) Macroband

Figure 3.4: Visualization of hypothetical tracks for (a) equidistant and (b) macroband ray-tracing methods. Boundaries between macrobands are shown as red dotted lines.

The modular ray-tracing (MRT) ray-tracing technique does not consider the internal geometry when laying down tracks. For a specified ray-spacing and module size, the tracks are the same regardless of the internal mesh. The macroband takes an entirely different approach, and the internal mesh is the primary guide for laying down the tracks.

Macrobands are determined by the computational mesh; for large heterogeneous assemblies, this results in very thin macrobands, which would result in significantly increased computation time. In the related CDP Hong and Cho [41] proposed that macroband ray-tracing data only be generated on unique subsystems. Similarly, Yamamoto et al. [40] proposed the memory reduction technique for macroband (MRMB) in which macroband ray-tracing data is only generated for unit-cells. These techniques are similar to the modular ray-tracing technique in that ray-tracing data is only generated for unique subsystems, which significantly reduces the amount of ray-tracing data. The macroband ray-tracing process is displayed for a single pin-cell mesh in Fig. 3.5.

However, these techniques are fundamentally incompatible with the DNPL technique, at thus an approximation of angular flux must be made on subsystem interfaces. Yamamoto et al. [40] proposed linearly interpolating the angular flux on cell boundaries, though other techniques involving averaging the angular flux on sub-boundaries have been utilized in the CDP [42]. Alternatively, these methods do not require adjustment to the angular quadrature.

Yamamoto et al. [40] found that the macroband method (using a Gauss-Legendre quadrature for ray placement), was more accurate than conventional ray-tracing methods with equidistant ray-spacing. Févotte et al. [43] proposed a new tracking technique similar to the macroband

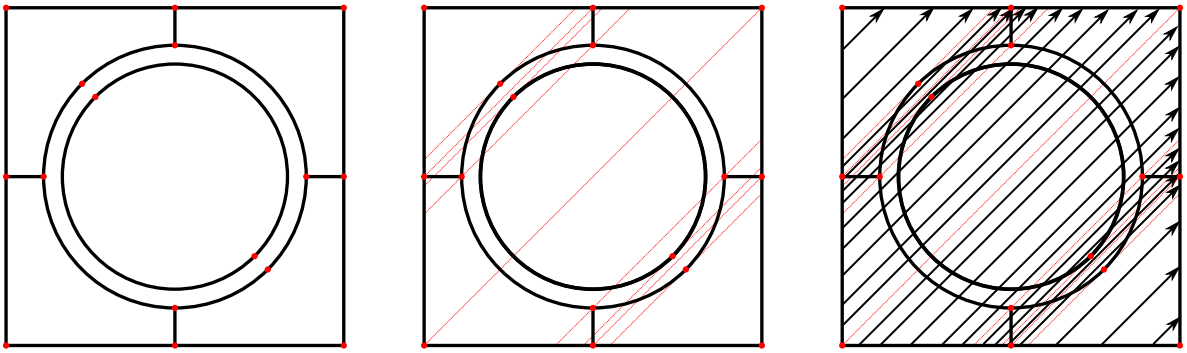

(a) Determine intersection and tangent points

(b) Determine macroband boundaries (through identified points)

(c) Perform ray-tracing within macroband boundaries

Figure 3.5: Ray-tracing process for macroband.

method, in which rays (placed equidistantly) are divided into sub-bands, which are effectively *locally* projected macrobands, and the average flux of the sub-bands is propagated along each ray. Studies of ray-spacing with macroband, and Févotte et al.'s [43] method, have indicated that coarser ray-spacing can be used while maintaining accuracy [39, 40, 43].

3.4.3.1 Interface Flux Approximations

The macroband ray-tracing method is fundamentally incompatible with direct neutron path linking (DNPL). Although ray-tracing can be performed on small unique subsystems, similarly to the MRT method, the rays on module interfaces are no longer guaranteed to align. This makes it necessary for an approximation of the spatial dependence of the angular flux on these interfaces. However, there are multiple different options for performing this approximation.

Yamamoto et al. [40] proposed performing a linear of the flux on these interfaces. However, without adjustment, linear interpolation will not preserve the total flux passing through the surface; which is an important aspect when considering acceleration techniques such as CMFD. For 3-D CDP with uniformly spaced rays, Liu et al. [42] proposed a sub-boundary averaging method. This method partitioned each interface into sub-boundaries, with the size depending on the interface and the direction; each sub-boundary represented a single angular flux value for each energy group, that was the average of the angular flux of all rays with centroids that intersected the sub-boundary. However, because only the centroids of each ray are considered using ray-spacing that is coarse compared to the sub-boundary size it not feasible.

An earlier work [41] used a similar 2-D sub-boundary averaging (though not directionally dependent); but rather than only considering the ray centroids, it considered the "projection" of rays. The "projection" being the area on the surface which would be intersected by the ray if it were

infinite in length. Then, partial intersections of the projection and sub-boundaries are considered. This allows for coarse ray-spacing to be used without as much accuracy on the interfaces as the previously mentioned method.

Figure 3.6 visually depicts the surface projections of 2-D rays on a single surface. This figure will be used as an example for the equations of this sub-boundary averaging method. ψ_s^1 should be a linear combination of the ray fluxes ψ_r^1 and ψ_r^2, based on their fractional areas, A_1^1 and A_2^1, respectively. Let us denote a sub-boundary as S_i where i is some index, and a ray projection as R_j where j is some index. We expect the surface flux to be a linear combination of the ray fluxes which intersect it; this can be expressed mathematically as

$$\psi_s^i = \sum_j \frac{A(S_i \cap R_j)}{A(S_i)} \psi_r^j, \tag{3.58}$$

where A denotes a function returning the area of the argument, and $\cap$ indicates the intersection of two objects. To show that this preserves the total neutron flux through the surface, consider the total flux through the surface

$$\begin{aligned} \psi_t &= \sum_i A(S_i)\psi_s^i \\ &= \sum_i A(S_i) \sum_j \frac{A(S_i \cap R_j)}{A(S_i)} \psi_r^j \\ &= \sum_i \sum_j A(S_i \cap R_j)\psi_r^j \\ &= \sum_j A(R_j)\psi_r^j, \end{aligned} \tag{3.59}$$

where this last line is simply the summation of all ray fluxes. The reverse problem, computing the ray fluxes from the sub-boundary fluxes, is found to be

$$\psi_r^j = \sum_i \frac{A(S_i \cap R_j)}{A(R_j)} \psi_s^i. \tag{3.60}$$

Figure 3.6 also highlights a problem with only considering the centroids of each ray. Ray 2 is split nearly evenly between sub-boundaries 1 and 2. If only the centroids was considered, all ray 2's flux would be put into sub-boundary 2 and in the reverse direction all it's flux would come from sub-boundary 2. If the flux is relatively uniform along the surface direction, this is fine; however, if there are discontinuities in the flux then this can lead to considerable inaccuracies.

Liu et al. [42] did introduce a very useful concept to sub-boundary averaging, with the direction-dependence in the number of sub-boundaries on each surface. Rather than using a fixed number of

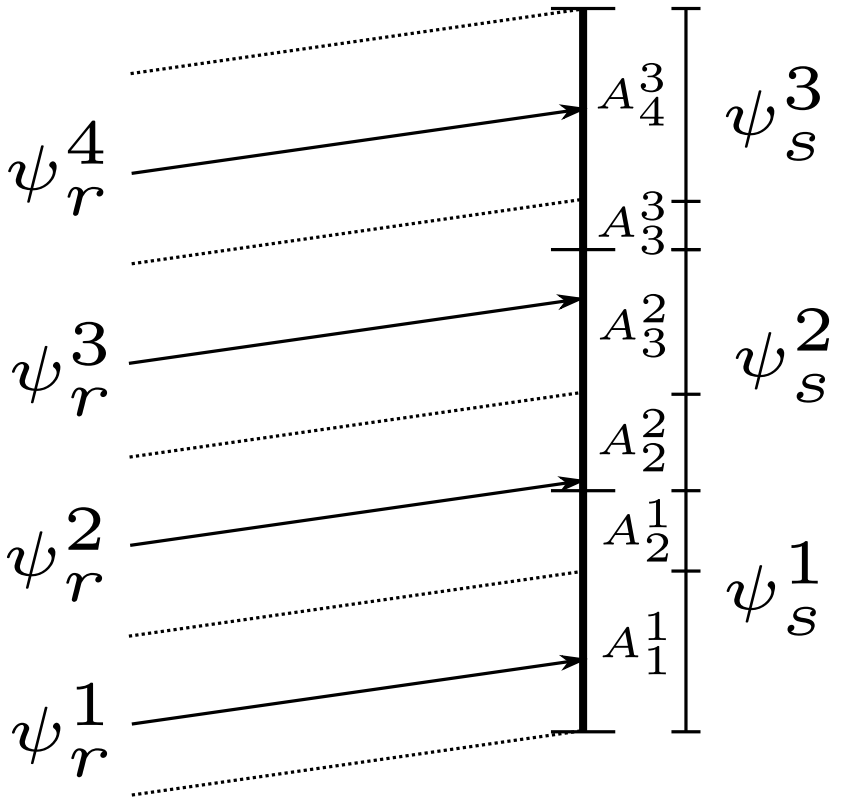

Figure 3.6: Example of sub-boundary surface flux for a single surface. Ray flux denoted with the r subscript, and surface flux denoted with s subscript. Ray projection areas are split by sub-boundaries in the line to the right of the impacted surface.

sub-boundaries on each surface, it is expected that directions which are closer to being perpendicular to the surface will have larger variation, and thus need more sub-boundaries. The number of sub-boundaries on each surface can be computed using the dimensions of the surface, and the direction. Similarly to MRT, the number of sub-boundaries on a surface is constrained to be an integer. The MRT equations, Eqs. (3.54), can be used to determine the number of sub-boundaries on the x and y surfaces.

3.4.4 Three-Dimensional Ray-Tracing Techniques

The MoC is naturally extended to three-dimensional calculations along characteristic tracks spanning three-dimensions. However, 3-D MoC presents significant computational challenges. This has led to significant research effort into developing more efficient approaches to three-dimensional MoC [32, 44–47]. One of the main focuses of this research has been in reducing the complexity

introduced by three-dimensional ray-tracing.

3.4.4.1 3-D Modular Ray-Tracing

In three-dimensional MoC calculations, characteristic rays must be laid down through the three-dimensional domain; Generally, three-dimensional tracks are generated by first creating a set to two-dimensional tracks, and generating three-dimensional tracks that project onto these two-dimensional tracks [32, 48]. The generation of these two-dimensional tracks can be simplified as viewing each of the two-dimensional tracks as a plane in the axial and characteristic directions, z and s respectively. Three-dimensional tracks are then produced by performing two-dimensional ray-tracing on this characteristic plane [32], as is shown in Fig. 3.7

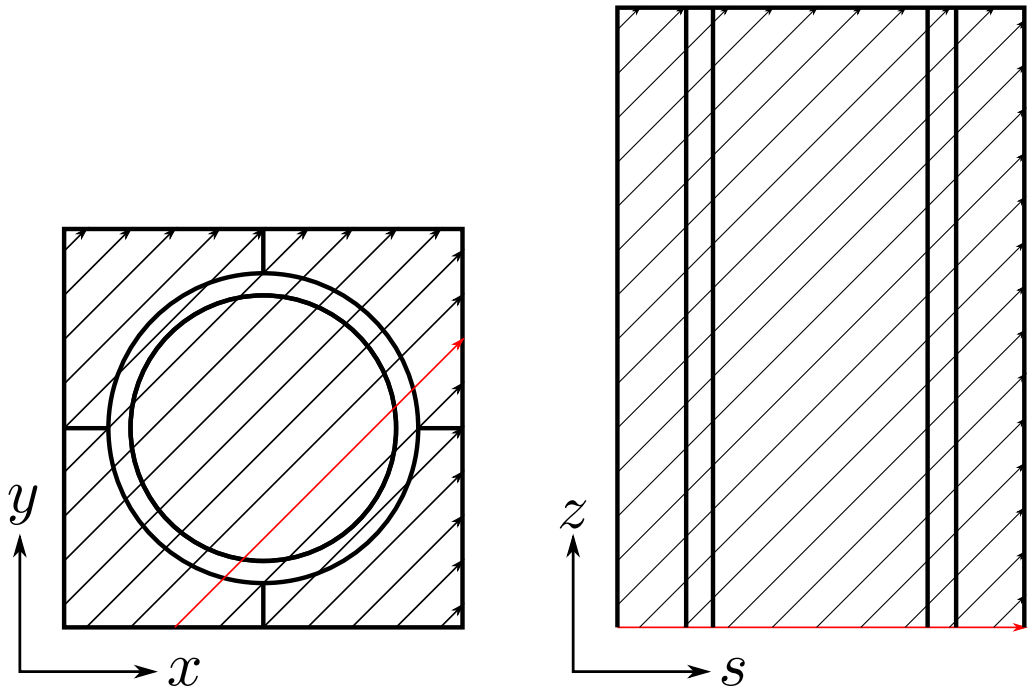

Figure 3.7: 3-D ray-tracing process. Generate 2-D tracks, these become characteristic planes. Along each plane, perform 2-D ray-tracing. The highlighted (red) characteristic track in the 2-D pin-cell on the left becomes the characteristic plane on the right.

There are subtleties in the generation of three-dimensional tracks, which have led to the development of different 3-D modular ray-tracing techniques [32, 48]. Previous work had reported that direct use of the MRT method in 3-D, required that tracks be stored separately for the forward and backward directions [32]; this has, however, been shown not to be the case [48]. The simplified MRT was developed to avoid this issue [32], but generates significantly more characteristic tracks [48].

As discussed in Section 3.4.1, 2-D MRT perturbs the azimuthal angles in the directional quadrature to ensure DNPL. For 3-D MRT, this also perturbs the polar angles in the directional quadrature. Kochunas [32] also found that modularization of the directional quadratures led to clustering of the discrete directions, which introduces significant error in the integration of spherical harmonics moments [32], and has implications on particle conservation in anisotropic calculations (Section 3.2.2). In order to avoid this issue, the axial ray-spacing can be reduced until the modularized polar angle is only perturbed within some error criteria [32]; however, this leads to significant increases in the number of tracks (and thus increases computational costs).

3.4.5 Transport Sweeping with the Method of Characteristics

The MoC is used to iteratively solve the transport equation, the iterations are generally referred to as *transport sweeps*. For given boundary conditions and source, a transport sweep is used to compute estimates of the scalar flux and other moments using equations in the form Eqs. (3.31) for FSMoC and Eqs. (3.46) for LSMoC. This is an overly generalized description of a transport sweep, and there are considerations that arise from the different ray-tracing techniques discussed.

In global ray-tracking procedures, calculations are most often carried out by examining a ray from end to end. The angular flux at the ends can be found from the boundary conditions. Along each segment, a transmission calculation can be carried out (Eqs. 3.26 and 3.43), and flux moments can be accumulated. This procedure is shared by the MRT which constructs global rays (long rays) by linking modular rays, as shown in Fig. 3.3. This allows for each ray calculation to be carried out in parallel, since each ray calculation is effectively independent [32]; though special considerations must be taken to avoid race-conditions in the accumulation of moments.

However, in the macroband method, transport sweeping is carried out in a different manner. It is not possible to generate a continuous characteristic track spanning the global domain when using MRMB techniques. Thus, transport calculations are carried out in a pin-by-pin (assuming pins are the subsystems on which track data is generated) basis. For each pin calculation, boundary or interface angular flux can be computed as described in Section 3.4.3.1, and transmission/accumulation calculations are carried out by sweeping over the tracks. This can be done by considering each track separately, or by considering each macroband which are guaranteed to pass through the same regions. The angular flux on the exiting interface must be approximated, this can be done as described in Section 3.4.3.1.

Pin-by-pin transport calculations must be carried out in a specific order, by considering the dependencies of angular flux. Figure 3.8 displays the sweeping order for a 2×2 array of pins in 2-D; this order is significantly different than the ray-by-ray order used in traditional MRT-based MoC calculations. Sweeping in this manner limits parallelism, though it may be possible to construct a

dependency graph to get an optimal sweeping order considering macrorays individually, rather than on the pin-by-pin basis.

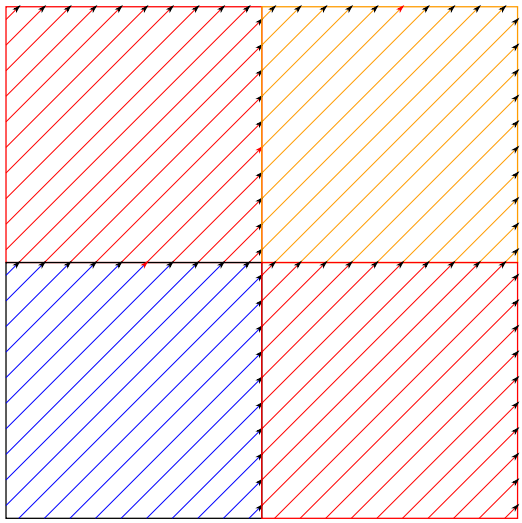

Figure 3.8: Pin-by-pin sweeping order for a 2×2 domain with colors representing the order starting from the bottom left pin.

3.5 Parallelism

High-fidelity transport methods, such as the MoC, can require significant computational resources for full core calculations; this is particularly true for 3-D calculations. While processing power has increased exponentially since the MoC was first conceived in 1972 [1], since the early 2000's, single-core processing power has largely leveled off. System architectures, as well as code design, have become more focused on *parallel* computations. Previous works [32] made significant progress in the efficient parallelization of the MoC.

Kochunas [32] developed a hybrid-parallel algorithm for the MoC that included thread-based parallelism over characteristic tracks, as well as spatial and angular decomposition. This work showed that the MoC was able to scale well up to 10000's of processors. While this work is important, and has led to significant advancement, the use of 1000's of processors is not feasible for industrial use. It is thus the author's opinion that the primary focus of research on 3-D MoC techniques should be on serial efficiency, such as the linear-source approximation (LSA) (Chapter 5), and macroray (Chapter 6); however, moderate levels of parallelism are feasible for industry, and so more efficient use of parallel resources should also be a focus of research (Chapter 4).

In MoC calculations, each characteristic track calculation is nearly independent from others; previous works have indicated that loops over characteristic tracks can be parallelized efficiently by

using threads on traditional central processing units (CPUs) [32] or on general purpose graphics processing units (GPGPUs) [10]. This type of parallelism is called *shared-data parallelism*, as data is shared between the parallel threads.

Large neutronics calculations may require significant amounts of memory, and thus *distributed-data parallelism* is necessary. In general, this type of parallelism separates (partitions) a domain of the problem, and separate computing nodes are assigned a subdomain. Only data for the assigned subdomain is stored, and thus whole-core simulations become possible; additionally, because each subdomain can be processed in parallel, overall runtimes typically decrease with increasing numbers of subdomains (processors).

MPACT has the capabilities for domain decomposition/parallelism over two separate domains: space and direction. In MPACT, each discrete direction has an easily calculable amount of work, and the decomposition is trivial; in general the same cannot be said of the spatial domain. As part of this thesis work, a more efficient method of spatial decomposition has been investigated and developed in MPACT [49]. Details on the spatial decomposition techniques used in this work are given in Chapter 4.

Bibliography

[1] J.R. Askew. *A Characteristics Formulation of the Neutron Transport Equation in Complicated Geometries*. 1972.

[2] M.J. Halsall. "CACTUS, a characteristics solution to the neutron transport equations in complicated geometries". In: *Transactions of the American Nuclear Society*. 1980. URL: https://inis.iaea.org/search/search.aspx?orig{_}q=RN:12592444.

[3] Benjamin Collins et al. "Stability and accuracy of 3D neutron transport simulations using the 2D/1D method in MPACT". In: *Journal of Computational Physics* 326 (2016), pp. 612–628. ISSN: 10902716. DOI: 10.1016/j.jcp.2016.08.022.

[4] Dave Knott and Akio Yamamoto. "Lattice Physics Computations". In: *Handbook of Nuclear Engineering* (2010), pp. 913–1239. DOI: 10.1007/978-0-387-98149-9_9.

[5] Ser Gi Hong and Nam Zin Cho. "CRX: A code for Rectangular and Hexagonal Lattices Based on the Method of Characteristics". In: *Annals of Nuclear Energy* 25.97 (1998), pp. 547–565.

[6] Shinya Kosaka and Etsuro Saji. "Transport theory calculation for a heterogeneous multi-assembly problem by characteristics method with direct neutron path linking technique". In: *Journal of Nuclear Science and Technology* 37.12 (2000), pp. 1015–1023. ISSN: 00223131. DOI: 10.1080/18811248.2000.9714987.

[7] K.S. Smith and J.D. Rhodes III. "Full-Core, 2-D, LWR Core Calculations with CASMO-4E". In: *Physor* 1 (2002), pp. 1–13.

[8] Naoki Sugimura et al. "Neutron Transport Models of AEGIS: An Advanced Next-Generation Neutronics Design System". In: *Nuclear Science and Engineering* 155.2 (2006), pp. 276–289. ISSN: 0029-5639. DOI: 10.13182/nse155-276.

[9] Emiliano Masiello, Richard Sanchez, and Igor Zmijarevic. "New Numerical Solution with the Method of Short Characteristics for 2-D Heterogeneous Cartesian Cells in the APOLLO2 Code: Numerical Analysis and Tests". In: *Nuclear Science and Engineering* 161.3 (2008), pp. 257–278. ISSN: 0029-5639. DOI: 10.13182/nse161-257.

[10] William Boyd et al. “The OpenMOC method of characteristics neutral particle transport code”. In: *Annals of Nuclear Energy* 68 (2014), pp. 43–52. ISSN: 03064549. DOI: 10.1016/j.anucene.2013.12.012.

[11] R. Le Tellier and A. Hébert. “Anisotropy and Particle Conservation for Trajectory-Based Deterministic Methods”. In: *Nuclear Science and Engineering* 158.1 (2008), pp. 28–39. ISSN: 0029-5639. DOI: 10.13182/NSE08-A2736.

[12] Rodolfo M. Ferrer and Joel D. Rhodes. “The linear source approximation and particle conservation in the Method of Characteristics for isotropic and anisotropic sources”. In: *Annals of Nuclear Energy* 115 (2018), pp. 209–219. ISSN: 03064549. DOI: 10.1016/j.anucene.2018.01.023.

[13] Akio YAMAMOTO, Yasunori KITAMURA, and Yoshihiro YAMANE. “Simplified Treatments of Anisotropic Scattering in LWR Core Calculations”. In: *Journal of Nuclear Science and Technology* 45.3 (2008), pp. 217–229. ISSN: 0022-3131. DOI: 10.1080/18811248.2008.9711430.

[14] Petko Petkov, Toshikazu Takeda, and Takamasa Mori. “Comparison of the Flat and Linear Source Variants of the Method of Characteristics”. In: *Annals of Nuclear Energy* 26.10 (1999), pp. 935–942. ISSN: 03064549. DOI: 10.1016/S0306-4549(98)00109-1.

[15] Rodolfo M. Ferrer and Joel D. Rhodes. “A Linear Source Approximation Scheme for the Method of Characteristics”. In: *Nuclear Science and Engineering* 182.2 (2016), pp. 151–165. ISSN: 0029-5639. DOI: 10.13182/NSE15-6.

[16] Edward W. Larsen and Warren F. Miller. “Convergence Rates of Spatial Difference Equations for the Discrete-Ordinates Neutron Transport Equations in Slab Geometry”. In: *Nuclear Science and Engineering* 73.1 (1980), pp. 76–83. ISSN: 0029-5639. DOI: 10.13182/nse80-3.

[17] M. J. Halsall. “Neutron Transport in WIMS by the Characteristics Methods”. In: *Transactions of the American Nuclear Society1*. 1993, pp. 454–455.

[18] Chuntao Tang and Shaohong Zhang. “Development and verification of an MOC code employing assembly modular ray tracing and efficient acceleration techniques”. In: *Annals of Nuclear Energy* 36.8 (2009), pp. 1013–1020. ISSN: 03064549. DOI: 10.1016/j.anucene.2009.06.007.

[19] Petko T. Petkov and Toshikazu Takeda. “Transport calculations of MOX and UO2 pin cells by the method of characteristics”. In: *Journal of Nuclear Science and Technology* 35.12 (1998), pp. 874–885. ISSN: 00223131. DOI: 10.1080/18811248.1998.9733960.

[20] C Rabiti et al. “Quasi Linear Representation of the Isotropic Scattering Source for the Method of Characteristics”. In: *International Conference on Mathematics, Computational Methods & Reactor Physics* January (2009), pp. 3–7.

[21] S Santandrea and R Sanchez. “POSITIVE LINEAR AND NONLINEAR SURFACE CHARACTERISTIC SCHEMES FOR THE NEUTRON TRANSPORT EQUATION IN UNSTRUCTURED GEOMETRIES”. In: *Physor*. 2002.

[22] Simone Santandrea, Richard Sanchez, and Pietro Mosca. “A linear surface characteristics approximation for neutron transport in unstructured meshes”. In: *Nuclear Science and Engineering* 160.1 (2008), pp. 23–40. ISSN: 00295639. DOI: 10.13182/NSE07-69.

[23] Romain Le Tellier and Alain Hébert. “On the integration scheme along a trajectory for the characteristics method”. In: *Annals of Nuclear Energy* 33.14-15 (2006), pp. 1260–1269. ISSN: 03064549. DOI: 10.1016/j.anucene.2006.07.010.

[24] Alain Hébert. “High-Order Linear Discontinuous and Diamond Differencing Schemes Along Cyclic Characteristics”. In: *Nuclear Science and Engineering* 184.4 (2016), pp. 591–603. ISSN: 0029-5639. DOI: 10.13182/nse16-82.

[25] Alain Hébert. “Acceleration of step and linear discontinuous schemes for the method of characteristics in DRAGON5”. In: *Nuclear Engineering and Technology* 49.6 (2017), pp. 1135–1142. ISSN: 2234358X. DOI: 10.1016/j.net.2017.07.004.

[26] Emiliano Masiello, Roberto Clemente, and Simone Santandrea. “High-Order Method of Characteristics for 2-D Unstructured Meshes”. In: *International Conference on Mathematics, Computational Methods & Reactor Physics* June 2015 (2009). URL: http://mathematicsandcomputation.cowhosting.net/MC09/pdfs/202865.pdf{\%}5Cnpapers3://publication/uuid/217E92CC-587D-4349-843B-58B5693D625C.

[27] X. M. Chai, K. Wang, and D Yao. “The linear source approximation in three dimension characteristics method”. In: *International Conference on Mathematics, Computational Methods \& Reactor Physics (M\&C 2009)* February (2009), pp. 1–14.

[28] Y. I. Chang. “Technical rationale for metal fuel in fast reactors”. In: *Nuclear Engineering and Technology* 39.3 (2007), pp. 161–170. ISSN: 1738-5733. URL: http://gehitachiprism.com/wp-content/themes/geh{_}prism/resources/Technical{_}Rationale{_}for{_}Metal{_}Fuel{_}in{_}Fast{_}Reactors.pdf.

[29] Andrew Fitzgerald and Brendan Kochunas. “Fast Exponential Function Approximations for the Method of Characteristics with Linear Source”. In: *Transactions of the American Nuclear Society*. Orlando, USA, 2018, pp. 645–648.

[30] W. L. Filippone, S. Woolf, and R. J. Lavigne. “Particle Transport Calculations with the Method of Streaming Rays”. In: *Nuclear Science and Engineering* 77.2 (1980), pp. 119–136. ISSN: 0029-5639. DOI: 10.13182/nse81-a21346.

[31] G. J. Wu and R. Roy. “A new characteristics algorithm for 3D transport calculations”. In: *Annals of Nuclear Energy* 30.1 (2003), pp. 1–16. ISSN: 03064549. DOI: 10.1016/S0306-4549(02)00046-4.

[32] Brendan Matthew Kochunas. “A Hybrid Parallel Algorithm for the 3-D Method of Characteristics Solution of the Boltzmann Transport Equation on High Performance Compute Clusters”. Doctoral. University of Michigan, 2013, pp. 1–194.

[33] Yeon Sang Jung and Han Gyu Joo. “Decoupled Planar MOC Solution for Dynamic Group Constant Generation in Direct Three-Dimensional Core”. In: *M&C 2009* (2009).

[34] Han Gyu Joo et al. “Methods and performance of a three-dimensional whole-core transport code DeCART”. In: *PHYSOR 2004*. 2004, pp. 21–34. ISBN: 0894486837. URL: http://www.scopus.com/inward/record.url?eid=2-s2.0-22344449157{\&}partnerID=tZOtx3y1.

[35] Franck Gabriel et al. “APOLLO3: CEA/DEN DETERMINISTIC MULTI-PURPOSE CODE FOR REACTOR PHYSICS ANALYSIS”. In: May 2016. 2016.

[36] MPACT Team. *MPACT Theory Manual v2.2.0*. Tech. rep. Consortium for Advanced Simulation of Light Water Reactors, 2016.

[37] Alain Hébert. “Acceleration of Step and Linear Discontinuous Schemes for the Method of Characteristics in DRAGON5”. In: *M&C 2017*. Jeju, Korea, 2017.

[38] Eduardo A. Villarino et al. “HELIOS: Angularly Dependent Collision Probabilities”. In: *Nuclear Science and Engineering* 112.1 (1992), pp. 16–31. ISSN: 0029-5639. DOI: 10.13182/NSE112-16.

[39] Akio Yamamoto. “Reduction in spatial discretization error in the method of characteristics by using the mobile-chord ray tracing method”. In: *Annals of Nuclear Energy* 35.5 (2008), pp. 783–789. ISSN: 03064549. DOI: 10.1016/j.anucene.2007.09.018.

[40] Akio Yamamoto et al. “Non-Equidistant Ray Tracing for the Method of Characteristics”. In: *M&C 2005* (2005), pp. 1–10.

[41] Ser Gi Hong and Nam Zin Cho. "Method of Characteristic Direction Probabilities for Heterogeneous Lattice Calculation". In: *Nuclear Science and Engineering* 132.1 (2017), pp. 65–77. ISSN: 0029-5639. DOI: 10.13182/nse99-a2049.

[42] Zhouyu Liu et al. "Theory and analysis of accuracy for the method of characteristics direction probabilities with boundary averaging". In: *Annals of Nuclear Energy* 77 (2015), pp. 212–222. ISSN: 0306-4549. DOI: 10.1016/J.ANUCENE.2014.11.016.

[43] François Févotte, Simone Santandrea, and Richard Sanchez. "Advanced Transverse Integration for the Method of Characteristics". In: *M&C 2007*. 2007, pp. 1–12. ISBN: 0894480596.

[44] John R. Tramm et al. "A task-based parallelism and vectorized approach to 3D Method of Characteristics (MOC) reactor simulation for high performance computing architectures". In: *Computer Physics Communications* 202 (2016), pp. 141–150. ISSN: 00104655. DOI: 10.1016/j.cpc.2016.01.007.

[45] Akio Yamamoto et al. "GENESIS: A Three-Dimensional Heterogeneous Transport Solver Based on the Legendre Polynomial Expansion of Angular Flux Method". In: *Nuclear Science and Engineering* 49.6 (2017), pp. 1143–1156. ISSN: 2234358X. DOI: 10.1016/j.net.2017.06.016.

[46] Laurent Graziano et al. "Polynomial Characteristics Method for Neutron Transport in 3D extruded geometries". In: *M&C 2017*. Jeju, Korea, 2017.

[47] Geoffrey Gunow et al. "Accuracy and Performance of 3D MOC for Full-Core PWR Problems". In: *M&C 2017*. Jeju, Korea, 2017.

[48] S. Shaner et al. "Theoretical analysis of track generation in 3D method of characteristics". In: *Mathematics and Computations, Supercomputing in Nuclear Applications and Monte Carlo International Conference, M&C+SNA+MC 2015* 4.Mc (2015), pp. 2667–2681.

[49] Andrew P Fitzgerald et al. "Spatial decomposition of structured grids for nuclear reactor simulations". In: *Annals of Nuclear Energy* 132 (2019), pp. 686–701. ISSN: 0306-4549. DOI: 10.1016/j.anucene.2019.06.054.

CHAPTER 4

Spatial Decomposition

4.1 Introduction

Until relatively recently, the method of choice for neutronics calculations has been neutron diffusion. Neutron diffusion codes can perform whole-core calculations, on a typical workstation, in relatively short run-times. However, with the recent shift towards higher fidelity methods such as S_N, and MoC [1], more significant computational resources are necessary. These high fidelity methods allow for more detailed analysis, through finer resolution and use of fewer approximations, but typically take far more time to perform calculations; particularly for large calculations. Although processor clock-speeds have significantly improved, in the past several years computer cores have, for the most part, not gotten faster. To reduce the run-times (real-time) of high fidelity simulations, it is thus necessary to rely on parallelism.

There are many different aspects of parallelism, and thread-based parallelism has been discussed previously Section 3.5. Shared-data parallelism (threads), is limited to the resources of a single computational node. In order to utilize more resources, it is necessary to use a technique called *domain decomposition*. Even without considerations for run-times, these high-fidelity simulations typically use more memory than is available on a single node, and domain decomposition becomes a necessity. In general, domain decomposition involves splitting up one domain of the problem into smaller subdomains; some typical domains to decompose are space, direction, and energy. Each smaller subdomain is assigned to a separate processor, and these can be run in parallel; although, there is generally some communication between the processors.

In Monte-Carlo simulations, it is common that spatial decomposition involves duplication of some spatial locations. However, in deterministic transport methods, each domain is typically *partitioned*, that is the domain is split without any overlap between subdomains. The MPACT [2] code has the ability to decompose two domains: space and direction. In MPACT, each discrete direction has a calculable amount of work, and the decomposition is trivial; in general, the same cannot be said of the spatial domain. This chapter focuses on improvements to the spatial decomposition

techniques used in MPACT; these techniques, however, can be applied to other transport codes and similar results would be expected. The contents of this chapter are, in large part, adapted from an article published on this work [3].

As diffusion has been the method of choice for so long in the reactor physics field, spatial partitioning techniques common in other fields have, largely, not been applied. Transport codes such as MPACT [2], or OpenMOC [4] used simple spatial partitioning methods that divided the core into uniformly sized blocks. However, the spatial partitioning of a reactor can be abstracted to a graph partitioning problem [5], which has been well studied in computer science [6] and applied to other simulation fields such as computational fluid dynamics [7]. In general, the graph partitioning problem is *NP-complete*, meaning that a partitioning cannot be easily verified as optimal; therefore, graph partitioning relies on approximate heuristic methods. Many different methods have been developed for graph partitioning, several of which are discussed in Section 4.3.

The remained of this chapter is structured as follows. In Section 4.2, a description of spatial decomposition in MPACT is given. Section 4.3 introduces relevant graph theory concepts, and the methods used for spatial partitioning in this work. Section 4.4 describes the applications of these graph theory methods in MPACT. Section 4.5 compares methods for 2-D and 3-D reactor simulations. Finally, Section 4.7 lists the conclusions that are drawn from this work.

4.2 Spatial Decomposition in MPACT

The MPACT code uses the MoC for neutronics calculations, and was originally developed for direct whole-core simulation of LWRs. As mentioned in Section 3.4.1, MPACT uses the modular ray-tracing [8] to significantly reduce track memory usage. The ray-tracing modules are small geometries that are often repeated in the reactor; these ray-tracing modules are used as the smallest unit for spatial decomposition in MPACT [9]. These ray-tracing modules are typically an axial slice of a quarter of a full fuel assembly, as shown in Fig. 4.1 The core consists of a structured grid of these modules in which each module has the same dimensions but may have different numbers of computational cells. Therefore, in MPACT, the spatial decomposition is a structured grid partitioning problem.

In general, it is possible to use the computational cells as the smallest unit in the decomposition. However, this causes the decomposition problem to become an unstructured mesh partitioning problem. This has not been done in MPACT because communication would become significantly more complicated. Additionally, there would be more re-entrant rays which would have negative impacts on the rate of convergence.

MPACT has had two spatial decomposition methods in the past: manual decomposition, and assembly-based decomposition. A user may manually enter a decomposition [9], but it is time

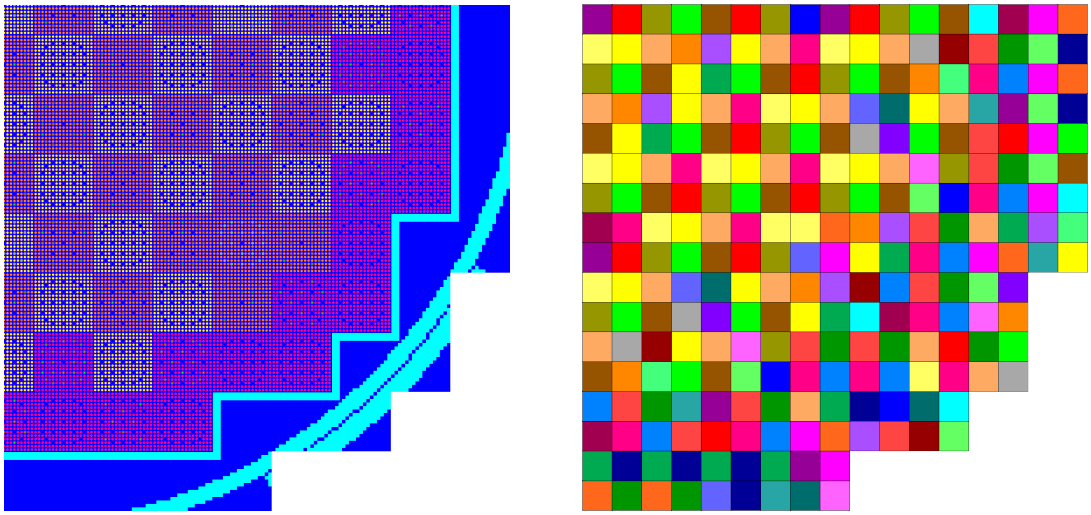

(a) fine mesh (b) ray-tracing module mesh

Figure 4.1: Example quarter core configuration and corresponding ray-tracing modular mesh in MPACT.

consuming to construct a balanced decomposition and will likely still be suboptimal to some degree. An automated method exists that recursively bisects the core using Morton-ordering [10] applied to the reactor assembly geometries. While this method is automated, it often yields very imbalanced domains, and also restricts the number of subdomains that can be used.

Previous work has shown that spatial decomposition of reactors can be abstracted to a graph partitioning problem [5]. The use of graph partitioning methods in MPACT is expected to solve the issues encountered in each of the two approaches described above. These methods can be used to decompose into an arbitrary number of domains with high quality results, without user input.

Existing graph partitioning libraries such as METIS [11] partition graphs very efficiently and have very high quality results. To use all given processors, MPACT requires that each spatial subdomain contains at least one module, i.e. no partition can be empty. However, in some cases, particularly when the number of partitions is high, METIS may generate empty partitions. This means METIS cannot be used to decompose the core into an arbitrary number of subdomains without modifying the resulting partitions. For this reason, MPACT does not rely on third-party libraries for graph partitioning in the spatial decomposition process.

4.3 Applied Graph Theory

The spatial decomposition of a reactor core can be abstracted to the partitioning of a graph. Specifically, this would be a weighted graph, $G(V, E)$, which is comprised of a set of vertices, V, and a set of edges, E, that connect pairs of vertices. In general, these vertices and edges may have

weights; a vertex v_i will have weight w_i, and an edge e_i between vertices v_i and v_j will have weight c_{ij}. In MPACT, a vertex represents a ray-tracing module, and the edges represent communication between adjacent modules in the MoC. The graphs are undirected because communication between ray-tracing modules is two-way.

Previous work [5] applied unweighted graph partitioning techniques to the reactor spatial decomposition problem; the work presented here applies generalizations and improvements to the methods used for graphs with weighted vertices and edges. A vertex's weight indicates the amount of computational work that is needed; as one might expect, this is highly correlated with the number of computational cells. This is shown in Section 4.5. In general, the edges may also be weighted to account for different amounts of data transfer. This is discussed in more detail in Section 4.4.

The goal is for each partition to have equal weight, with minimal weight of edges cut by partition boundaries. This is equivalent to each subdomain having the same amount of computational work with minimized communication between processes. If each process has roughly the same amount of work to perform, then less time will be spent waiting for other processes, thus improving parallel efficiency. Also, with less communication, less time will be spent passing data between processes, so the parallel overhead will be reduced.

In this work, methods were separated into two distinct categories: partitioning methods and partition refinement (improvement) methods. Partitioning methods give a near-balanced partitioning for a given graph. Refinement methods attempt to reduce communication between existing partitions in a graph. As applied in MPACT, these refinement methods typically did not significantly reduce communication. These methods and results are presented in Section 4.6.

4.3.1 Graph Partitioning Methods

In this work, recursive partition methods were considered due to their capability to partition into arbitrary numbers of domains. Each of these recursive partitioning methods sorts the graph, using different methods, and then divides or "cuts" the graph into two sub-graphs with approximately equal vertex weights. Once a graph's vertices are sorted into a list, V_s, the graph can be bisected using Algorithm 3.

Multi-level partitioning methods are widely used in other fields such as networking, where graphs can become very large; however, in MPACT, the number of ray-tracing modules is on the order of a few hundred to several thousand, which directly correlates to the size of the graph. Additionally, for MPACT, the decomposition problem is static, so the computation time for partitioning is expected to be negligible as it can simply be performed one time at the outset. Due to the small graph size, multi-level methods were not considered as part of this work.

Algorithm 3 The algorithm used to determine how to cut a graph, $G(V, E)$, into two sub-graphs based on a sorted vertex list V_s, and that the graph will be recursively partitioned into N groups.

procedure GRAPH CUT($G(V, E), V_s, N$)
  $N_1 \leftarrow \lfloor N/2 \rfloor$ ▷ Desired number of recursive partitions for first subgraph
  $W_1 \leftarrow \frac{N_1}{N} \sum_{v_i \in V} w_i$ ▷ Ideal weight of first subgraph
  Let V_1 be a set of vertices such that:
    - $V_1 \subset V$
    - The vertices V_1 are taken in order from V_s
    - $W_1 - \sum_{v_i \in V_1} w_i$ is minimized
  Let V_2 be the subset $V \setminus V_1$
  Optionally call a refinement method
  Create a graph G_1 from V_1
  Create a graph G_2 from V_2
end procedure

4.3.1.1 Recursive Spectral Bisection

The recursive spectral bisection (RSB) method, originally developed by Pothen et al. [12], has been highly successful and widely used in graph partitioning [13, 14]. This method relies entirely on the connectivity of the graph and not on its geometry. The RSB method has been improved to allow to allow for partitioning of *weighted* graphs into any number of domains [15].

The RSB method makes use of the Laplacian matrix of a graph; specifically the second-smallest eigenvalue of this matrix, referred to by Fiedler as the *algebraic connectivity* [16]. The eigenvector associated with this eigenvalue has also been known as the *Fiedler vector*. For weighted graphs, the weighted Laplacian matrix is used in lieu of the Laplacian matrix; matrix elements are given by

$$L_{ij} = \begin{cases} d_i, & i = j, \\ c_{ij}, & i \neq j, \\ 0, & \text{else}, \end{cases} \tag{4.1}$$

where d_i is the sum of edge weights from vertex v_i, and c_{ij} is the weight of the edge between vertices v_i and v_j. The Fiedler vector is found from this weighted Laplacian matrix; by sorting the values of the Fiedler vector, the vertices can be reordered in a one-dimensional list V_s. This list of vertices is then divided into two sets, based on weight and total number of partitions needed (see Algorithm 3). The recursive spectral bisection algorithm is listed in Algorithm 4.

Algorithm 4 The recursive spectral bisection (RSB) algorithm.

procedure RSB($G(V, E)$)
    Let L be the weighted Laplacian of $G(V, E)$
    Compute eigenvectors of L
    Use the Fiedler vector to sort $V \rightarrow V_s$ ▷ If tie, use larger eigenvectors
    Cut graph into $G_1(V_1, E_1), G_2(V_2, E_2)$: Algorithm 3
    RSB($G_1(V_1, E_1)$)
    RSB($G_2(V_2, E_2)$)
end procedure

4.3.1.2 Recursive Inertial Bisection

Another class of recursive partitioning methods are coordinate or geometric methods. There are many different geometric partitioning methods in existence; in this study, the recursive intertial bisection (RIB) method [6, 17] was investigated. This method uses only the geometry of the graph to construct a bisector and does not consider the connectivity (edges) in any way.

The RIB method determines a bisector which cuts the graph into two approximately equally sized subdomains. This is easily generalized for weighted graphs. The bisector should have approximately equal amounts of weight on each side. The RIB makes no assumption of the orientation of the graph in space, unlike some other coordinate partitioning methods. The principle axes of the graph are equivalent to the eigenvectors of the inertial matrix given by

$$\boldsymbol{I} \equiv \sum_{i=1}^{n} w_i \left(\boldsymbol{x}_i - \overline{\boldsymbol{x}}\right)^T \left(\boldsymbol{x}_i - \overline{\boldsymbol{x}}\right), \tag{4.2}$$

where n is the number of vertices, $\boldsymbol{x}_i$ is a row-vector containing coordinates of vertex v_i, and $\overline{\boldsymbol{x}}$ is the mean coordinate vector given by

$$\overline{\boldsymbol{x}} \equiv \frac{\sum_{i=1}^{n} w_i \boldsymbol{x_i}}{\sum_{i=1}^{n} w_i}. \tag{4.3}$$

An approximate bisector is given as passing through the weighted centroid with normal vector given as one of the eigenvectors of $\boldsymbol{I}$.

Other works [6, 17] have used the smallest eigenvalue's eigenvector as a normal vector to minimize the mean-square distance of vertices from the bisecting line or plane. However, in this work, the largest eigenvalue's eigenvector is used, so a smaller cut-size is typically given while still bisecting the graph into two subdomains of approximately equal weight. This is the case because in the MoC, communication scales with the surface area between adjacent ray-tracing modules. This may not be the case for other computational methods.

In general, a line or plane passing through the weighted centroid with the eigenvector normals will not cut the graph into two equally weighted subdomains. Instead, the vertices will be sorted according to their distance from the approximate bisectors, and then a cut will be made so that near equal amounts of weight are in each set using Algorithm 3. This sorting and cutting based on weights is equivalent to shifting the bisector in the direction of the normal vector. An example is visualized in Fig. 4.2. The RIB algorithm is listed in Algorithm 5.

Algorithm 5 The basic recursive intertial bisection (RIB) algorithm.

procedure RIB($G(V, E)$)
    Compute the weighted centroid of the graph $\overline{\boldsymbol{x}}$, given by Eq. (4.3)
    Shift coordinates relative to centroid: $\boldsymbol{x}_i^c = \boldsymbol{x}_i - \overline{\boldsymbol{x}} \quad \forall i \in V$
    Compute inertial matrix $\boldsymbol{I}$, given by Eq. (4.2)
    Compute eigenvectors of $\boldsymbol{I}$. Largest eigenvalue's eigenvector $\boldsymbol{e}_1$
    Compute distance from largest eigen-pair bisector: $d_i = \boldsymbol{x}_i^c \cdot \boldsymbol{e}_1$
    Sort $V \rightarrow V_s$ based on d_i. ▷ In ties use smaller eigenvalue's eigenvector
    Cut graph into $G_1(V_1, E_1), G_2(V_2, E_2)$: Algorithm 3
    RIB($G_1(V_1, E_1)$)
    RIB($G_2(V_2, E_2)$)
end procedure

4.3.1.3 Recursive Expansion-Based Methods

The recursive expansion bisection (REB) methods comprise the last class of partitioning methods examined in this work. These methods begin a bisection step by selecting a vertex as the starting point of a subdomain. This subdomain is then expanded until it is approximately half the size of the graph [5, 6, 18, 19]. In this work, the method outlined by Fitzgerald et al. [5] was slightly modified and generalized to weighted graphs. For the remainder of this work, the acronym *REB* will be used to denote this specific expansion-based method rather than the entire class of methods.

This REB method considers both the geometry and connectivity of the graph. The method begins by choosing a starting vertex for the subdomain and then expands based on a set of prioritized rules. At each expansion step, the next vertex is chosen so that it is geometrically close to the vertices within the subdomain and to minimize edges between the subdomain and the remaining graph. However, this method makes the assumptions that the mesh is structured, and that every mesh element is the same shape and size. For the application in MPACT, this is always true.

This REB method uses the concept of a *sphere of influence (SOI)* around a vertex. The SOI includes directly neighboring vertices and vertices that neighbor more than one of the direct neighbors or that would if the direct neighbor were present in each structured position around the primary vertex. This is shown for 2-D rectangular structured mesh in Fig. 4.3. For implementation

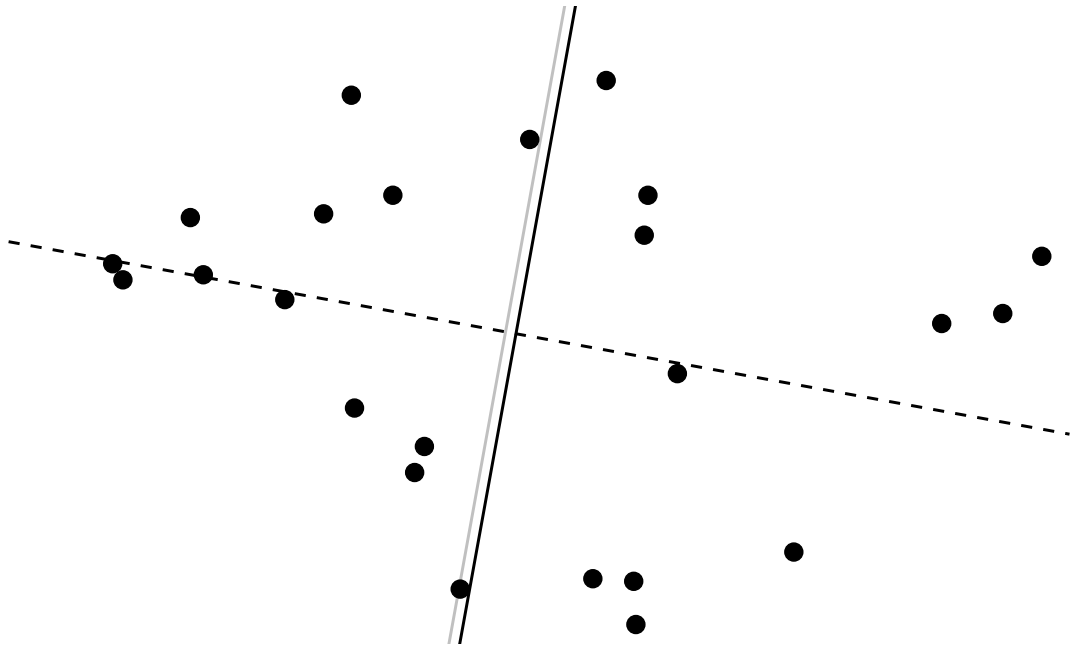

Figure 4.2: Example of an inertial bisection. Vertices are shown as black points, the bisectors of the largest eigen-pair is shown by the black solid, and the bisector of the smallest eigen-pair is shown by the black dashed line. The "shifted" bisector used in the partitioning is shown in grey. While the communication between vertices is not drawn, it is clear that the length (proportional to cut size) of the smallest eigen-pair bisector is larger than that of the largest eigen-pair bisector.

simplicity, the sphere of influence is calculated using distance rather than connectivity.

The starting vertex in this REB method is chosen using a set of prioritized rules:

1. must be on graph boundary, i.e. at least one direct neighbor is not present,
2. must have the lowest summed weight of edges, and
3. must be located furthest from weighted centroid (given by Eq. (4.3)).

Vertices within the expanding subdomain are considered internal vertices, and the remaining vertices are considered to be external vertices. During expansion, the next vertex is determined using a set of prioritized rules:

1. must be neighboring at least one internal vertex,
2. must have the highest summed weight of edges with internal vertices,
3. must have the lowest summed weight of edges with external vertices,
4. must have the largest number of internal SOI vertices,
5. must have the largest number of external SOI vertices, and

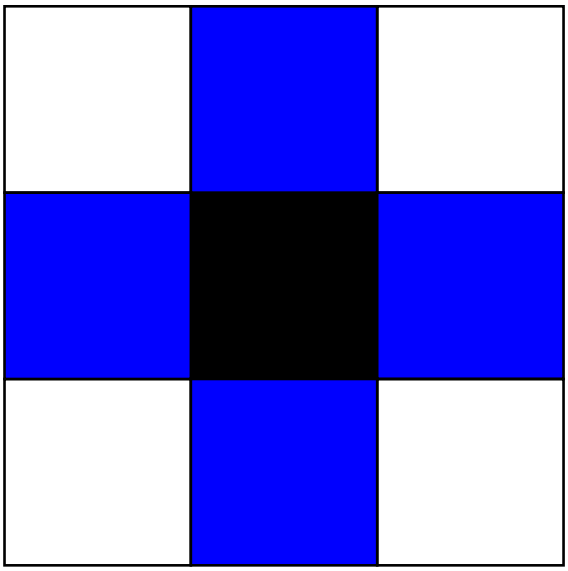

Figure 4.3: "Sphere of influence" example for 2-D rectangular structured grid. The primary vertex is shown in black, direct neighbors are blue, and additional vertices in the sphere are white [5].

6. must have the smallest distance from reference vertex.

The reference vertex is in the expanding subdomain, which begins as the first vertex but changes during expansion; the reference vertex is the most recently added vertex with less external communication than the previously added vertex. An example of the expansion order is shown in Fig. 4.4.

Algorithm 6 The chosen Recursive Expansion Bisection (REB) algorithm.

1: **procedure** REB($G(V, E)$)
2: Compute weighted centroid of the graph
3: Choose a starting vertex for the expanding domain: See rules in Section 4.3.1.3
4: Expand the domain from the starting vertex. Let V_s be the list of vertices in order of the expansion: See rules in Section 4.3.1.3
5: Cut graph into $G_1(V_1, E_1), G_2(V_2, E_2)$: Algorithm 3
6: REB($G_1(V_1, E_1)$)
7: REB($G_2(V_2, E_2)$)
8: **end procedure**

4.4 Applications for MPACT

As described in Section 4.2, MPACT's spatial decomposition is performed on the ray-tracing module mesh. However, there are a couple of restrictions on spatial subdomains in MPACT. Each spatial

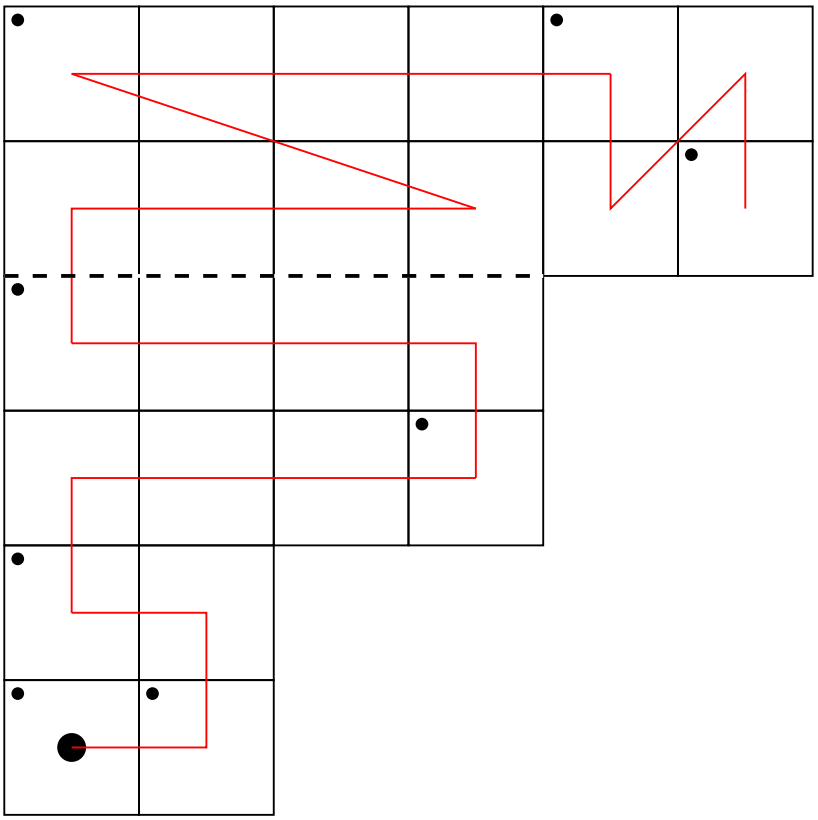

Figure 4.4: An example of the REB method expansion on a small graph. The black lines show the square mesh cells. The expansion begins at the large black point in the center of a cell, and the red line from this shows the expansion's order. Each small black dot in the upper left of a cell indicates the reference vertices during expansion. The thick black dashed line shows the bisecting cut.

subdomain must be contiguous, and cannot wrap around other spatial subdomains. To account for these restrictions, adaptations are made to the graph partitioning process.

Due to restrictions in MPACT, at each recursive step, each subdomain in a bisection is made contiguous. If a partitioning method results in a noncontiguous subdomain, then each noncontiguous group of modules will be moved into the other subdomain except for the largest group. This fix is done at the expense of load-balance, but is necessary for these methods to be robust in MPACT. To ensure that no subdomain wraps around another, a fix is applied after the graph partitioning process. If a subdomain wraps around another, then the concave subdomain will be given the modules it wraps around.

A group of ray-tracing modules in MPACT can be abstracted into a graph. Each vertex will have weight corresponding to the number of cells contained in the module. Edges can be drawn between directly neighboring ray-tracing modules. This represents communication in MPACT's MoC solver. Transport source iterations converge slowly, so MPACT relies on the CMFD [20] acceleration method. CMFD acceleration is performed by constructing a sparse linear system based on the finite differenced diffusion operator and then solving for the largest eigenpair of that linear system. In MPACT, solving the linear system is handled by a third-party library, PETSc [21].

For 2-D simulations, the application of graph partitioning methods is clear: abstract the 2-D mesh into a graph for partitioning. However, for 3-D, there are additional concerns. MPACT's primary 3-D transport method is the 2D-1D method, in which the MoC is used in the radial directions, and a lower-order solver couples axial planes [22]. For 2D-1D simulations, MPACT currently restricts spatial domains to be aligned in both the radial and axial directions; this is due to implementation, and is not a general requirement of the methods.

To comply with MPACT's restrictions on 3-D spatial domains, the current approach is to axially average module weights (numbers of cells), perform a 2-D graph partitioning on a single plane, and apply the resulting partitioning to all axial planes. This approach will restrict the number of spatial domains to be an integer multiple of the number of planes. This axially and radially aligned scheme is expected to work well in many cases since reactor cores do not typically vary significantly in the axial direction. However, for some designs, this may not be true, and planes near the top or bottom of the core have significantly fewer cells; in these cases, high load imbalance is to be expected.

It is possible to change MPACT's implementation to lift these alignment restrictions. If spatial domains were aligned in only the radial direction, there may be some benefit to load-balance. In this scheme, each axial plane can be assigned an appropriate number of processes, and a separate 2-D decomposition can be performed for each plane. This also lifts restrictions on the number of domains; the number of domains must only be greater than or equal to the number of planes.

If all alignment restrictions were lifted on MPACT's spatial domains, then a direct partitioning of the 3-D core can be performed by abstracting the entire core to a graph. This scheme provides the

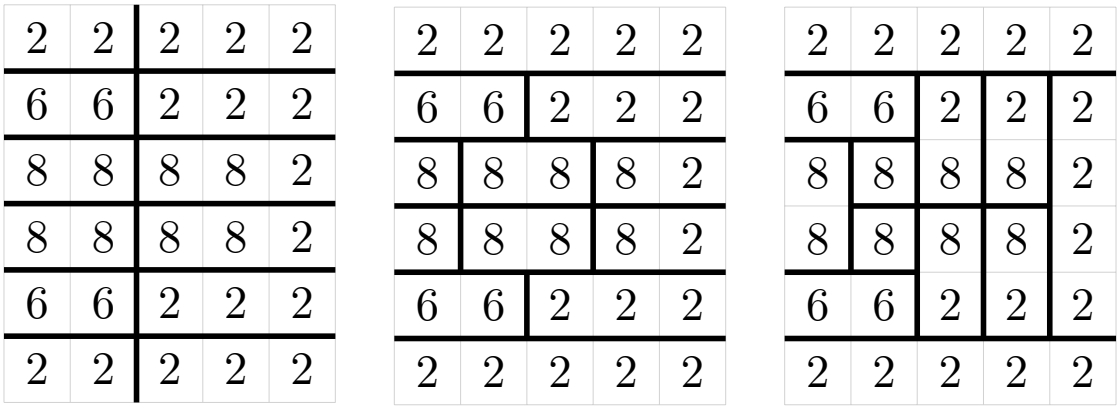

Figure 4.5: Sample decompositions for (a) axially aligned, (b) radially aligned, and (c) generalized decomposition strategies. Rows represent axial planes. Numbers are the vertex weights.

most freedom and would be expected to give the most balanced decompositions. In MPACT's 2D-1D solver, the amount of data communicated radially is significantly larger than that communicated axially, so it may be advantageous to assign the edges connecting the neighboring modules in the axial direction lower weights than those in radial directions. By doing so, the overall communication would be expected to be decreased.

Figure 4.5 shows a comparison of the three hypothetical decomposition schemes, for the purposes of illustration. Looking at the maximum-to-minimum ratio (MMR), as an indicator of load-balance, the strategies have clear differences. The MMR for the axially aligned, radially aligned, and generalized strategies in this example are 4.00, 2.67, and 2.00, respectively. However, it is important to note that the largest domain in each case has the same weight (16), so while the different schemes give different balances, the overall run-times are not expected to be different.

4.5 Results

4.5.1 2-D Results

Results were generated for the planar 2-D version of VERA progression problem 5a [23]. This problem is a quarter core with reflector, barrel, and neutron pad regions surrounding several fuel assemblies, as shown in Fig. 4.6. In the model, there are 257 ray-tracing modules in total, which provides the upper bound for the number of domains. Each subdomain is assigned to a single processor, with a maximum of 36 processors (subdomains) per computational node. Each of the graph decomposition methods was applied to the geometry of this problem, and MPACT was run for each case without applying refinement methods. The assembly-based decomposition was run

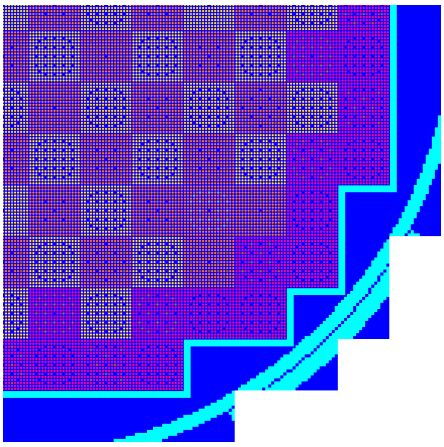

Figure 4.6: VERA progression problem 5a-2d core configuration.

for all possible numbers of subdomains: 1, 4, 16, 73, and 257. The possible numbers of subdomains are limited by powers of 4 (8 in 3-D), until subdomains would be located entirely outside the core shape. It is also possible to decompose into the fuel assemblies or ray-tracing modules, in this case 73 and 257 respectively. Example decompositions for 73 subdomains are shown in Fig. 4.7.

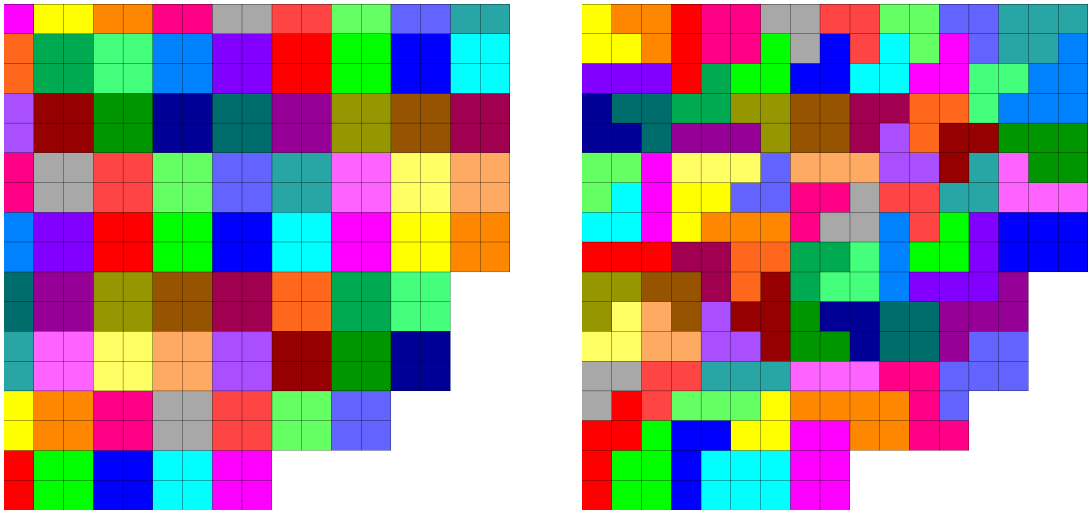

(a) Assembly-based decomposition method.

(b) REB partitioning method.

Figure 4.7: Example decompositions for 73 subdomains for VERA progression problem 5a-2d. Each color represents a different subdomain.

4.5.1.1 Load-Balance

In MPACT, each spatial subdomain is simulated concurrently. After each iteration, parallel boundary conditions are communicated and updated in parallel. The time for solve routines is measured for each subdomain, as is the MoC communication time. However, the communication time includes

time spent waiting for other subdomains to finish computation; that is, blocking communication.

This parallel iteration scheme means that the wall-time of each iteration is controlled by the subdomain with the longest run-time; this is expected to be the subdomain with the largest number of cells. However, the wall-time is not the only important consideration; it is important to consider how well the computational resources are used. A measure for how well computational resources are used is the parallel efficiency, as defined by

$$E \equiv \frac{T_s}{N \cdot T}, \tag{4.4}$$

where T_s is the time in serial, and T is the time in parallel with N processes.

If runtime is highly correlated with the largest number of cells in a subdomain, then this efficiency is expected to be related to the largest *fraction* of cells in a subdomain. Specifically, the parallel efficiency is expected to be inversely proportional to the ratio of the largest fraction of cells to the optimal fraction of cells. In an ideally balanced decomposition, each subdomain would have $1/N$ cell fraction. By comparing the maximum cell fraction to this optimal value, one can estimate how much longer the simulation will take compared to an ideal decomposition, neglecting serial code sections and overhead.

Higher parallel efficiency indicates better utilization of the available computational resources, and lower runtime. The expectation is that higher parallel efficiency can be obtained by having a largest cell fraction closer to the optimal cell fraction. As seen in Fig. 4.8, the REB method is expected to have slightly better parallel efficiency than the other methods for many cases. It is also expected that for a low number of subdomains, the assembly-based decomposition will result in significantly lower parallel efficiency. However, for large numbers of subdomains, the assembly-based decomposition is expected to result in comparable parallel efficiency to the graph partitioning methods.

4.5.1.2 Communication

In MPACT, parallel boundary conditions are communicated concurrently. However, the measurement of communication time includes any time spent waiting for other subdomains to complete their calculations. Generally, the time spent sending receiving parallel boundary conditions is relatively small. This time is expected to increase with the weight of edges cut by parallel boundaries.

Figure 4.9 shows that the number of edges cut increases as the number of domains increases. This indicates that time sending and receiving parallel boundary conditions is expected to increase with the number of subdomains. As the number of subdomains increases, the time spent sending and receiving parallel boundary conditions is expected to increase as more data is communicated. However, the time difference between the slowest and fastest subdomains decreases, so the overall

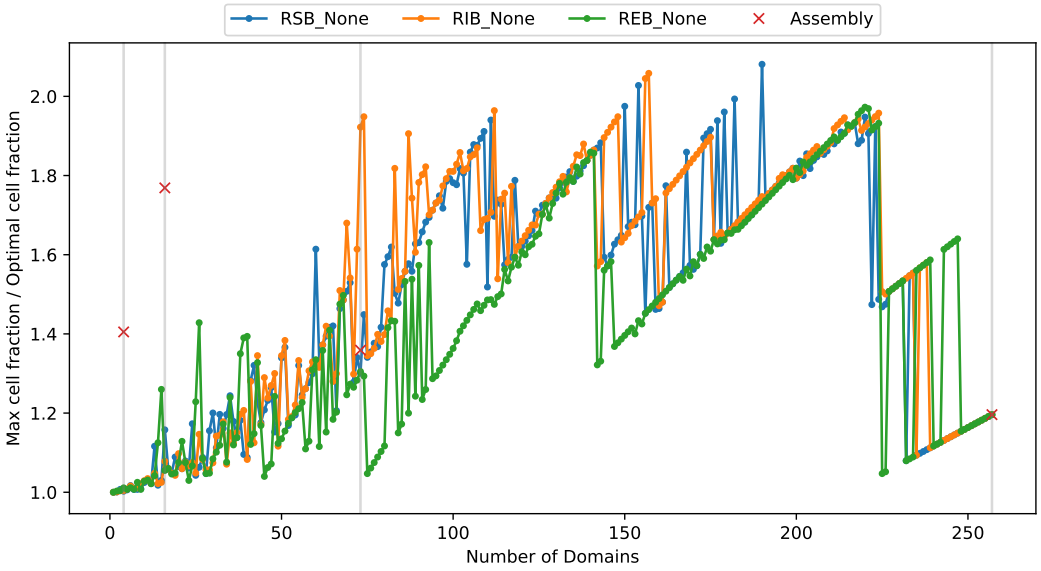

Figure 4.8: Ratio of largest fraction of cells to the optimal fraction of cells as a function of number of subdomains for each partitioning method without refinement.

communication time measurement is expected to decrease. Because subdomains in the assembly-based decomposition are rectangular, the number of edges cut is typically lower than in the graph partitioning methods.

4.5.1.3 MPACT Results

As expected, the total and MoC run-times are highly correlated with the largest fraction of cells in any subdomain, as shown in Fig. 4.10. Both total and MoC run-times are very highly correlated with the largest fraction of cells in a subdomain, indicating that this metric can be used to estimate the relative run-times of decompositions. The assembly-based decomposition method was not used in this correlation, as there are only a few data points available.

Utilization of computational resources is also an important aspect for a high performance simulation code; this can be measured by the parallel efficiency. The total parallel efficiency is shown in Fig. 4.11 for each decomposition method. As the core becomes more decomposed, the parallel efficiency drops off rapidly, approaching around 20%. Generally, the graph partitioning methods result in similar parallel efficiency, though the REB method appears to give very slightly higher efficiency in many cases. The assembly-based decomposition method has significantly lower parallel efficiency when there are few subdomains. However, for the moderately decomposed problem (73 subdomains) the assembly-based decomposition method results in significantly higher parallel efficiency. This was not initially expected, as the largest subdomain has a cell fraction similar to that of the graph partitioning methods.

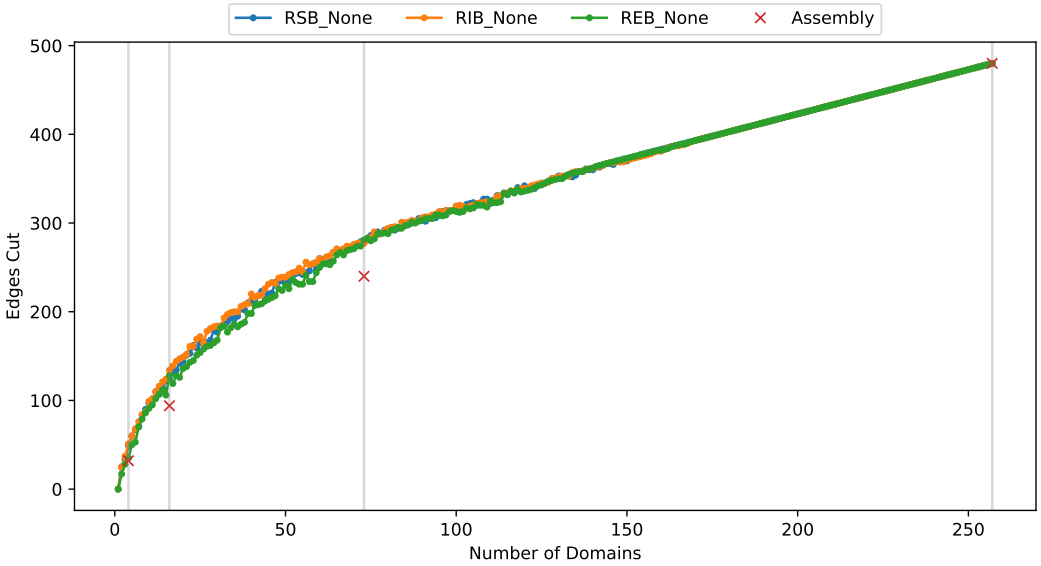

Figure 4.9: Number of edges cut as a fraction of number of domains for each partitioning method without refinement.

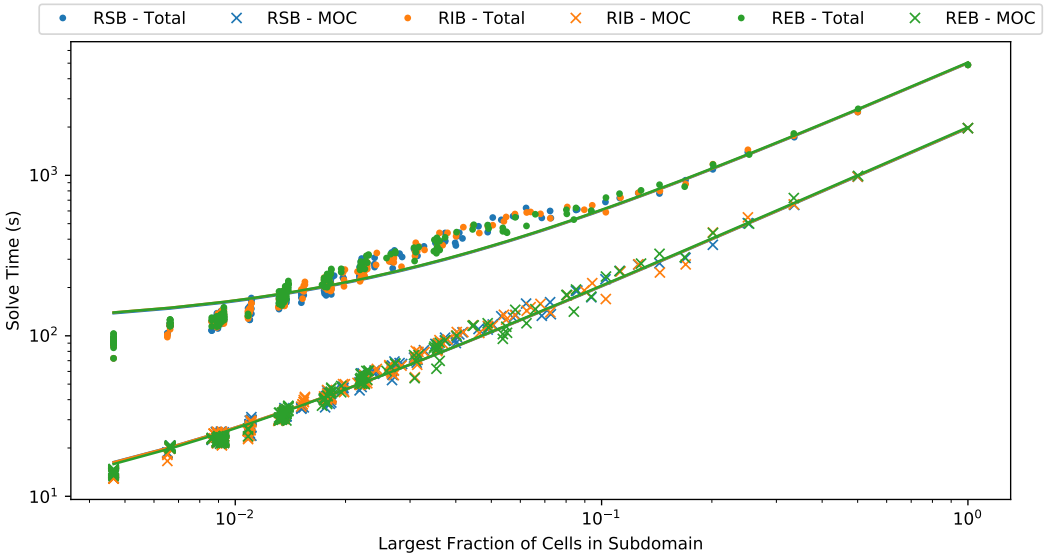

Figure 4.10: Correlation of total and MoC run-times to the largest fraction of cells in a subdomain for each partitioning method.

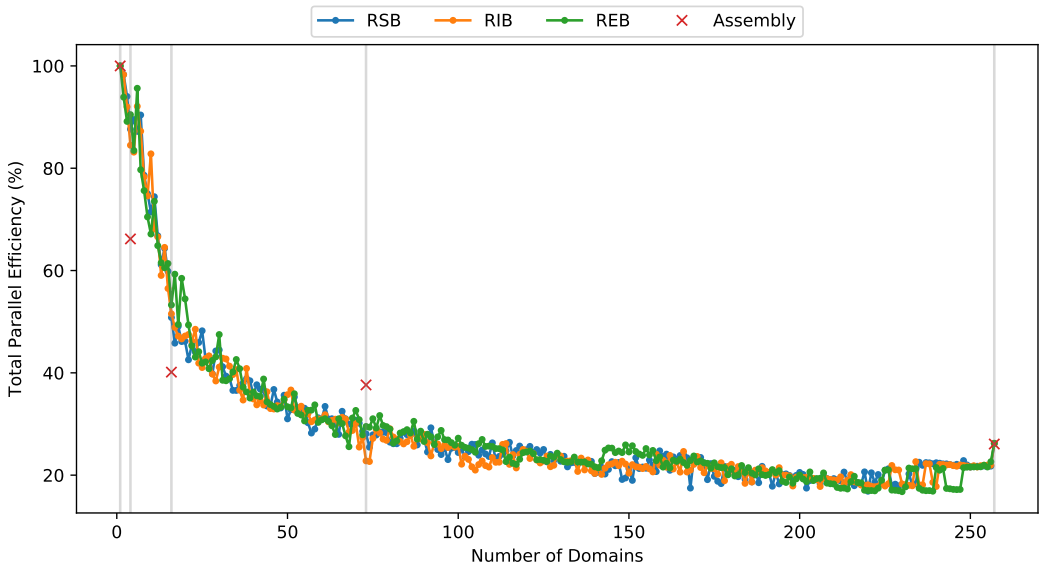

Figure 4.11: The total parallel efficiency for each partitioning method as a function of the number of domains.

As parallel boundary conditions have a more significant effect on the solution within each subdomain, the convergence rate decreases. This occurs as subdomains become smaller (geometrically), or as they become more "jagged." These jagged parallel boundaries cause re-entrant rays, in which a single ray in the MoC will re-enter the subdomain after leaving. These re-entrant rays will *not* occur in the assembly-based decomposition, because subdomains are forced to be rectangular. This can be observed in Fig. 4.7. The number of MoC iterations required for convergence in each case is shown in Fig. 4.12. There is not a significant increase in the number of outer iterations as the subdomains become smaller, this is consistent with previous results in parallel accelerated transport calculations [24–26]. The increase in number of iterations would be expected to be much more significant in an unaccelerated transport calculation. It may be possible to consider spectral information, such as subdomain optical thickness or scattering ratios, during decomposition to allow for a smaller increase in required iterations; however, this will only have an effect at moderately decomposed problems.

By examining the parallel efficiency of *runtime per iteration* these spectral effects are eliminated and the scaling of the solvers in parallel can be determined. As shown in Fig. 4.13, the total parallel efficiency per iteration decreases as the core becomes more decomposed, limiting toward 25%. However, if only the MoC solver time is being examined, the parallel efficiency per iteration decreases at a much slower rate as shown in Fig. 4.14. This indicates that the MoC solver in MPACT is highly efficient in parallel, and that other components of MPACT are the bottleneck in parallel simulations. Furthermore, for both total and MoC run-times, the graph partitioning methods give

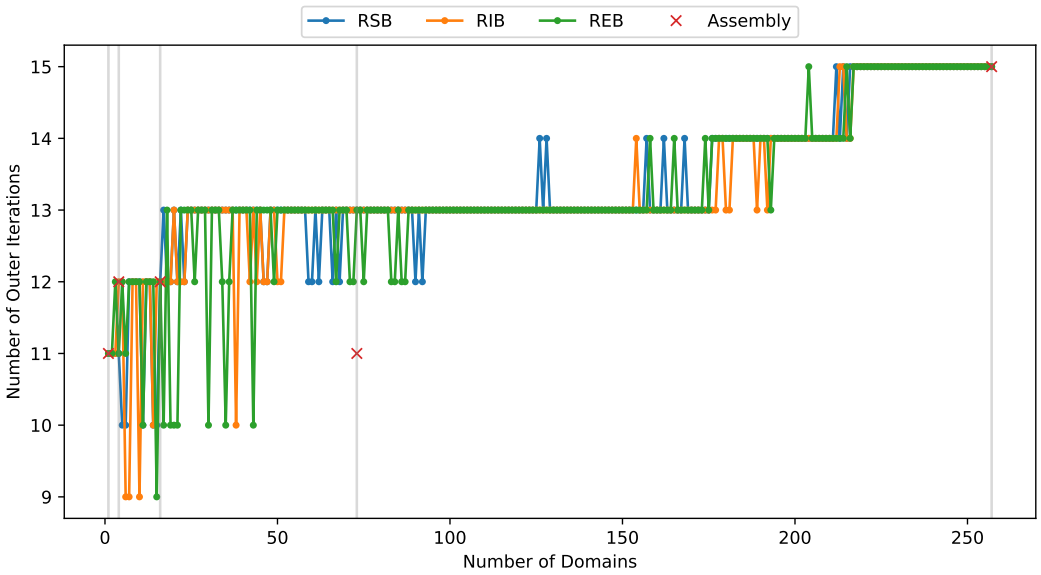

Figure 4.12: The number of iterations used by each decomposition method as a function of the number of subdomains.

comparable parallel efficiencies. The assembly-based decomposition method still results in lower efficiency when using few subdomains, but for high numbers of subdomains, it is comparable with the graph partitioning methods.

Finally, the ratio of the optimal cell fraction to the maximum cell fraction is expected to be proportional to the parallel efficiency per iteration of the MoC solver. As shown in Fig. 4.15, the parallel efficiency is correlated with the the ratio of optimal-to-maximum cell fractions, though it is not correlated as strongly as the runtime with the maximum cell fraction. This indicates that this ratio can be used to estimate the parallel efficiency of the MoC solver for a decomposition. Even isolating the effect due to increased numbers of iterations, there is a significant spread in parallel efficiency as a function of the optimal to maximum cell fraction ratio; this can be explained by the fact that significantly different numbers of domains (processes) can result in similar fractions. This is clearly observed in Fig. 4.8.

4.5.1.4 CMFD Acceleration

In MPACT, the two main solvers contributing to runtime are the MoC solver and CMFD acceleration, each of which is parallelized using the same computational resources. From Fig. 4.16, the MoC and CMFD solvers take similar amounts of time in serial; however, as more subdomains are used, the fractional runtime of CMFD increases to almost 70% of the total. This indicates that the parallel efficiency is quite low for MPACT's CMFD linear system solvers, which heavily leverage PETSc [21] for parallelism.

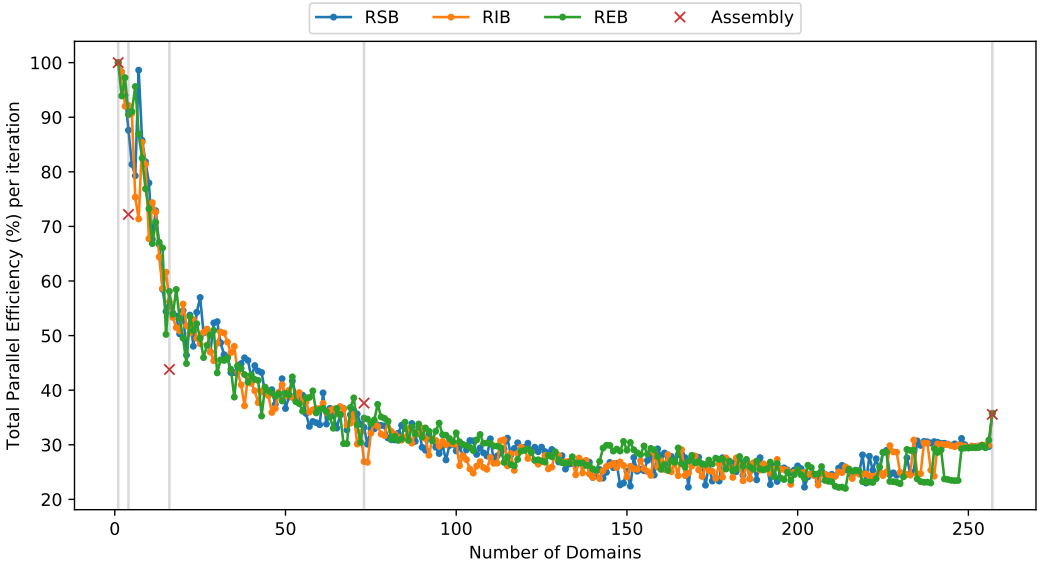

Figure 4.13: The total parallel efficiency per iteration for each partitioning method as a function of the number of domains.

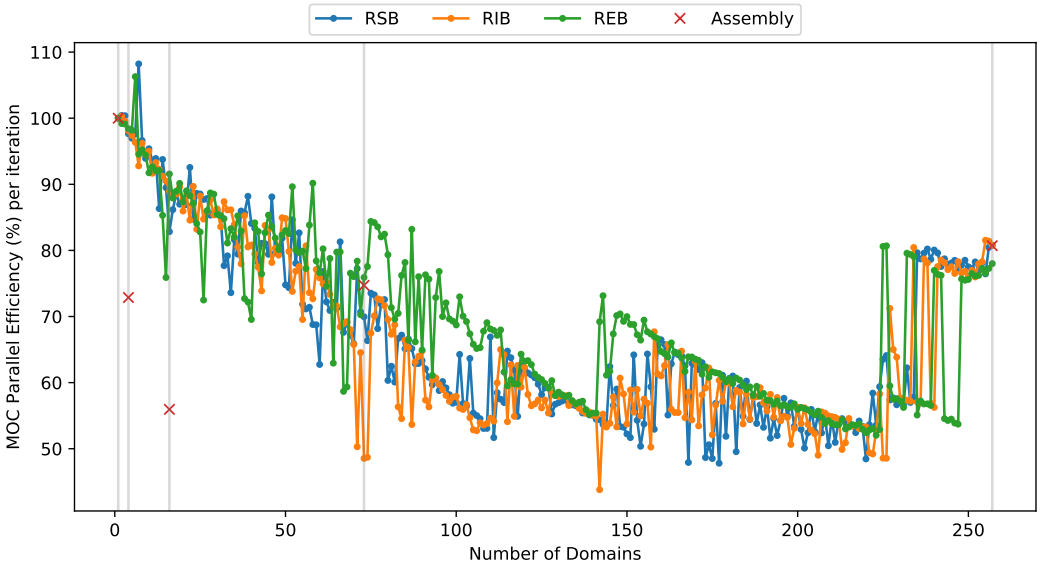

Figure 4.14: The MoC parallel efficiency per iteration for each partitioning method as a function of the number of domains.

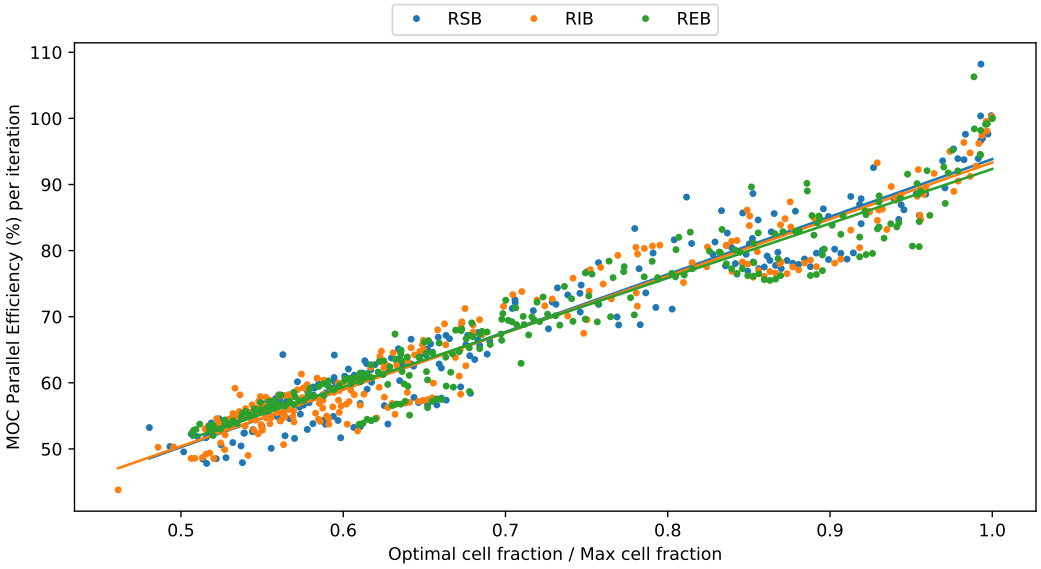

Figure 4.15: Correlation of the MoC parallel efficiency per iteration and the ratio of optimal and maximum cell fractions for each of the partitioning methods.

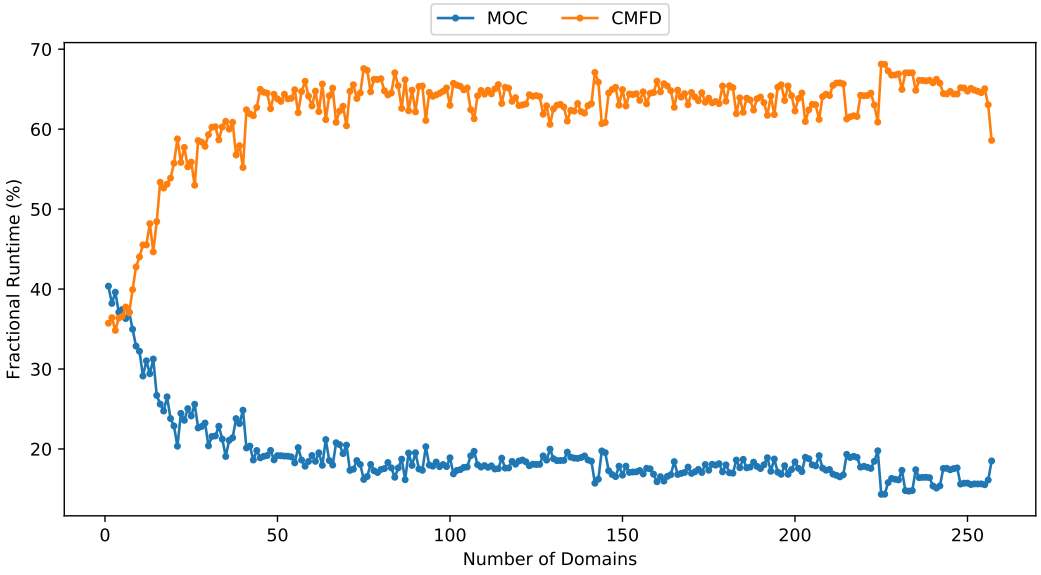

Figure 4.16: Fractional runtime of the MoC solver and CMFD acceleration method in MPACT for varying number of domains with the REB partitioning method.

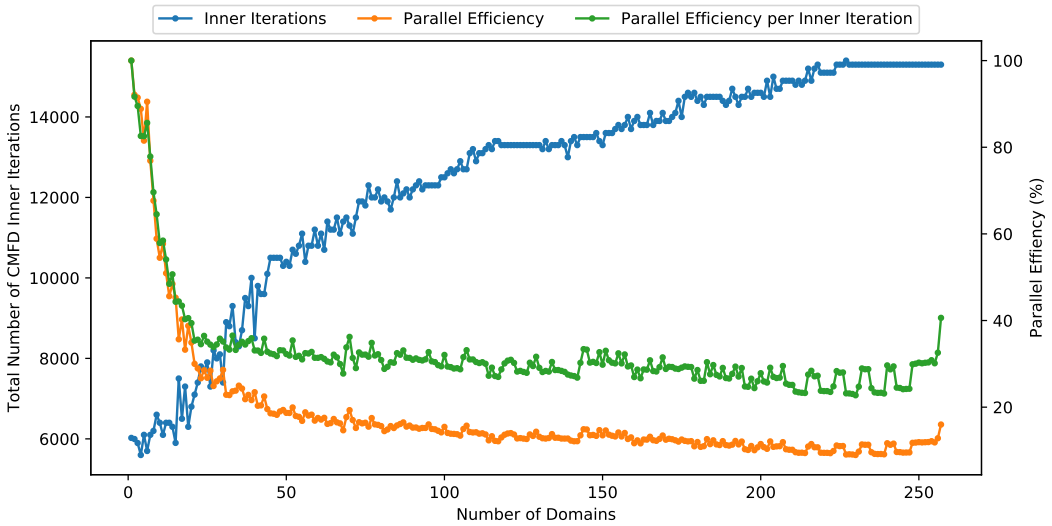

Figure 4.17: The total number of CMFD inner iterations, parallel efficiency, and parallel efficiency per inner iteration for varying number of domains with the REB partitioning method.

Similar as the number of outer transport iterations, as subdomains become smaller, it is expected the CMFD linear system will require more iterations for convergence; this is shown for the REB partitioning method in Fig. 4.17. However, by considering the parallel efficiency per inner iteration, these convergence effects can be eliminated, and the parallel scaling of the linear system solvers can be examined. Figure 4.17 shows that the parallel efficiency of the linear system solvers used in MPACT for CMFD calculations is quite low, limiting to around 30%. By using a linear system solver that has better parallel scaling [27], the overall parallel efficiency of MPACT may be increased. However, these results also indicate that the parallel efficiency is, in part, lowered by spectral effects, which will not be eliminated by a more efficient parallel linear solver.

4.5.2 3-D Results

As shown in Section 4.5.1, decomposition metrics can be used to estimate the runtime and parallel efficiency without needing to run the simulations. There are different approaches to decomposition in 3-D; these are discussed in more detail in Section 4.4. Decompositions were performed without refinement for three different 3-D decomposition schemes: axially and radially aligned (ARA), radially aligned (RA), and unrestricted (UR). Given fewer restrictions, the resulting decompositions were expected to be more balanced. Decompositions were performed on VERA progression problem 5a-0 in 3-D [23] with 58 axial planes, but the simulations for this problem were not run.

The ratio of maximum cell fraction to optimal cell fraction can easily be converted to the maximum cell fraction by dividing by N. For brevity, only this load balance metric is shown herein. The resulting decompositions from the ARA approach are very similar to those in the 2-D case.

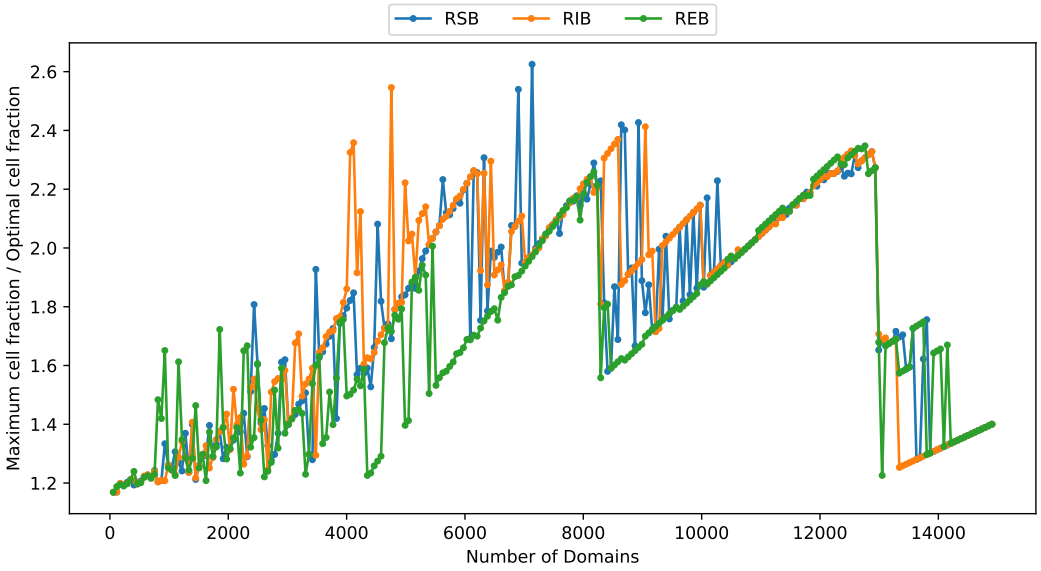

Figure 4.18: Maximum-to-optimal cell fraction ratio for each partitioning method as a function of number of domains in the axially and radially aligned (ARA) scheme.

Just as in the 2-D case, the maximum-to-optimal cell fraction ratio is lowest for the REB method as compared to the other partitioning methods for many cases, as seen in Fig. 4.18. This indicates that, barring any differences in the number of iterations, the REB method is expected to have slightly higher parallel efficiencies.

In the RA scheme, a separate decomposition is performed for each axial plane, with an appropriate number of subdomains based on the number of cells in the plane. Unlike in the 2-D case, the REB method seems to perform significantly worse than the other two methods for low numbers of subdomains. For highly decomposed cores, the REB method seems to perform slightly better than the other partitioning methods. Additionally, by comparing the magnitude of the ratios in Fig. 4.19 and Fig. 4.18, it is clear that the RA approach typically has less imbalance.

Finally, the UR approach decomposes the 3-D core by directly abstracting the entire core into a graph. The REB method is significantly more imbalanced than other methods for lower numbers of subdomains; however, for highly decomposed cores, the REB method outperforms the other methods, as shown in Fig. 4.20. Additionally, for highly decomposed problems, both the RSB and RIB methods seem to have worse balance when using the UR scheme compared to the RA scheme.

The approach currently used in MPACT is the axially and radially aligned 3-D decomposition scheme. If other approaches were to be used, the implementation of parallel communication in the 2D-1D method would need to be reworked. To justify these changes, the less restricted approaches would need to offer significant advantages over the current approach. Figures 4.21 to 4.23 examine the maximum cell fraction of each scheme relative to the current scheme. The smaller the relative

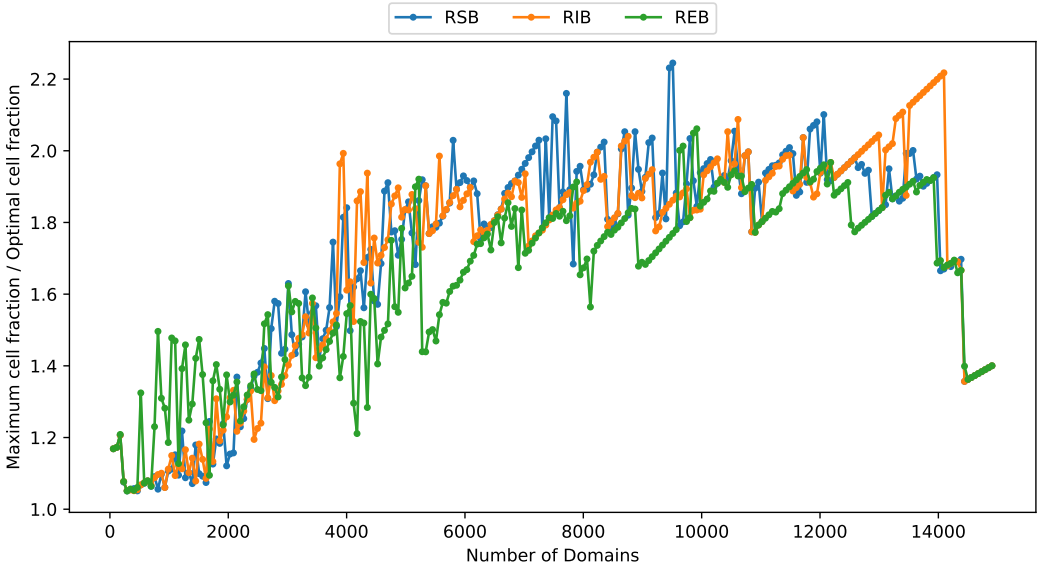

Figure 4.19: Maximum-to-optimal cell fraction ratio for each partitioning method as a function of number of domains in the radially aligned (RA) scheme.

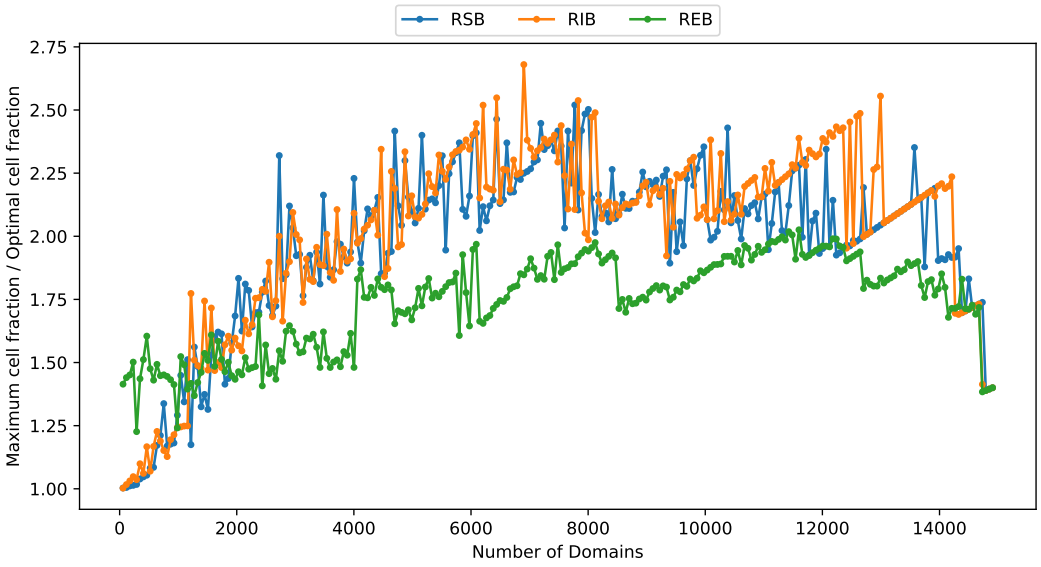

Figure 4.20: Maximum-to-optimal cell fraction ratio for each partitioning method as a function of number of domains in the unrestricted (UR) scheme.

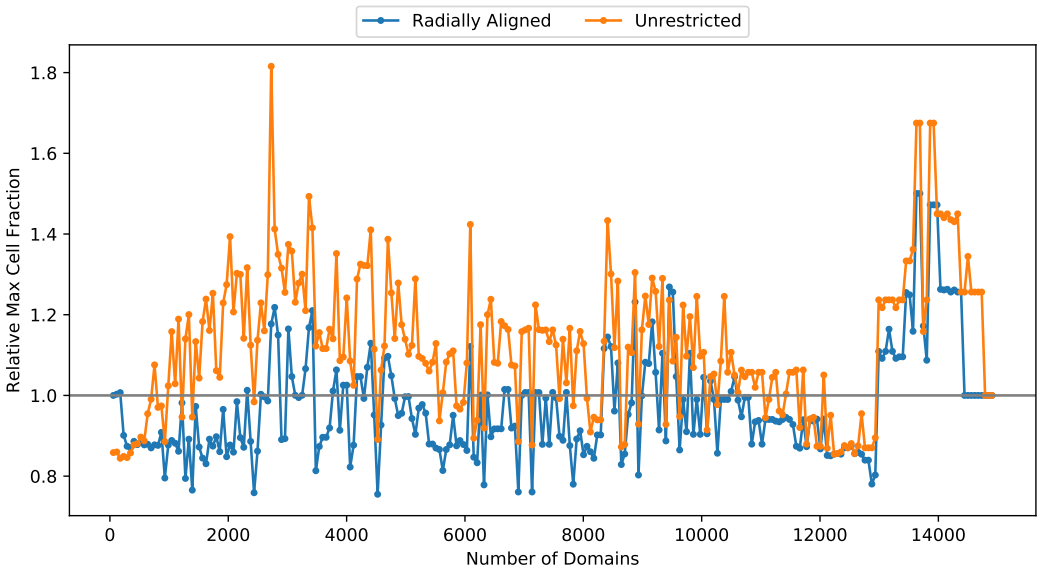

Figure 4.21: Maximum cell fraction relative to the axially and radially aligned (ARA) approach for the RSB partitioning method.

maximum cell fraction, the lower the expected runtime will be.

For most applications, reactor cores in MPACT are not highly decomposed with, at maximum, on the order of 30 subdomains per axial plane. In this context, modestly decomposed cores are defined as those with fewer than 2,000 subdomains; otherwise, the core is considered highly decomposed. For the RSB and RIB methods, the RA approach is expected to give 10% better performance than the ARA approach on average. For highly decomposed cases, these partitioning methods are only expected to give an average of 2 – 3% better performance. On average, the UR approach is expected to give *worse* performance by more than 10% using these partitioning methods. However, for the REB partitioning method, the RA approach is only expected to give 3% better performance on average. Typically, the UR approach is still expected to result in worse performance. This may be a result of the problem examined in this work which had axial planes that were fairly well balanced. By giving the graph partitioning methods more degrees of freedom the heuristic graph partitioning methods perform worse overall. Multi-level partitioning methods reduce the degrees of freedom during coarsening and may be more appropriate in these cases.

4.6 Partition Refinement

4.6.1 Partition Refinement Methods

The Kernighan-Lin algorithm [28] is often described as one of the earliest developed graph partitioning algorithms; however, the algorithm does not actually create a partitioning of the graph, it

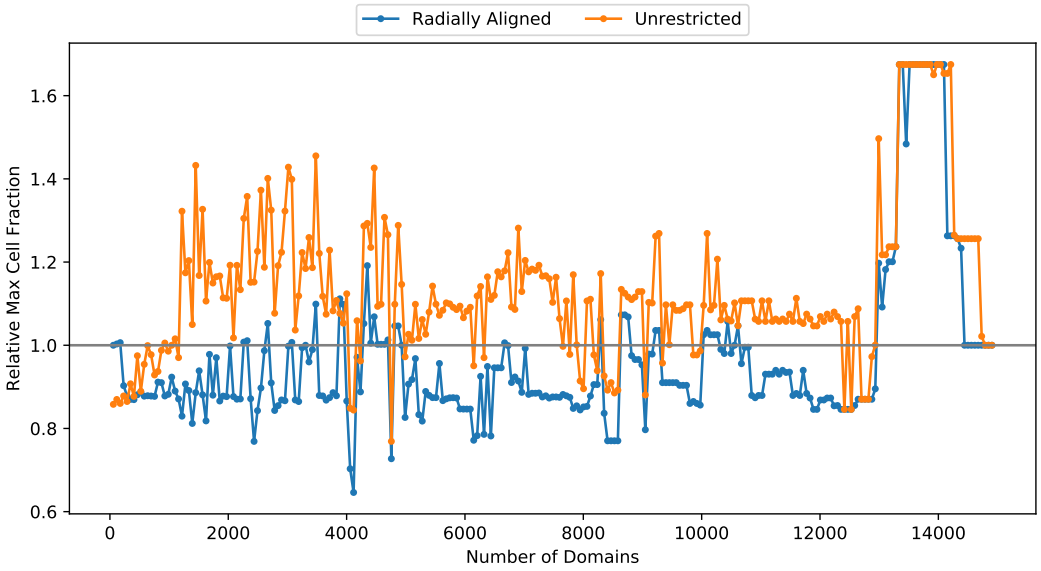

Figure 4.22: Maximum cell fraction relative to the axially and radially aligned (ARA) approach for the RIB partitioning method.

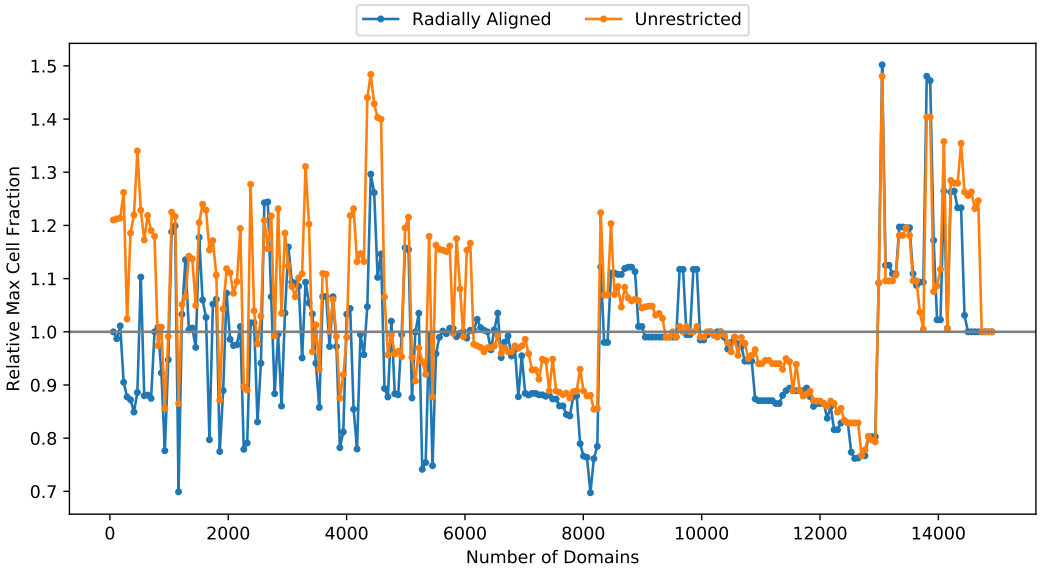

Figure 4.23: Maximum cell fraction relative to the axially and radially aligned (ARA) approach for the REB partitioning method.

improves, or refines, the quality by reducing the number of edges cut between existing partitions [6]. Therefore, in this work, this method and a modified version of it are called *refinement methods*.

As suggested by Pothen [12], the RSB method or other partitioning methods can create a high quality initial partitioning to use in the Kernighan-Lin algorithm. Significant improvements have been made to the efficiency of the original Kernighan-Lin algorithm [29]; however, the graphs of concern in this work are relatively small, and graph decomposition time is negligible when compared to the overall simulation runtime. Two partition refinement methods were examined: the Kernighan-Lin algorithm [28] and a modification to the Kernighan-Lin algorithm which takes some geometric information of the graph into account [5].

The investigated partition refinement algorithms reduce the weight of edges cut between two partitions by swapping vertex pairs between the partitions iteratively. The original Kernighan-Lin algorithm operates entirely on the connectivity of the graph, while the modified Spatial Kernighan-Lin algorithm uses both connectivity and geometric information from the graph.

For each vertex in the graph, D is defined as

$$D_i \equiv E_{E,i} - E_{I,i}, \tag{4.5}$$

where $E_{E,i}$ is the sum of edge weights from vertex i connecting with vertices outside the partition containing vertex i, and $E_{I,i}$ is the sum of edge weights from vertex i connecting with vertices within the partition containing vertex i. The reduction in communication or "gain," from swapping a pair of vertices (a, b) is defined as

$$g_{(a,b)} \equiv D_a + D_b - 2c_{a,b}. \tag{4.6}$$

The Kernighan-Lin algorithm, given in Algorithm 7, is a greedy algorithm, in that it will swap a pair (a, b) with maximal g at the current step. The idea is that by doing this iteratively, the algorithm will lead to a minimized cut-size; in reality, the algorithm will often get stuck in local minima that do not have a global minimized cut-size. Additionally, there may be multiple pairs (a, b) with the same maximal gain value: the algorithm will only consider one of these pairs.

The Spatial Kernighan-Lin algorithm, given in Algorithm 8, is an adaptation of the Kernighan-Lin algorithm which accounts for the multiple pairs with maximal gain. This algorithm prioritizes vertex pairs which are geometrically distant from one another. The idea behind this modification is that to minimize the edge-cut, the cut should be as straight as possible. By prioritizing distant vertex pairs, the bisector is typically "straightened" out; this process can be likened to pulling on the ends of a string in order to straighten it.

Algorithm 7 Kernighan-Lin Algorithm, with input graph $G(V, E)$, and vertex sets A and B within the graph.

procedure KERNIGHAN-LIN($G(V, E), A, B$)
  $g_m = 1$
  while $g_m > 0$ **do**
    $W_A = \sum_{i \in A} w_i$
    $W_B = \sum_{i \in B} w_i$
    Compute $D \forall V$ (Equation (4.5))
    Let a_v, b_v, g_v be empty sets
    for $n = 1$ to $N/2$ **do**
      Find unmarked pair (a, b) such that:
        1. $a \in A$ and $b \in B$
        2. g is maximized (Equation (4.6))
      $\widehat{W}_A = W_A + w_b - w_a$
      $\widehat{W}_B = W_B + w_a - w_b$
      if MAX(W_A, W_B) $\geq$ MAX($\widehat{W}_A, \widehat{W}_B$) **then**
        Append a to a_v, b to b_v, and g to g_v
        Update D values as if a, b have been swapped
        $W_A = \widehat{W}_A$
        $W_A = \widehat{W}_B$
      else
        End search
      end if
    end for
    Find k maximizing $g_m = \sum_{i=1}^{k} g_v(i)$
    if $g_m > 0$ **then**
      Exchange vertices in $a_v(1 : k)$ and $b_v(1 : k)$
    end if
  end while
end procedure

Algorithm 8 Spatial Kernighan-Lin Algorithm, with input graph $G(V, E)$, and vertex sets A and B within the graph.

procedure SPATIAL KERNIGHAN-LIN($G(V, E), A, B$)
  $g_m = 1$
  while $g_m > 0$ **do**
    $W_A = \sum_{i \in A} w_i$
    $W_B = \sum_{i \in B} w_i$
    Compute $D \; \forall \; V$ (Equation (4.5))
    Let a_v, b_v, g_v be empty sets
    for $n = 1$ to $N/2$ **do**
      Allow (f_a, f_b) to be sets from A, B satisfying:

1. $a \in A$, $b \in B$
2. g is maximized (Equation (4.6))
3. a and b are on the boundary between A and B

      Find pair (f'_a, f'_b) such that distance is maximized
      if No pair found **then**
        Search using standard Kernighan-Lin rules
      end if
      $\widehat{W}_A = W_A + w_b - w_a$
      $\widehat{W}_B = W_B + w_a - w_b$
      if MAX(W_A, W_B) $\geq$ MAX($\widehat{W}_A, \widehat{W}_B$) **then**
        Append a to a_v, b to b_v, and g to g_v
        Update D values as if a, b have been swapped
        $W_A = \widehat{W}_A$
        $W_A = \widehat{W}_B$
      else
        End search
      end if
    end for
    Find k maximizing $g_m = \sum_{i=1}^{k} g_v(i)$
    if $g_m > 0$ **then**
      Exchange vertices in $a_v(1:k)$ and $b_v(1:k)$
    end if
  end while
end procedure

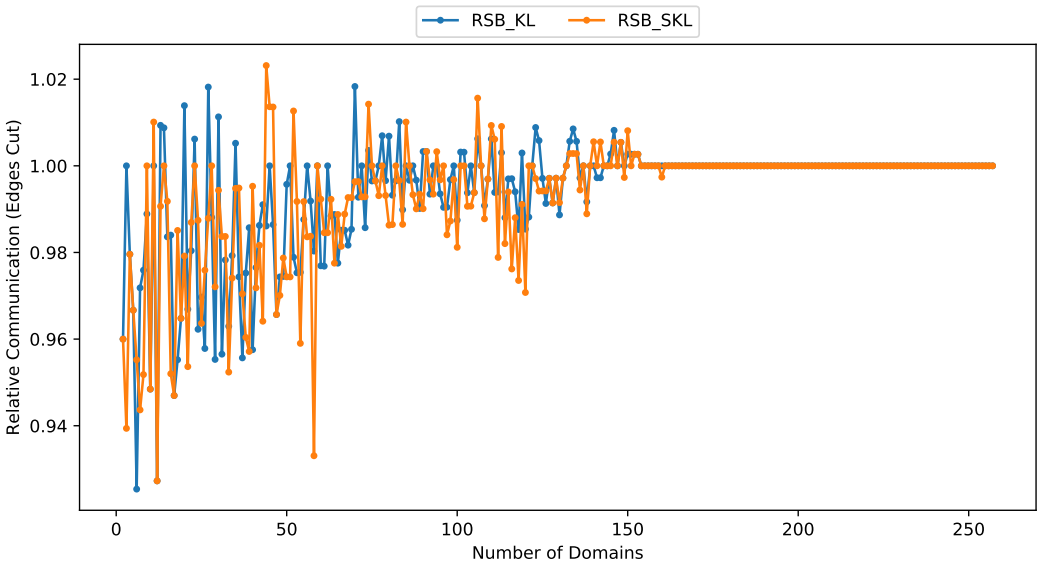

Figure 4.24: Communication relative to the RSB method without refinement as a function of number of domains for each refinement method using the RSB partitioning method.

4.6.2 Partition Refinement Results

In Section 4.6.1, refinement methods are introduced as a method for further reducing communication. Figure 4.24 shows that both refinement methods are able to slightly reduce the number of edges cut compared to the cases without refinement for RSB. Similar trends are observed for the other partitioning methods. While these refinement methods offer a slight reduction in communication, the parallel efficiency due to load imbalance may be negatively affected by applying refinement, as shown in Fig. 4.25. Communication is not expected to have as significant of an effect as load imbalance, so for the simulations in MPACT, partitioning methods were used without refinement.

4.7 Conclusions

Spatial decomposition is a useful technique for reducing the runtime of simulations and is necessary to run whole-core high fidelity reactor calculations. Using graph partitioning methods to decompose the spatial domain of a core has significant advantages when compared to previous decomposition methods. Graph partitioning allows for the usage of an arbitrary number of spatial subdomains, and it generalizes to different module geometries such as a hexagonal lattice. Graph partitioning methods generally provide high quality decompositions that increase parallel efficiency. These automated spatial decomposition methods improve code usability and flexibility by allowing users to easily fit simulations to any number of processors.

However, for highly decomposed cores, the convergence rate decreases due to jagged subdomain

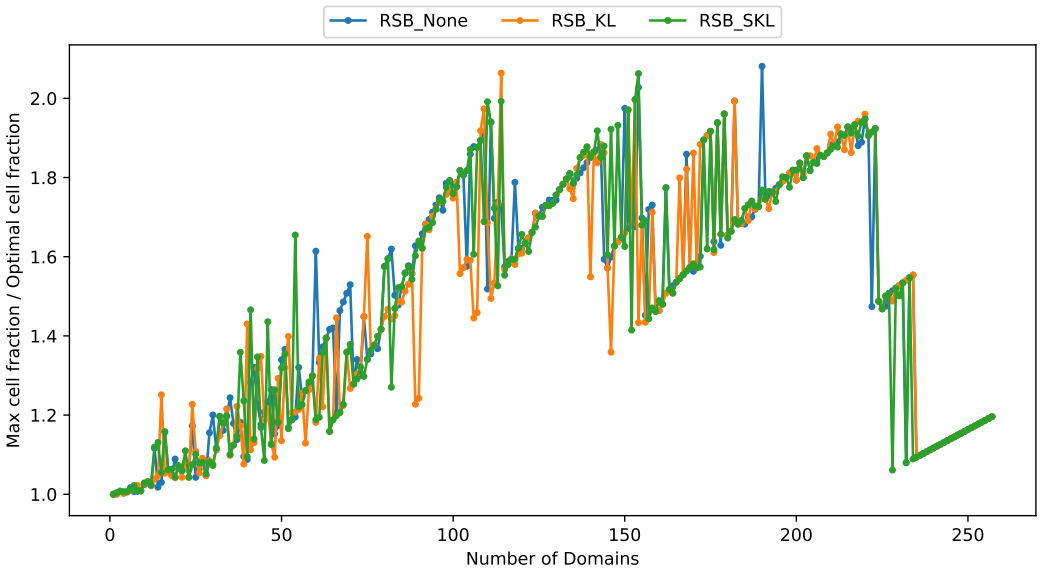

Figure 4.25: Ratio of maximum cell fraction to optimal cell fraction for the RSB partitioning method with each refinement method.

boundaries. This caused graph partitioning methods to significantly reduce runtime for problems that were not highly decomposed but actually increase runtime for highly decomposed problems. This is because the assembly-based decomposition method used rectangular (non-jagged) subdomains. This indicates that it may be advantageous to create a high quality decomposition method that enforces rectangular subdomains. However, this approach will not generalize to other lattice types, such as hexagonal lattices.

In the current MPACT implementation, there is no significant difference in run-times when using any of the three partitioning methods discussed, although REB typically results in slightly lower MoC run-times. The 2-D results indicate that the maximum fraction of cells in a subdomain is highly correlated with the runtime of the simulation. Furthermore, 2-D results indicate that the parallel efficiency of MoC is highly correlated with the ratio of the optimal cell fraction per subdomain to the maximum cell fraction in a subdomain.

In 3-D, MPACT currently requires spatial domains to be axially and radially aligned. If these restrictions are lifted, then other approaches can be used to perform the 3-D spatial decomposition. Three 3-D decomposition approaches were investigated in this work: radial and axial aligned subdomains, radially aligned subdomains, and an approach with no alignment restrictions. The radially aligned approach is expected to out perform the current approach by an average of 10% for typical cases. However, the unrestricted approach is actually expected to perform worse than the current approach on average. This analysis was performed on a 3-D core, which was relatively homogeneous in the axial direction; if a core design were to be more axially heterogeneous, then a

more significant increase in performance might be expected.

The parallel efficiency is a measure of how well computational resources are utilized in parallel applications. MPACT's overall parallel efficiency decreases rapidly as more domains are used due to two factors: increased number of iterations, and the inefficiency of parallel CMFD solves. For the 2-D VERA progression problem 5a, the overall parallel efficiency of MPACT dropped to nearly 20%. The parallel efficiency of only the MoC computations in MPACT drops to between 40–60%, while the parallel efficiency of the CMFD computation drops to $<20\%$. This causes the CMFD computation to dominate runtime in spatially decomposed cases, and motivates the implementation of a more efficient parallel linear system operator in MPACT rather than using a third-party library.

Bibliography

[1] J.R. Askew. *A Characteristics Formulation of the Neutron Transport Equation in Complicated Geometries*. 1972.

[2] MPACT Team. *MPACT Theory Manual v2.2.0*. Tech. rep. Consortium for Advanced Simulation of Light Water Reactors, 2016.

[3] Andrew P Fitzgerald et al. "Spatial decomposition of structured grids for nuclear reactor simulations". In: *Annals of Nuclear Energy* 132 (2019), pp. 686–701. ISSN: 0306-4549. DOI: 10.1016/j.anucene.2019.06.054.

[4] Geoffrey Alexander Gunow. "Full Core 3D Neutron Transport Simulation Using the Method of Characteristics with Linear Sources". Doctoral. Massachusetts Institute of Technology, 2018.

[5] Andrew Fitzgerald et al. "Automated Decomposition of a Structured Grid". In: *Transactions of the American Nuclear Society*. Vol. 117. Washington D.C., 2017, pp. 731–734.

[6] Ulrich Elsner. *Graph partitioning A Survey*. Tech. rep. Technische Universitat Chemnitz, 1997, p. 52. URL: http://citeseerx.ist.psu.edu/viewdoc/summary?doi=10.1.1.54.2060.

[7] Y.F. Yao and B.E. Richards. "Parallel CFD Computation on Unstructured Grids". In: *Parallel Computational Fluid Dynamics*. Elsevier, 1998, pp. 289–296. DOI: 10.1016/B978-044482849-1/50035-X.

[8] Shinya Kosaka and Etsuro Saji. "Transport theory calculation for a heterogeneous multi-assembly problem by characteristics method with direct neutron path linking technique". In: *Journal of Nuclear Science and Technology* 37.12 (2000), pp. 1015–1023. ISSN: 00223131. DOI: 10.1080/18811248.2000.9714987.

[9] Shane Stimpson and Benjamin Collins. "Flexible Spatial Partitions in MPACT Through Module-Based Data Passing". In: *Transactions of the American Nuclear Society*. Vol. 116. San Francisco, 2017, pp. 654–657.

[10] G. M. Morton. *A computer Oriented Geodetic Data Base; and a New Technique in File Sequencing*. Tech. rep. Ottawa, Canada: IBM Ltd., 1966.

[11] George Karypis and Vipin Kumar. "A fast and high quality multilevel scheme for partitioning irregular graphs". In: *SIAM Journal on Scientific Computing* 20.1 (1998), pp. 359–392.

[12] Alex Pothen, Horst D. Simon, and Kang-Pu Paul Liu. "Partitioning Sparse Matrices with Eigenvectors of Graphs". In: *SIAM Journal on Matrix Analysis and Applications* 11.3 (1989), pp. 430–452.

[13] H. D. Simon. "Partitioning of unstructured problems for parallel processing". In: *Computing Systems in Engineering* 2.2-3 (1991), pp. 135–148. ISSN: 09560521. DOI: 10.1016/0956-0521(91)90014-V.

[14] Daniel A. Spielman and Shang Hua Teng. "Spectral partitioning works: Planar graphs and finite element meshes". In: *Linear Algebra and Its Applications* 421.2-3 SPEC. ISS. (2007), pp. 284–305. ISSN: 00243795. DOI: 10.1016/j.laa.2006.07.020.

[15] Shang Hsien Hsieh, Glaucio H. Paulino, and John F. Abel. "Recursive spectral algorithms for automatic domain partitioning in parallel finite element analysis". In: *Computer Methods in Applied Mechanics and Engineering* 121.1-4 (1995), pp. 137–162. ISSN: 00457825. DOI: 10.1016/0045-7825(94)00704-Q.

[16] Miroslav Fiedler. "Algebraic Connectivity of Graphs". In: *Czechoslovak Mathematical Journal* 23.2 (1973), pp. 298–305.

[17] N. Floros et al. "Comparative efficiencies of domain decompositions". In: *Parallel Computing* 21.11 (1995), pp. 1823–1835. ISSN: 01678191. DOI: 10.1016/0167-8191(95)00031-7.

[18] Charbel Farhat. "A simple and efficient automatic fem domain decomposer". In: *Computers and Structures* 28.5 (1988), pp. 579–602. ISSN: 00457949. DOI: 10.1016/0045-7949(88)90004-1.

[19] M A Nasra and D T Nguyen. "An algorithm for domain decomposition in finite element analysis". In: *Computers & Structures* 39.3/4 (1991), pp. 277–289.

[20] Kord S. Smith. "Nodal method storage reduction by nonlinear iteration". In: *Transactions of the American Nuclear Society*. Vol. 44. 1983, pp. 265–266.

[21] S. Balay et al. *PETSc Users Manual Revision 3.10*. Tech. rep. Argonne, IL (United States): Argonne National Laboratory (ANL), 2018.

[22] Benjamin Collins et al. “Stability and accuracy of 3D neutron transport simulations using the 2D/1D method in MPACT”. In: *Journal of Computational Physics* 326 (2016), pp. 612–628. ISSN: 10902716. DOI: 10.1016/j.jcp.2016.08.022.

[23] A. T. Godfrey. *VERA Core Physics Benchmark Progression Problem Specifications*. Tech. rep. 4. 2014, pp. 1–173. URL: https://www.casl.gov/sites/default/files/docs/CASL-U-2012-0131-004.pdf.

[24] B.W. Kelley and E.W. Larsen. “CMFD Acceleration of Spatial Domain-Decomposed Neutron Transport Problems”. In: *Physor*. Knoxville, 2012, pp. 1–13.

[25] Shane G Stimpson et al. “Boundary Acceleration Techniques for CMFD-Accelerated 2D-MOC”. In: Kyoto, 2014, pp. 1–11.

[26] Brendan Kochunas et al. “Application of the SDD-Cmfd Acceleration Technique To Parallel 3-D Method of Characteristics Transport”. In: *Physor*. Kyoto, 2014.

[27] Chen Hao et al. “3D whole-core neutron transport simulation using 2D/1D method via multi-level generalized equivalence theory based CMFD acceleration”. In: *Annals of Nuclear Energy* 122 (2018), pp. 79–90. ISSN: 18732100. DOI: 10.1016/j.anucene.2018.08.014.

[28] B.W. Kernighan and S. Lin. “An efficient heuristic for partitioning graphs”. In: *Bell Systems Technical Journal* 49 (1970), pp. 291–308.

[29] C. M. Fiduccia and R. M. Mattheyses. *A Linear-Time Heuristic for Improving Network Partitions*. Tech. rep. Schenectady, NY: General Electric Research and Development Center, 1982, pp. 175–181.

CHAPTER 5

Improved Linear Source Formulation for Multi-physics and 2D/1D Applications

The studies performed in this thesis have made extensive use of the linear-source approximation (LSA) introduced by Ferrer and Rhodes [1]. Through the use of the approximation, as presented in the original work, instabilities and inefficiencies were found. This chapter aims to present two improvements made to this approximation that have been a focus of this research: improved exponential tabulation [2], and an improved formulation for multi-physics and 2D/1D applications [3].

5.1 Exponential Tabulation

The original moment-based LSMoC formulation [1], detailed in Section 3.3, uses several exponential functions:

$$F_1(\tau_m^g) \equiv 1 - e^{\tau_m^g}, \tag{5.1a}$$

$$F_2(\tau_m^g) \equiv 2\left[\tau_m^g - F_1(\tau_m^g)\right] - \tau_{mki}^g F_1(\tau_m^g), \tag{5.1b}$$

$$G_1(\tau_{mki}^g) \equiv 1 + \frac{\tau_{mki}^g}{2} - \left(1 + \frac{1}{\tau_{mki}^g}\right) F_1(\tau_{mki}^g), \tag{5.1c}$$

$$G_2(\tau_{mki}^g) \equiv \frac{2}{3}\tau_{mki}^g - \left(1 + \frac{2}{\tau_{mki}^g}\right) G_1(\tau_{mki}^g), \tag{5.1d}$$

and

$$H(\tau_{mki}^g) \equiv \frac{\tau_{mki}^g}{2} - G_1(\tau_{mki}^g), \tag{5.1e}$$

where τ_m^g is the variable optical thickness, and τ_{mki}^g is the total optical thickness of a segment. Although the functions $F_1(\tau_m^g)$, and $F_2(\tau_m^g)$ are functions of variable τ_m^g, in the implementation of this method in code they are only ever evaluated over the full optical thickness, τ_{mki}^g. The functions, $G_1(\tau_{mki}^g)$, $G_2(\tau_{mki}^g)$, and $H(\tau_{mki}^g)$ all require special treatment around $\tau_{mki}^g = 0$, in this work this is

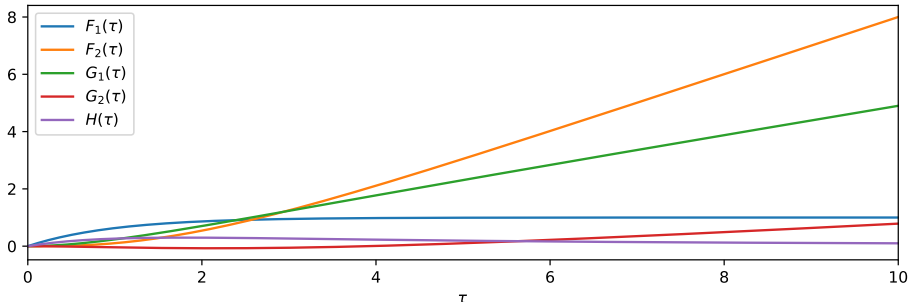

Figure 5.1: The exponential functions, Eqs. (5.1), from 0 to 10.

handled via Taylor interpolation about $\tau^g_{mki} = 0$.

These functions all involve an exponential, $e^{-\tau^g_{mki}}$; although this does not present a problem mathematically, the exponential function is a transcendental function that tends to be slow when evaluated computationally. For efficient transport codes, this presents a challenge. Previous works have demonstrated that function interpolation can provide significant run-time reduction [4], and the original formulation [1] suggested the use of function interpolation (though no details were provided).

5.1.1 First Approach: Improved Accuracy

With the implementation of LSA into MPACT, stability issues were observed in problems with very small transport cross sections, such as the fuel-clad gap in LWRs. These stability issues were only observed when exponential function interpolation was used, and the simplest method for addressing the issue was to increase the accuracy of the exponential interpolation. It was discovered that the root of the problem was the $F_2(\tau^g_{mki})$ function in the transmission equation

$$\psi^{g,\text{out}}_{mki} = \psi^{g,\text{in}}_{mki} + \left(\frac{\overline{q}^g_{mki}}{\Sigma^g_{t,i}} - \psi^{g,\text{in}}_{mki} \right) F_1(\tau^g_{mki}) + \frac{\widehat{q}^g_{mi}}{2\left(\Sigma^g_{t,i}\right)^2} F_2(\tau^g_{mki}). \tag{5.2}$$

In MPACT, source terms are actually computed and stored as $q/\Sigma^g_{t,i}$; however the $F_2(\tau^g_{mki})$ term has an additional inverse $\Sigma^g_{t,i}$. In problems with near-void regions, where $\Sigma^g_{t,i}$ is small, any error in $F_2(\tau^g_{mki})$ interpolation will be magnified. The simplest approach is to increase the accuracy of the exponential interpolation to account for the lowest expected cross sections; in the test problem this was on the order of 10^{-5}. Thus, the expectation is that an interpolation 5 orders of magnitude more accurate than previous accuracy would be sufficient. Previous work [4] indicated that for FSMoC calculations an max interpolation error of 10^{-7} was sufficient, i.e. for LSMoC the max error would be within 10^{-12}.

Creating interpolation tables with the necessary accuracy for these problems requires some care.

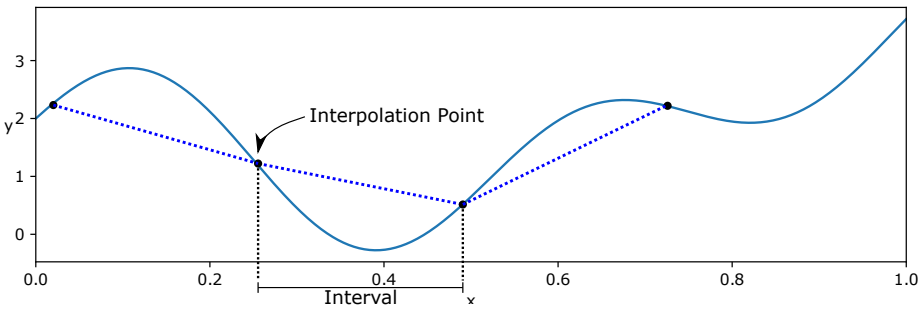

Figure 5.2: Example of linear interpolation with uniform interval widths and interpolation points on the edge of the domain.

The original investigation of exponential interpolation for transport calculations done by Yamamoto et al. [4] indicated two methods of controlling interpolation accuracy. One method to increase interpolation accuracy is to increase the number of intervals (decreased interval width); however, this increased the memory. Alternatively, higher order polynomials can be used in the interpolation, which overall tends to reduce memory at the expense of increased run-times.

In this investigation, two additional methods for controlling accuracy were investigated: interpolation node choice, and non-uniform interval widths.

5.1.1.1 Interpolation Points

Within each interval of an interpolation table, the function is computed at interpolation points and an approximation of the function is made as the polynomial passing through these points. The placement of these points within each interval can greatly affect the accuracy of the approximation. Previous works [4, 5] used evenly spaced interpolation points within each interval; however, this does not minimize the error in the approximation. An example is shown in Fig. 5.2.

Let $P_n(x)$ be the order n polynomial approximating a function, $f(x)$, on an arbitrary interval $[a, b]$. The maximum error, ϵ, within an interval is given by

$$\epsilon = \frac{1}{(n+1)!} \left(\max_{\xi \in [a,b]} \left| f^{(n+1)}(\xi) \right| \right) \left(\max_{x \in [a,b]} \left| \prod_{j=1}^{n+1} (x - x_j) \right| \right), \tag{5.3}$$

for some value $\xi \in [a, b]$, where $f^{(n+1)}$ is the $n+1$-th derivative of $f(x)$. The choice of interpolation points will only affect the last term enclosed in parentheses.

The Chebyshev points [6] are a set of values in $[a, b]$ that minimize $\max_{x \in [a,b]} \left| \prod_{j=1}^{n+1} (x - x_j) \right|$, and

Table 5.1: Maximum error in $F_1(\tau_m^g)$ for interval width Δ.

Polynomial Order	Uniform points	Chebyshev points
1	$\frac{\Delta^2}{8}$	$\frac{\Delta^2}{16}$
2	$\frac{\Delta^3}{72\sqrt{3}}$	$\frac{\Delta^3}{192}$
3	$\frac{\Delta^4}{1536}$	$\frac{\Delta^4}{3072}$

are given by

$$x_k = \frac{1}{2}\left[(a+b) + (b-1)\cos\left(\frac{2k-1}{2(n+1)}\pi\right)\right], \forall k \in \{1, 2, ..., n, n+1\}. \tag{5.4}$$

By using the Chebyshev points, the maximum interpolation error, ϵ, can be simplified to

$$\epsilon = \frac{1}{2^n(n+1)!}\left(\frac{b-a}{2}\right)^{n+1} \max_{\xi\in[a,b]} \left|f^{(n+1)}(\xi)\right|. \tag{5.5}$$

Because the Chebyshev points do not include the end-points of the interval, there is additional cost in setting up the interpolation table, but this is negligible to typical MoC calculation times. An interpolation table using Chebyshev points *reduces error at no run-time cost* compared to a table using evenly spaced points. For this reason, Chebyshev points will be assumed for the remainder of this section. Table 5.1 shows maximum errors for $F_1(\tau_m^g)$ interpolation for uniformly spaced points and Chebyshev points for an interval width $\Delta = b - a$.

5.1.1.2 Interval Width

The conventional approach for interpolation tables has been to use a constant interval width, Δ, for all intervals in the domain. This interval width is then used to control the error of the table. Equation (5.3) shows that the interval bounds affect the interpolation error through the derivative term. The second and higher order derivatives of each of the exponential functions (Eqs. (5.1)) approach zero as τ_{mki}^g approaches infinity. This indicates that the interpolation error typically decreases as the optical thickness increases in the conventional approach.

However, is is possible to maintain the same maximum error over each interval if a variable interval width, Δ_i, is used, where i indicates the interval index. By using a variable interval width, a table can use fewer intervals while maintaining the same maximum error. However, since the widths are no longer constant, there is no longer a simple/direct conversion from τ_{mki}^g to i. Although there may be better ways, for this work the smallest interval is used to break up the domain into a map which points to the correct interval for that range of values.

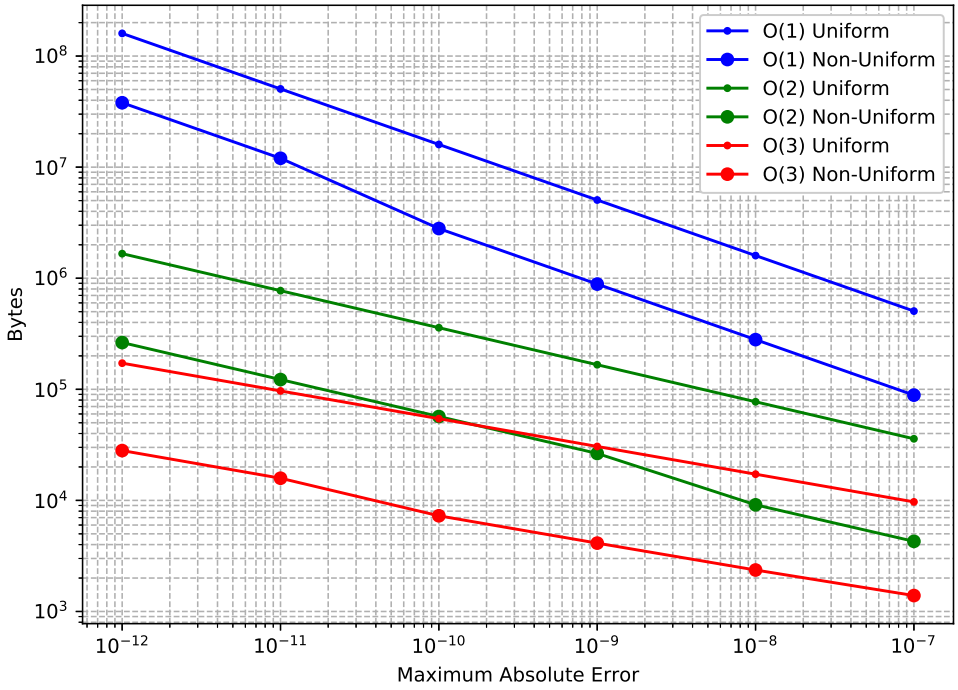

Figure 5.3: The memory usage of a single interpolation table (polar independent) for $F_1(\tau^g_{mki})$ is shown as a function of the maximum error for different interpolation orders and tabulation methods.

It was found that the use of non-uniform interval widths allowed for significantly fewer total intervals, reducing the memory usage, but incurring overhead for the additional mapping to index. Figure 5.3 shows the memory usage for a polar-independent interpolation table for $F_1(\tau^g_{mki})$. Using a non-uniform table typically decreases the memory usage by nearly an order of magnitude. For polar-dependent tables, the memory usage will be multiplied by the largest inverse sine of the polar angle, and the number of polar angles.

Because all the functions of Eqs. (5.1) are related, it is possible to tabulate only a single function and compute the others from the resulting interpolated value. However, if $F_1(\tau^g_{mki})$ is known accurately, it is not possible to compute $H(\tau^g_{mki})$ for very small τ^g_{mki} due to round-off errors. Instead one can tabulate $H(\tau^g_{mki})$ and use the result to compute the other functions; however, this may incur more error than directly interpolating these functions.

5.1.2 Function Modification

A second approach for addressing the instability due to inaccurate function interpolation was taken: change the functions. Recall that the highly accurate interpolation tables of Section 5.1.1 were

necessary due to the inverse total (or transport) cross section on the $F_2(\tau^g_{mki})$ term of Eq. (5.2). Manipulating this term, we define a new function

$$\frac{F_2(\tau^g_{mki})}{\Sigma^g_{t,i}} = t_m \widehat{F}_2(\tau^g_{mki}), \tag{5.6}$$

where

$$\widehat{F}_2(\tau^g_{mki}) \equiv 2\left(1 - \frac{F_1(\tau^g_{mki})}{\tau^g_{mki}}\right) - F_1(\tau^g_{mki}). \tag{5.7}$$

The $\widehat{F}_2(\tau^g_{mki})$ function can be tabulated in place of $F_2(\tau^g_{mki})$; this will require an additional multiplication by the segment length t_{mki} causing slight reduction in performance. But, by using the modified $\widehat{F}_2(\tau^g_{mki})$ function, the underlying cause of the numerical instability is addressed, and the more accurate interpolation is no longer necessary.

One approach is to tabulate the $\widehat{F}_2(\tau^g_{mki})$ function in place of the $F_2(\tau^g_{mki})$ function, and multiply by t_{mki} during evaluation. However, as stated in the previous section, it is possible to tabulate a single function and compute the others. The $H(\tau^g_{mki})$ function could be tabulated again; but tabulating an intermediate function,

$$E_1(\tau^g_{mki}) \equiv \frac{1 - e^{-\tau^g_{mki}}}{\tau^g_{mki}}, \tag{5.8}$$

uses the same number of operations to compute the other functions. This $E_1(\tau^g_{mki})$ function also has smaller derivative terms around $\tau^g_{mki} = 0$, allowing for larger interval widths with no loss in accuracy. Therefore, it is expected that $E_1(\tau^g_{mki})$ tabulation will be more efficient.

5.1.3 Results

The results of this section were generated in serial on a Linux system with an Intel Xeon E3-1241 v3 (3.50 GHz) processors with 8 MB L3 cache. Results were generated for a 2-D MoC transport calculation. In 2-D it is sometimes convenient to store separate interpolation tables for each polar angle. Both polar dependent and independent tables were tested.

In both of the results sections, results were generated using tables for the three functions ($F_1(\tau^g_{mki})$, $F_2(\tau^g_{mki})$, $H(\tau^g_{mki})$), or a single function (which is then used to compute the others). In the results, it is considered 3 functions, as the $G_1(\tau^g_{mki})$, and $G_2(\tau^g_{mki})$ functions are only used in pre-computing coefficients, and not in the main MoC solver routine.

5.1.3.1 Results using More Accurate Tables

Table 5.2 shows results for the different interpolation methods in a 2-D MoC calculation. The use of non-uniform intervals significantly reduced the memory usage, but the run-times generally increased. This is likely due to the overhead from the additional index mapping operation; it is possible that a more efficient index mapping would change these results.

The linear tables were significantly slower than higher-order interpolations, and the non-uniform linear tables were actually slower than just using the builtin transcendental functions. The poor performance is due to the main memory accesses caused by the table size exceeding the largest (L3) cache size. The polar independent tables were faster only in the case of the linear tables, due primarily to the reduction in memory. In all other cases the polar-dependent tables were able to more efficiently approximate the functions. Using either second or third order tables gave reasonably low run-times; compared to the analytic evaluations the order 2 uniform polar dependent table led to ~ 3.5x speed-up in the exponential time, and ~ 1.9x speed-up in the overall MoC run-time. The results for both second and third order interpolation tables did not vary significantly, the second order was slightly faster for uniform tables.

However, if a single function is tabulated and used to compute the others, the memory footprint of the interpolation tables can be significantly reduced. Moreover, the memory accesses are reduced in favor of floating point operations which increases the computational intensity and temporal cache locality of the implementation. Generally, this is a favorable strategy for improving code performance as a memory access is expected to take *at minimum* the same time as a single floating point operation (FLOP), with cache-misses increasing that time. Indeed, Table 5.2 shows that tabulating the single function reduced run-time in all cases.

5.1.3.2 Results using Modified Function

Results were generated for the same cases as the more accurate table, but the interpolation accuracy was 10^{-7} rather than 10^{-12}, as the function modification addressed the cause of the instability. The results are summarized in Table 5.3. In one approach the three functions are tabulated, in the other $E_1(\tau^g_{mki})$ is tabulated and used to compute the three functions. Previous results showed that the polar-independent and non-uniform interval width tables were slower than uniform polar-dependent tables; here the results are only shown for the uniform polar-dependent interpolation tables.

The interpolation accuracy is not required to be as high as in the previous cases, thus the tables are significantly smaller in memory size. The linear tables no longer exceed the L3 cache size and are not prohibitively slow to use. In fact, the linear tables are the fastest option for both 3-table and single-table interpolation methods. Interpolating $E_1(\tau^g_{mki})$ and computing the other functions from the result was the fastest approach overall. As before, this is expected because this method favors

Table 5.2: Results for different exponential function evaluation methods. Maximum interpolation error of 10^{-12}. "w/ pol" indicates a table with polar dependence, and "w/o pol" indicates a table without polar dependence.

Method	Table Type	Order	Exponential Time (s)		MoC Time (s)		Intervals (Memory)	
			w/ pol	w/o pol	w/ pol	w/o pol	w/ pol	w/o pol
Analytic	N/A	N/A	432.5		654.7		N/A	
3-Functions	Uniform	1	382.6	360.3	622.5	591.0	6.00E7 (8.04 GB)	1.00E7 (458 MB)
		2	121.3	151.7	343.2	372.1	416080 (85.7 MB)	69360 (4.8 MB)
		3	124.1	169.0	347.5	388.7	32280 (9079 KB)	5400 (506 KB)
	Non-Uniform	1	592.9	559.2	825.8	800.6	4.07E6 (878 MB)	840658 (76.6 MB)
		2	144.6	178.5	364.3	397.8	45265 (10.9 MB)	8020 (835 KB)
		3	139.6	199.8	358.5	420.0	4491 (1.4 MB)	796 (85.2 KB)
1-Function	Uniform	1	296.2	259.3	523.9	484.5	6.00E7 (2.68 GB)	1.00E7 (153 MB)
		2	91.4	123.2	310.2	345.7	416080 (28.6 MB)	69360 (1.59 MB)
		3	87.2	133.2	305.4	353.6	32280 (2.96 MB)	5400 (169 KB)
	Non-Uniform	1	474.6	424.0	714.6	653.9	4.07E6 (415 MB)	722899 (49.2 MB)
		2	105.8	146.4	326.6	367.7	41444 (4.4 MB)	7338 (443 KB)
		3	98.9	153.3	318.8	373.2	4152 (515 KB)	735 (33.5 KB)

FLOPs over memory accesses.

This approach also significantly reduces the number of intervals necessary (by about 3 orders of magnitude). Although the higher-order interpolation ended up not being more efficient than the linear interpolation tables, the number of intervals is extremely small. These methods may be useful on different architectures (such as GPGPUs[1]) where memory is more limited than on a single-threaded CPU calculation.

Table 5.3: Results using the modified $\widehat{F}_2(\tau^g_{mki})$ function, with maximum interpolation error of 10^{-7}. Memory is under 1 MB in all cases.

Method	Order	Exp. Time (s)	MoC Time (s)	# Intervals
3-Functions	1	88.4	307.9	4774
	2	99.7	316.8	225
	3	116.5	333.1	46
$E_1(\tau^g_m)$ Only	1	80.5	299.0	2739
	2	87.6	307.3	158
	3	99.0	317.7	38

[1]this statement was not confirmed as part of this study, and is speculation based on knowledge of architecture constraints.

5.1.4 Conclusions

This study focused on the investigation of efficient approximation of the exponential functions in the LSMoC. Methods for efficiently approximating the exponential function for FSMoC have previously been investigated. However, these methods, applied without modification to the LSMoC can lead to numerical instability in problems with near-void regions. One approach to deal with these instabilities is to improve the accuracy of the interpolation tables based on the lowest cross section in the problem. While this approach can be made efficient, if cross sections become too small the tables may become exceedingly large and significantly hamper performance.

This investigation revealed that the cause of the instability was the $F_2(\tau^g_{mki})$ function in the transmission equation. By instead manipulating the term including this function, the cause of the instabilities can be addressed. This approach no longer requires excessively large interpolation tables; however, some key-findings from the first approach can be applied to make this appraoch faster. First, the use of Chebyshev points significantly increases interpolation accuracy for the same number of intervals as uniformly spaced points, at no run-time cost. Additionally, by interpolating a single function and using the result to compute the other functions performance can be significantly improved.

5.2 Improved Linear Source Formulation for Multi-physics and 2D/1D Applications

As stated in Section 3.3, the original derivation of the moment-based linear-source approximation (LSA) from Ferrer and Rhodes [1] faced inefficiencies in problems with non-constant cross sections. The inefficiencies arose from the use of pre-computed coefficients, Eq. (3.53), which must be re-computed if cross sections change. In multiphysics calculations, such as with T/H feedback, cross sections typically change each iteration, leading to significant overhead from re-computing these terms. This section presents and equivalent formulation, which eliminates the need to re-compute these terms if cross sections change, without additional operations.

5.2.1 Derivation

The derivation of this improved formulation begins with the same initial steps as the derivation detailed in Section 3.3.2. Several of these equations are repeated in this section for clarity. The source is assumed to have a spatially linear shape

$$q^g_{mi}(\boldsymbol{x}) \approx q^g_{mi} + \boldsymbol{x} \cdot \underline{\widehat{\boldsymbol{q}}}^g_{mi}, \tag{5.9}$$

and the angular flux moments can be expanded similarly

$$\phi_{i,n}^{\ell,g}(\boldsymbol{x}) = \overline{\phi}_{i,n}^{\ell,g} + \boldsymbol{x} \cdot \underline{\widehat{\boldsymbol{\phi}}}_{i,n}^{\ell,g}. \tag{5.10}$$

The source can be computed from the flux moments using Eq. (3.36).

Computing the source requires the flux to be evaluated during transport sweeping. The angular flux moments are given by Eqs. (3.41), but are repeated here for clarity. The spatially flat angular flux moments are defined by integrating the flux multiplied by a spherical harmonics moment function over space and directions,

$$\overline{\phi}_{i,n}^{\ell,g} \equiv \left\langle R_\ell^n(\widehat{\boldsymbol{\Omega}})\psi^g \right\rangle_i = \frac{4\pi}{V_i} \sum_m w_m R_\ell^n(\widehat{\boldsymbol{\Omega}}_m) \sum_k \delta A_{mki} t_{mki} \langle \psi^g \rangle_{mki}. \tag{5.11a}$$

To determine the spatial expansion coefficients of the flux moments, Eq. (5.10) is operated on by $\left\langle R_\ell^n(\widehat{\boldsymbol{\Omega}})\boldsymbol{x}(\cdot) \right\rangle_i$. As before, this should be directly proportional to the angular flux operated on by $\left\langle R_\ell^n(\widehat{\boldsymbol{\Omega}})\boldsymbol{x}\psi^g \right\rangle_i$, a system of equations is found

$$\boldsymbol{M}_i \underline{\widehat{\boldsymbol{\phi}}}_{i,n}^{\ell,g} = \left\langle R_\ell^n(\widehat{\boldsymbol{\Omega}})\boldsymbol{x}\psi^g \right\rangle_i, \tag{5.11b}$$

where

$$\boldsymbol{M}_i \equiv \left\langle \boldsymbol{x}^T \boldsymbol{x} \right\rangle_i. \tag{5.11c}$$

The spatial angular flux moments, $\left\langle R_\ell^n(\widehat{\boldsymbol{\Omega}})\boldsymbol{x}\psi^g \right\rangle_i$, are then defined as

$$\left\langle R_\ell^n(\widehat{\boldsymbol{\Omega}})\boldsymbol{x}\psi^g \right\rangle_i = \frac{4\pi}{V_i} \sum_m w_m R_\ell^n(\widehat{\boldsymbol{\Omega}}_m) \sum_k \delta A_{mki} t_{mki} \left(\boldsymbol{x}_{mki}^{\text{in}} \langle \psi^g \rangle_{mki} + \widehat{\boldsymbol{\Omega}}_m \langle t_m \psi^g \rangle_{mki} / \xi_{mi} \right). \tag{5.11d}$$

With the assumed source shape, Eq. (5.9), the characteristic transport equation becomes The characteristic transport equation becomes

$$\left[\frac{\mathrm{d}}{\mathrm{d}t_m} + \Sigma_{t,i}^g \right] \psi_{mki}^g(s) = \overline{q}_{mki}^g + \widehat{q}_{mi}^g \left(t_m - \frac{t_{mki}}{2} \right), \tag{5.12a}$$

where

$$\overline{q}_{mki}^g \equiv \frac{1}{4\pi} \left[q_{mi}^g + \boldsymbol{x}_{mki}^{\text{c}} \cdot \underline{\widehat{\boldsymbol{q}}}_{mi}^g \right], \tag{5.12b}$$

$$\widehat{q}_{mi}^g \equiv \frac{1}{4\pi} \left[\frac{\widehat{\boldsymbol{\Omega}}_m \cdot \underline{\widehat{\boldsymbol{q}}}_{mi}^g}{\xi_{mi}} \right], \tag{5.12c}$$

and $\boldsymbol{x}_{mki}^{\text{c}}$ is the local-coordinate centroid of the track-segment. Substituting this assumed source

shape (linear) into the generic MoC solution, given by Eq. (3.9), the angular flux along a track-segment is found to be

$$\psi_{mki}^{g}(s) = \psi_{mki}^{g,\text{in}} + \left(\frac{\overline{q}_{mki}^{g}}{\Sigma_{t,i}^{g}} - \psi_{mki}^{g,\text{in}} \right) F_1(\tau_m^g) + \frac{\widehat{q}_{mi}^{g}}{2(\Sigma_{t,i}^{g})^2} F_2(\tau_m^g), \tag{5.13a}$$

where

$$F_1(\tau_m^g) \equiv 1 - \exp(-\tau_m^g), \tag{5.13b}$$

and

$$F_2(\tau_m^g) \equiv 2[\tau_m^g - F_1(\tau_m^g)] - \tau_{mki}^g F_1(\tau_m^g). \tag{5.13c}$$

To evaluate the moments defined in Eqs. (5.11), the track-average flux and first spatial moment of the angular flux must be determined. The track-average flux is determined as it was before, by operating on Eq. (5.12a) by $t_{mki}\langle(\cdot)\rangle_{mki}$, yielding

$$\langle \psi^g \rangle_{mki} = \frac{\overline{q}_{mki}^{g}}{\Sigma_{t,i}^{g}} + \frac{\Delta\psi_{mki}^{g}}{\tau_{mki}^{g}}. \tag{5.14a}$$

At this point the two derivations diverge from one another. In the previous formulation, the integral in $\langle t_m \psi^g \rangle_{mki}$ is *explicitly* evaluated by substituting in the solution of the angular flux along the track (Eqs. (3.43)). Here, the moment will be found implicitly by operating on Eq. (5.12a) by $t_{mki}\langle t_m(\cdot)\rangle_{mki}$, just as was done for the 0th moment. This results in

$$\langle t_m \psi^g \rangle_{mki} = \frac{\langle \psi^g \rangle_{mki} - \psi_{mki}^{g,\text{out}}}{\Sigma_{t,i}^{g}} + \frac{t_{mki}}{2} \left[\frac{\overline{q}_{mki}^{g}}{\Sigma_{t,i}^{g}} + \frac{\widehat{q}_{mi}^{g}}{\Sigma_{t,i}^{g}} \frac{t_{mki}}{6} \right]. \tag{5.14b}$$

Unlike Eq. (3.44b), there a not any new exponential functions introduced in this form.

Previously, the average track flux, $\langle \psi^g \rangle_{mki}$, was expanded to find a simpler final form. This is the case here as well; however, the out-going flux, $\psi_{mki}^{g,\text{out}}$, will not be expanded, as this must necessarily be computed during transmission. Eqs. (5.11) can be simplified into

$$\overline{\phi}_{i,n}^{\ell,g} = \frac{4\pi}{V_i \Sigma_{t,i}^{g}} \sum_m w_m R_\ell^n(\widehat{\mathbf{\Omega}}) \sum_k \delta A_{mki} \left(t_{mki} \overline{q}_{mki}^{g} + \Delta\psi_{mki}^{g} \right), \tag{5.15a}$$

and

$$\left\langle R_\ell^n(\widehat{\boldsymbol{\Omega}})\boldsymbol{x}\psi^g\right\rangle_i = \frac{1}{V_i}\sum_m w_m R_\ell^n(\widehat{\boldsymbol{\Omega}})\sum_k \delta A_{mki} t_{mki}\left[\boldsymbol{x}_{mki}^{\mathrm{c}} q_i^g + \left(\boldsymbol{x}_{mki}^{\mathrm{c}}(\boldsymbol{x}_{mki}^{\mathrm{c}})^T + \frac{s_{mki}^2}{12}\widehat{\boldsymbol{\Omega}}_m\widehat{\boldsymbol{\Omega}}_m^T\right)\underline{\widehat{\boldsymbol{q}}}_i^g\right]$$
$$+\frac{4\pi}{V_i\Sigma_{t,i}^g}\sum_m w_m R_\ell^n(\widehat{\boldsymbol{\Omega}})\sum_k \delta A_{mki}\left[\boldsymbol{x}_{mki}^{\mathrm{in}}\Delta\psi_{mki}^g + \widehat{\boldsymbol{\Omega}}_m s_{mki}\left(\frac{\Delta\psi_{mki}^g}{\tau_{mki}^g} - \psi_{mki}^{g,\mathrm{out}} + \frac{\overline{q}_{mki}^g}{\Sigma_{t,i}^g}\right)\right] \tag{5.15b}$$

Equation (5.15b) contains $\Delta\psi_{mki}^g/\tau_{mki}^g$ terms, rather than only $\Delta\psi_{mki}^g$ terms. For numerical stability, it is beneficial to compute this quantity directly, rather than $\Delta\psi_{mki}^g$ and performing division. This can be found by evaluating the transmission equation, Eq. (5.13a), giving

$$\frac{\Delta\psi_{mki}^g}{\tau_{mki}^g} = \left(\psi_{mki}^{g,\mathrm{in}} - \frac{\overline{q}_{mki}^g}{\Sigma_{t,i}^g}\right)E_1(\tau_{mki}^g) - \frac{t_{mki}}{2}\frac{\widehat{q}_{mi}^g}{\Sigma_{t,i}^g}T_2(\tau_{mki}^g), \tag{5.16a}$$

where

$$E_1(\tau_{mki}^g) \equiv \frac{F_1(\tau_{mki}^g)}{\tau_{mki}^g}, \tag{5.16b}$$

$$T_2(\tau_{mki}^g) \equiv 2E_2(\tau_{mki}^g) - E_1(\tau_{mki}^g), \tag{5.16c}$$

and

$$E_2(\tau_{mki}^g) \equiv \frac{1 - E_1(\tau_{mki}^g)}{\tau_{mki}^g}. \tag{5.16d}$$

Here, $E_2(\tau_{mki}^g)$ is defined as an intermediate function which has smaller derivative terms, meaning higher accuracy with fewer interpolation intervals (see Section 5.1). Following the conclusions of Section 5.1, only the $E_2(\tau_{mki}^g)$ function needs to be tabulated, and then is used to compute the other two exponential functions, $E_1(\tau_{mki}^g)$, and $T_2(\tau_{mki}^g)$. The outgoing flux can then be evaluated as

$$\psi_{mki}^{g,\mathrm{out}} = \psi_{mki}^{g,\mathrm{in}} - \tau_{mki}^g\frac{\Delta\psi_{mki}^g}{\tau_{mki}^g}. \tag{5.17}$$

5.2.2 Particle Conservation

As described in Section 3.3.3, particle conservation puts the constraint of using direction-dependent renormalization and centroids, in addition to directional quadrature constraints. If these constraints are satisfied, Eqs. (5.15) can be simplified into

$$\overline{\phi}_{i,n}^{\ell,g} = \sum_m w_m R_\ell^n(\widehat{\boldsymbol{\Omega}})\frac{q_i^g}{\Sigma_{t,i}^g} + \frac{4\pi}{V_i\Sigma_{t,i}^g}\sum_m w_m R_\ell^n(\widehat{\boldsymbol{\Omega}})\sum_k \delta A_{mki}\Delta\psi_{mki}^g, \tag{5.18a}$$

and

$$\left\langle R_\ell^n(\widehat{\boldsymbol{\Omega}})\boldsymbol{x}\psi^g\right\rangle_i = \sum_m w_m R_\ell^n(\widehat{\boldsymbol{\Omega}})\boldsymbol{M}_{mi}\frac{\widehat{\boldsymbol{q}}_i^g}{\Sigma_{t,i}^g} + \frac{4\pi}{V_i\Sigma_{t,i}^g}\sum_m w_m R_\ell^n(\widehat{\boldsymbol{\Omega}})\sum_k \delta A_{mki}\left[\boldsymbol{x}_{mki}^{\text{in}}\Delta\psi_{mki}^g + \widehat{\boldsymbol{\Omega}}_m s_{mki}\left(\frac{\Delta\psi_{mki}^g}{\tau_{mki}^g} - \psi_{mki}^{g,\text{out}} + \frac{\overline{q}_{mki}^g}{\Sigma_{t,i}^g}\right)\right], \tag{5.18b}$$

where

$$\boldsymbol{M}_{mi} \equiv \frac{1}{V_i}\sum_k \delta A_{mki}\left[\boldsymbol{x}_{mki}^{\text{c}}(\boldsymbol{x}_{mki}^{\text{c}})^T + \frac{s_{mki}^2}{12}\widehat{\boldsymbol{\Omega}}_m\widehat{\boldsymbol{\Omega}}_m^T\right]. \tag{5.18c}$$

Although the above form seems to more computationally efficient, it would be negligent for this chapter to not include a more mathematically elegant form of Eq. (5.15b). The terms in the second summation may be rewritten as

$$\left\langle R_\ell^n(\widehat{\boldsymbol{\Omega}})\boldsymbol{x}\psi^g\right\rangle_i = \sum_m w_m R_\ell^n(\widehat{\boldsymbol{\Omega}})\boldsymbol{M}_{mi}\frac{\widehat{\boldsymbol{q}}_i^g}{\Sigma_{t,i}^g} + \frac{4\pi}{V_i}\sum_m w_m R_\ell^n(\widehat{\boldsymbol{\Omega}})\sum_k \delta A_{mki}\left[\boldsymbol{x}_{mki}^{\text{in}}\left(\psi_{mki}^{g,\text{in}} - \overline{\psi}_{mki}^g\right) - \boldsymbol{x}_{mki}^{\text{out}}\left(\psi_{mki}^{g,\text{out}} - \overline{\psi}_{mki}^g\right)\right], \tag{5.19a}$$

where $\overline{\psi}_{mki}^g$ is the average track flux,

$$\overline{\psi}_{mki}^g \equiv t_{mki}\langle\psi^g\rangle_{mki}. \tag{5.19b}$$

In this form, the interior summation over track-segments becomes a spatially weighted summation of the incident and outlet flux differences from the average flux.

5.2.3 Isotropic Simplifications

If the so called linear isotropic flat anisotropic (LIFA) scheme is used, the spatially flat moment equations do not change; however, Eq. (5.15b) can be simplified to

$$\left\langle R_\ell^n(\widehat{\boldsymbol{\Omega}})\boldsymbol{x}\psi^g\right\rangle_i = \boldsymbol{M}_i\frac{\widehat{\boldsymbol{q}}_i^g}{\Sigma_{t,i}^g} + \frac{4\pi}{V_i\Sigma_{t,i}^g}\sum_m w_m\sum_k \delta A_{mki}\left[\boldsymbol{x}_{mki}^{\text{in}}\Delta\psi_{mki}^g + \widehat{\boldsymbol{\Omega}}_m s_{mki}\left(\frac{\Delta\psi_{mki}^g}{\tau_{mki}^g} - \psi_{mki}^{g,\text{out}} + \frac{\overline{q}_{mki}^g}{\Sigma_{t,i}^g}\right)\right] \tag{5.20}$$

5.3 Results

5.3.1 C5G7 Benchmark

[C5G7 2-D Benchmark problem results]

5.3.2 Typical Pin Cell Depletion

In order to evaluate the benefits of this new formulation, the first multiphysics case studied was a typical uranium oxide (UO_2) fuel cell, as specified by Virtual Environment for Reactor Analysis (VERA) progression problem 1A [7]. Isotopic depletion calculations were run up to 70 gigawatt-days per metric ton heavy metal (GWDMT) ($\sim$1820 effective full power days (EFPD)) at hot full power (HFP) conditions. Using the current default meshing parameters in MPACT as a starting point, various mesh parameters were coarsened to study their affect when using the LSMoC. These cases were compared against a reference case which was very finely meshed with fine ray-spacing (0.001 cm), and a Tabuchi-Yamamoto [8] quadrature using 128 azimuthal angles and 4 polar angles over 4π All other cases were run using a Tabuchi-Yamamoto quadrature with 64 azimuthal angles and 4 polar angles, with a uniform ray-spacing of 0.05 cm.

Default Mesh MPACT's current default meshing parameters were used as a starting point. Flat and linear source calculations were run on this mesh, to set a baseline for "acceptable" levels of error in the eigenvalue. Compared to the reference case, the LS calculation had a larger maximum error in eigenvalue of 89.2 per cent mille (pcm), whereas the flat source (FS) calculation had a maximum error of 65.5 pcm. However, the average errors over the depletion were approximately the same: 31.6 and 33.7 pcm, for the FS and LS calculations, respectively. The eigenvalue differences over the depletion calculation are shown in Fig. 5.4. The goal in this mesh refinement study is to determine acceptable meshing parameters without worse maximum or average eigenvalue errors.

Fuel Radius During isotopic depletion, it is important to accurately capture the radial distribution of Plutonium, due to self-shielding effects. Plutonium is primarily produced in the outer rim of the pin, this is well known as the rim-effect. The default mesh uses three equal volume rings in the fuel region; however, we expect that two rings will be sufficient, when using the LSA, if the extra ring is placed in such a way that it captures this rim-effect. Experimental studies of the rim-effect [9] have found that there is a sharp rise in Plutonium at around between 80-90% of the outer radius of the fuel.

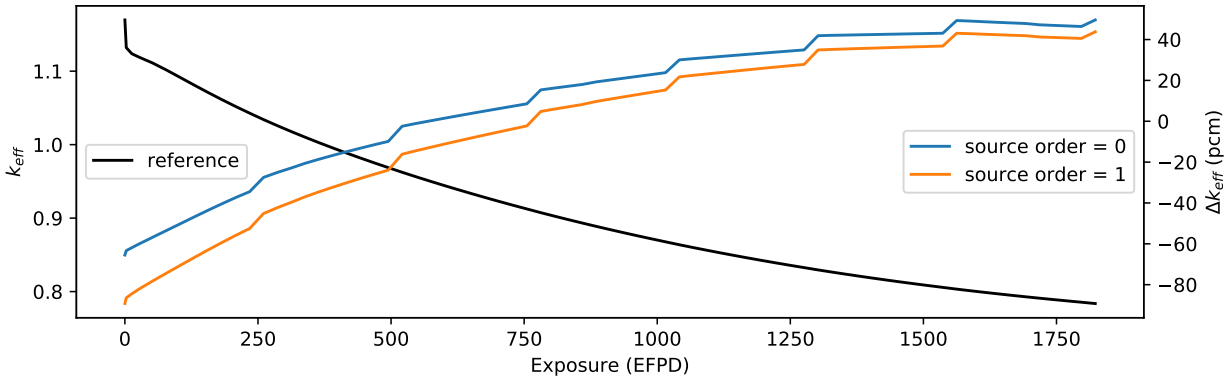

Figure 5.4: Reference eigenvalues and differences for the default mesh pin cell case with isotopic depletion.

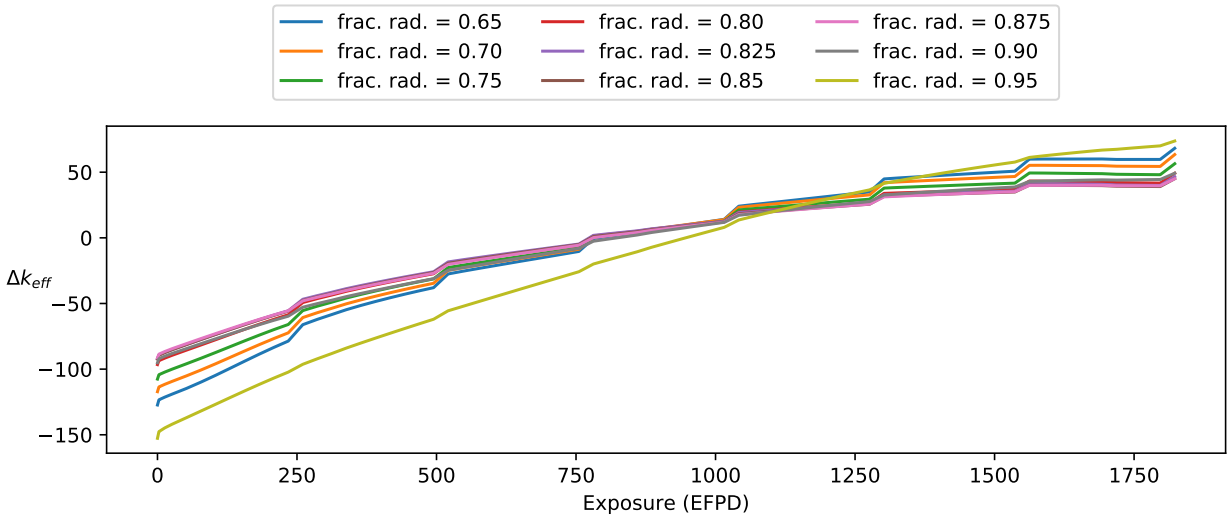

Figure 5.5: Eigenvalue comparisons for problem 1A using various inner fuel radii.

A series of calculations were run using two fuel rings with varying inner radius. The eigenvalue and Plutonium comparisons are shown in Figs. 5.5 and 5.6. Comparing eigenvalues, a fractional radius between 0.825 and 0.875 seem to have little effect on the mean or worst-case eigenvalue difference. By comparing the concentration of Pu-239, these radii are again shown to be the most accurate; a fractional radius of 0.875 was chosen to be sufficient, and used in the remainder of the studies.

Moderator Ring and Azimuthal Divisions The remaining mesh parameters are the azimuthal divisions in the fuel, clad, gap, and moderator regions, and the presence of an additional surrounding ring of moderator. While it may be sufficient to use a single azimuthal division in some regions in larger cases, due to symmetry of this single pin case, using a single azimuthal region would cause

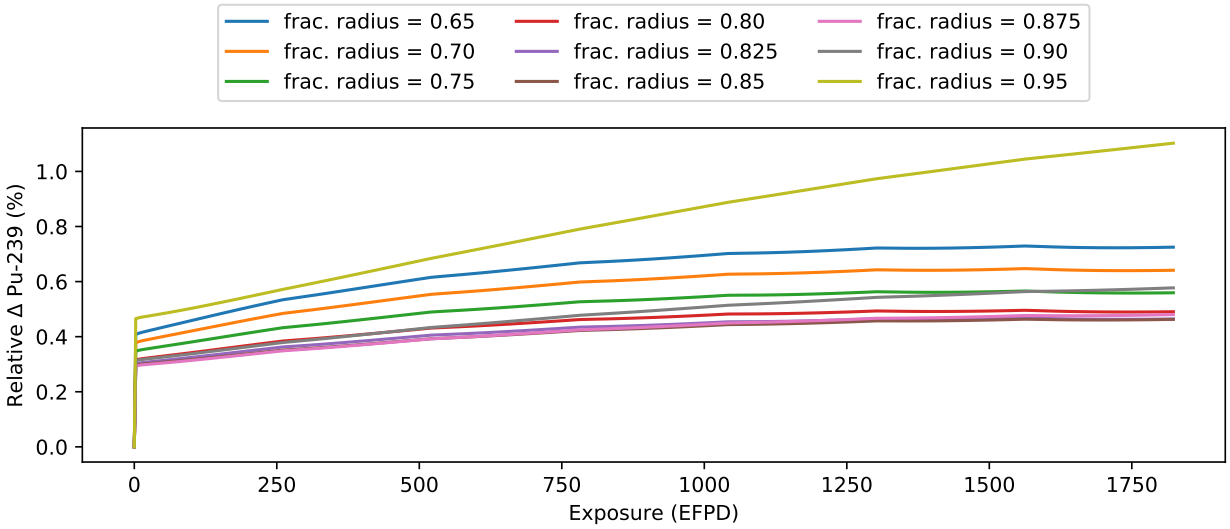

Figure 5.6: Pu-239 concentration comparisons for problem 1A using various inner fuel radii.

the linear components of the source to be zero (i.e. it is equivalent to the FSA). It was found that the coarsening of these parameters have an insignificant affect on the resulting eigenvalue when using the LSA, with less than 1 pcm difference over the entire depletion. Thus, four azimuthal divisions in each material region, and no additional surrounding moderator ring was found to be sufficiently accurate in this case. The coarse default and coarse meshes are displayed in Fig. 5.7.

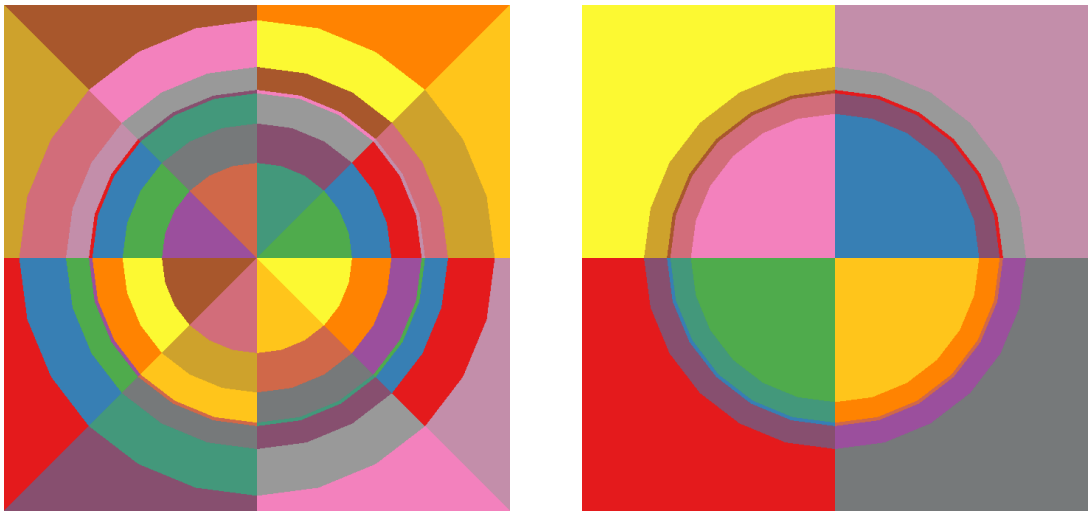

(a) default mesh (b) coarse mesh

Figure 5.7: VERA problem 1A (a) default and (b) coarse meshes.

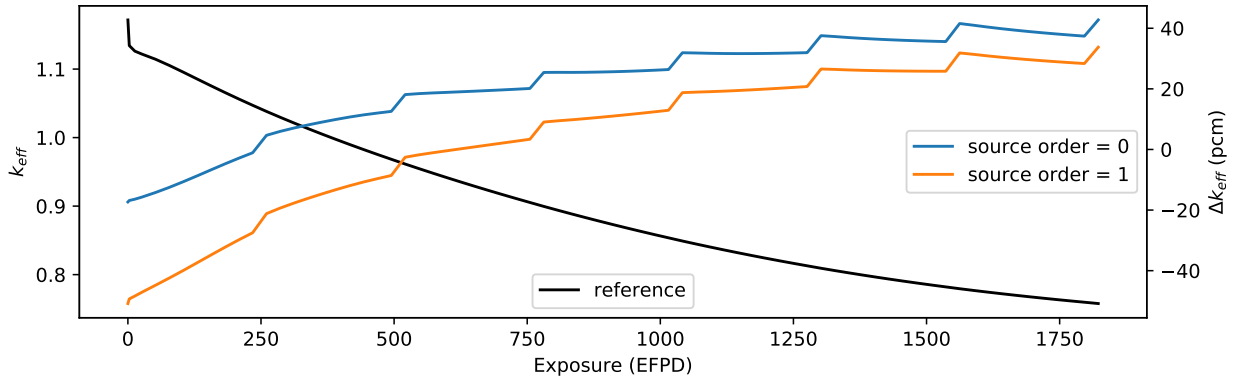

Figure 5.8: VERA Problem 2A default mesh eigenvalue comparison.

5.3.3 VERA Problem 2A and 2P Depletion

A mesh study similar to that done in Section 5.3.2 was performed on modified VERA problems 2A and 2P [7] with isotopic depletion up to 70 GWDMT. This was done to verify that the meshing parameters previously found were valid for larger problems, and determine if even coarser parameters were sufficient. First, problem 2A was studied; the meshing parameters of the fuel cell and guide-tube cells were studied independently.

5.3.3.1 Problem 2A

2A - Default Mesh For this problem, a reference calculation was carried out on the lattice with a very fine mesh. This reference calclation also used a finer directional quadrature of 128 azimuthal angles and 4 polar angles, with a uniform ray-spacing of 0.001 cm. Again, the MPACT's current default mesh was used a starting point for the mesh study; the results of the FS and LS calculations on this default mesh are used as a baseline. Eigenvalue and pin-power comparisons are provided in Figs. 5.8 and 5.9.

The trend in eigenvalue is similar to that found for problem 1A with the default mesh; the LS calculation has a higher absolute eigenvalue difference of 51 pcm compared to the FS calculation with 43 pcm. However, the average eigenvalue differences are similar at 24 and 21 pcm for the FS and LS calculations, respectively. Additionally, Fig. 5.9 shows that maximum pin power differences are consistently lower for the linear source calculation. This indicates that local effects are predicted better by the linear source, and there is some cancellation of errors occurring in the eigenvalue.

2A - Fuel Radius and Azimuthal Divisions For this problem, only the fractional radius found in Section 5.3.2 is tested against the current default mesh. There was no significant affect in eigenvalue or pin powers by using the 2-ring model with an inner radius fraction of 0.875. Next, the varied

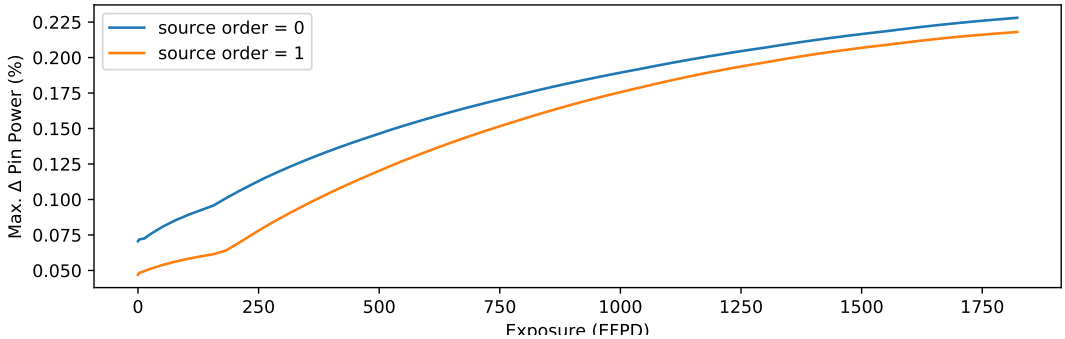

Figure 5.9: VERA Problem 2A default mesh pin power comparison.

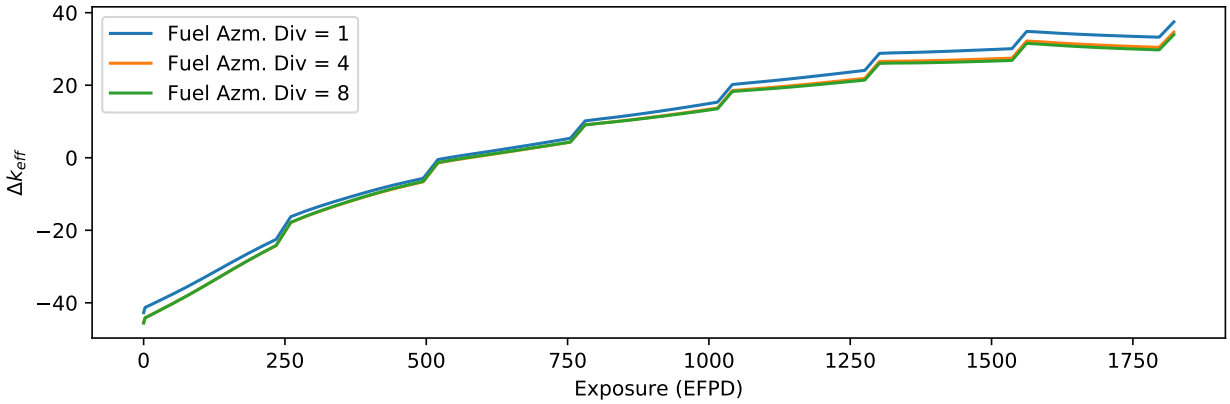

Figure 5.10: VERA Problem 2A eigenvalue comparison for varied fuel azimuthal divisions.

azimuthal divisions in the fuel were tested; this time testing a single azimuthal division. Figure 5.10 shows that there is noticeable affect moving to a single azimuthal division; however, the mean difference is changed by less than 1 pcm, and the max difference is actually improved by 3 pcm. We acknowledge that this improvement is likely due to cancellation of errors. Regardless, the net effect of this change is small.

2A - Moderator Azimuthal Divisions The azimuthal divisions of the surrounding moderator seems to have a more significant effect on the accuracy of the calculation. As shown by Fig. 5.11, using 4 azimuthal divisions seems to be sufficient; but moving to a single division is not feasible. A single division ore than doubles the mean eigenvalue difference, and shows a consistent positive bias.

2A - Cladding and Gap Azimuthal Divisions The azimuthal divisions of the cladding and gap regions do not seem to play a significant role. The difference is not even visually apparent in a graph of the eigenvalue, as seen in Fig. 5.12.

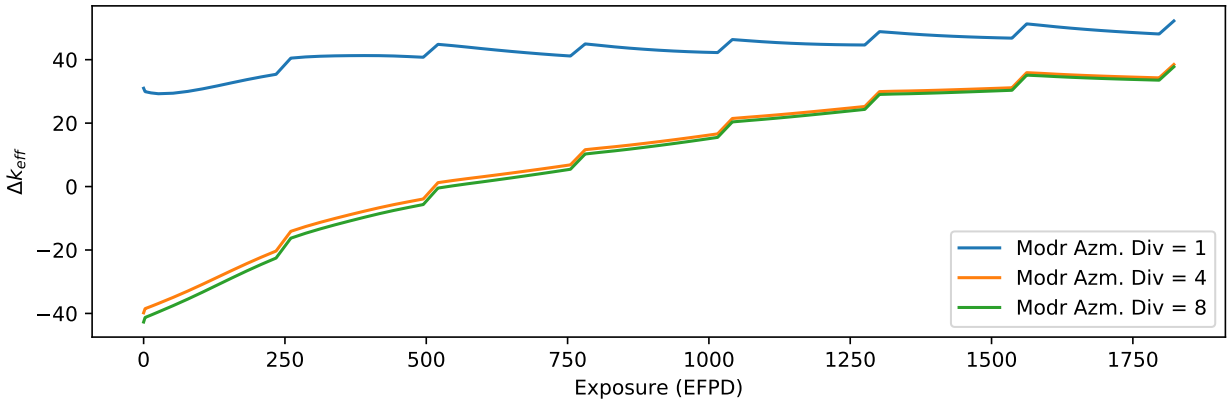

Figure 5.11: VERA Problem 2A eigenvalue comparison for varied number of surrounding moderator azimuthal divisions in the fuel cells.

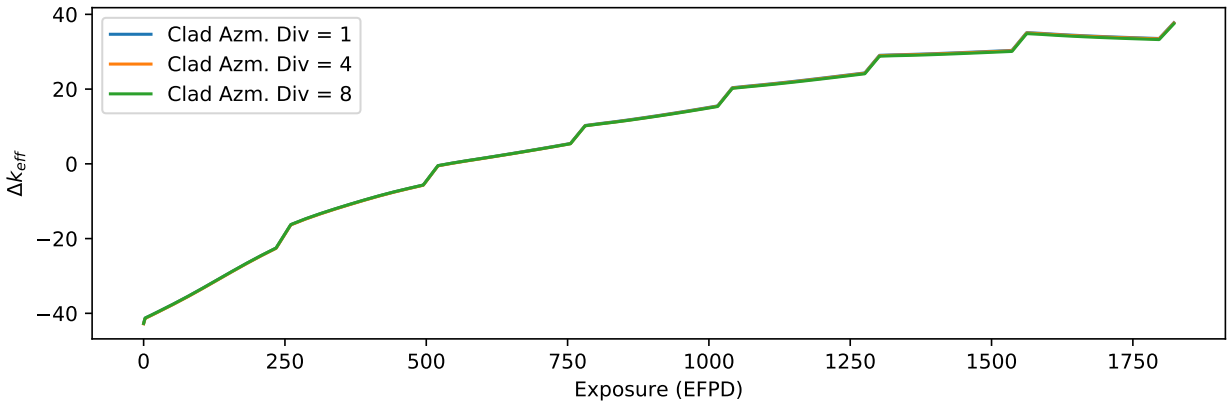

Figure 5.12: VERA Problem 2A eigenvalue comparison for varied number of the cladding/gap azimuthal divisions in the fuel cells.

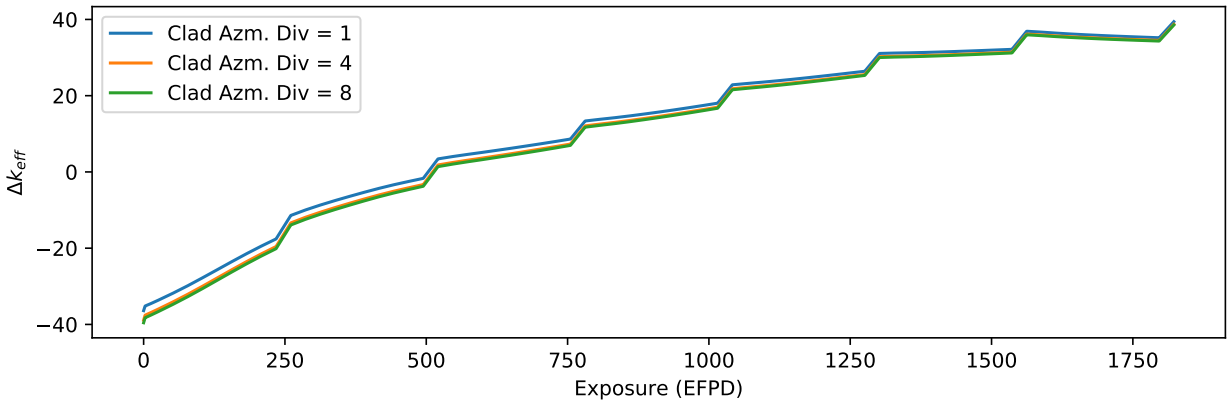

Figure 5.13: VERA Problem 2A eigenvalue comparison for varied number of inner moderator azimuthal divisions in the guide-tube cells.

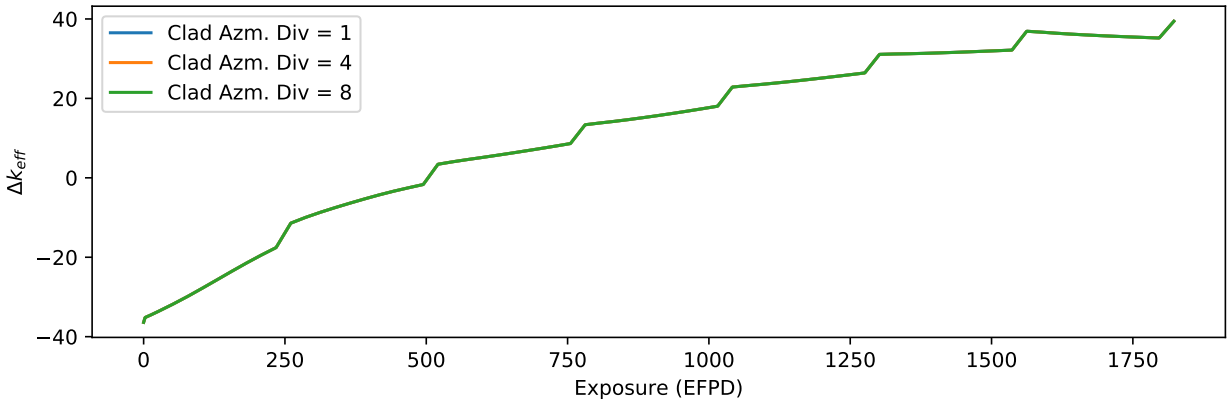

Figure 5.14: VERA Problem 2A eigenvalue comparison for varied number of cladding azimuthal divisions in the guide-tube cells.

2A - Guide-Tube Azimuthal Divisions In the 2A lattice, guide-tube pins are present; each guide-tube consists of three regions: inner moderator, cladding, and outer moderator. The effect of different azimuthal divisions in each of these regions was tested; the resulting eigenvalues are shown in Figs. 5.13 to 5.15. A single azimuthal division in each of these regions seems to be sufficient, without any significant affect on eigenvalue accuracy. However, 4 azimuthal divisions in the surrounding moderator was selected for moving forward due to compatibility issues with COBRA-TF (CTF).

2A - Coarse Mesh Summary Coarse mesh parameters were found using this isotopic depletion calculation on VERA problem 2A. The fuel cell

- has 2 fuel rings, with the inner radius being 0.875 fraction of the outer,
- no additional moderator ring in the surrounding moderator,

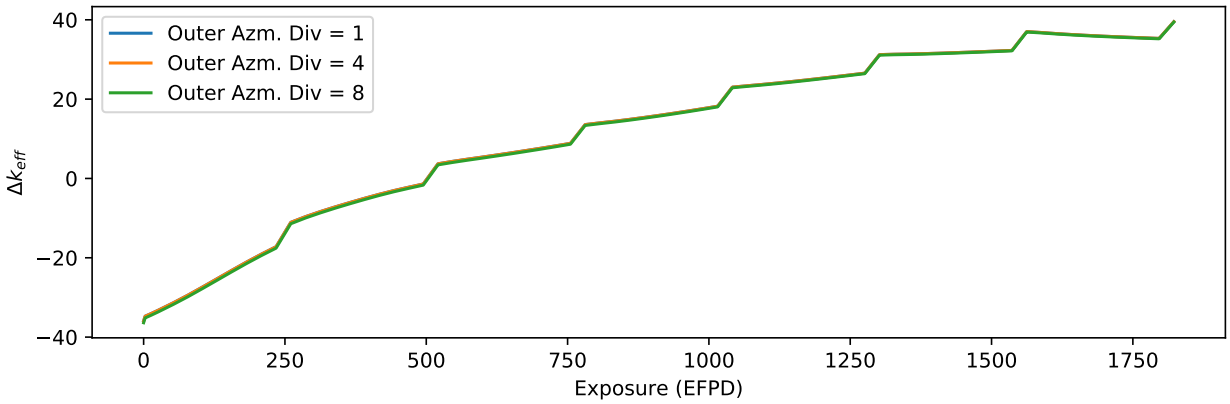

Figure 5.15: VERA Problem 2A eigenvalue comparison for varied number of outer moderator azimuthal divisions in the guide-tube cells.

- a single azimuthal division in the fuel, clad, and gap regions,
- and four azimuthal divisions in the surrounding moderator.

The guide-tube cell

- has no additional moderator ring in the surrounding moderator,
- has a single azimuthal division for the inner moderator, and cladding,
- and four azimuthal divisions for the surrounding moderator.

The lattice meshes are shown in Fig. 5.16.

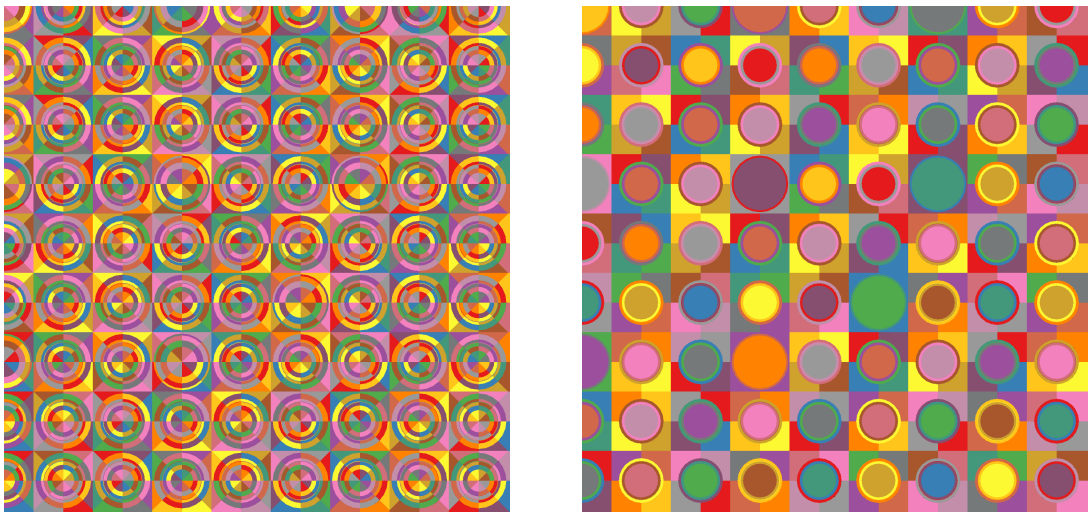

(a) default mesh (b) coarse mesh

Figure 5.16: VERA problem 2A (a) default and (b) coarse meshes.

Eigenvalue comparisons are shown in Fig. 5.17, and pin power comparisons are made in Fig. 5.18. While it is visually apparent that the accuracy is made slightly worse than the default mesh LS calculation, the entire goal of the this mesh study was to maintain error with the FS

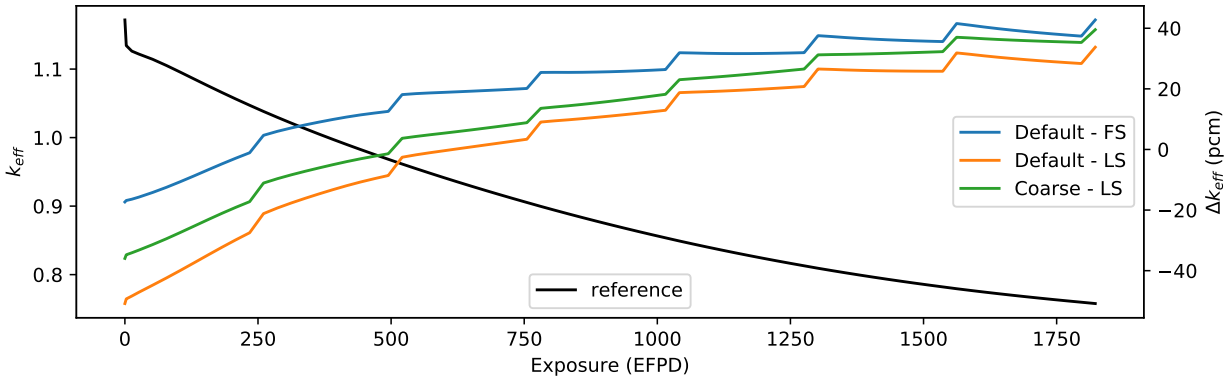

Figure 5.17: VERA Problem 2A coarse mesh eigenvalue comparison.

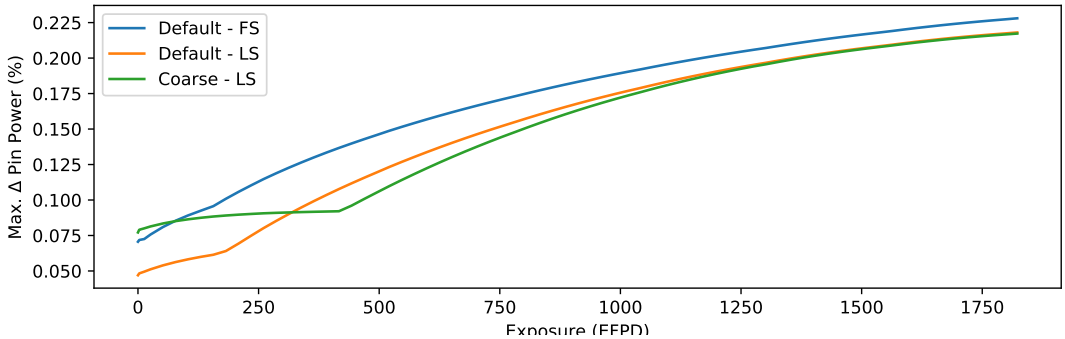

Figure 5.18: VERA Problem 2A coarse mesh pin power comparison.

calculation. This goal has been met, while reducing the number of cells from 3946 to 579.

5.3.3.2 Problem 2P

2P - Applying Coarse Mesh Parameters VERA problem 2P contains several gadolinia enriched fuel rods; as the lattice is depleted, these fuel rods "burn" the gadolinia. The gadolinia is primarily burned away started at the outer radius and moving inwards as time progresses. This inward burning makes the pins difficult to model, and requires many radial divisions for accurate calculations; it is effectively a "moving rim effect". Additionally, because the presence of these small radial regions, a finer ray-spacing (0.01 cm) is necessary.

To evaluate if the previously determined coarse mesh parameters are sufficient in this problem, they are applied to the regular fuel and guide-tube cells, while the gadolinia rods use the default meshing parameters. Figures 5.19 and 5.20 show that applying the coarse mesh parameters to the fuel and guide-tube cells does not significantly worsen the eigenvalue or pin power results. It is worth observing that errors in this cases are significantly higher than in the problem 2A; this is likely due to the complicated radial dependence of the gadolinia rods during depletion.

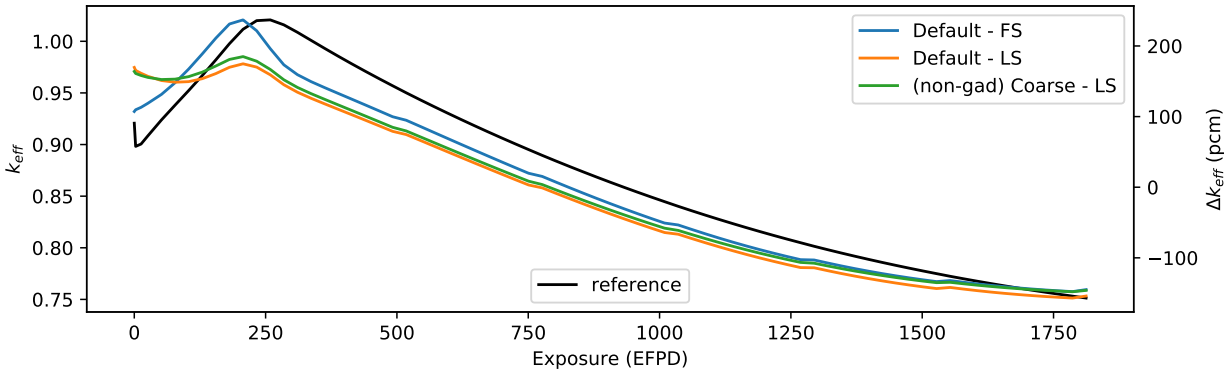

Figure 5.19: Eigenvalue comparisons for VERA problem 2P with default mesh parameters and coarse mesh parameters for the fuel and guide-tube cells.

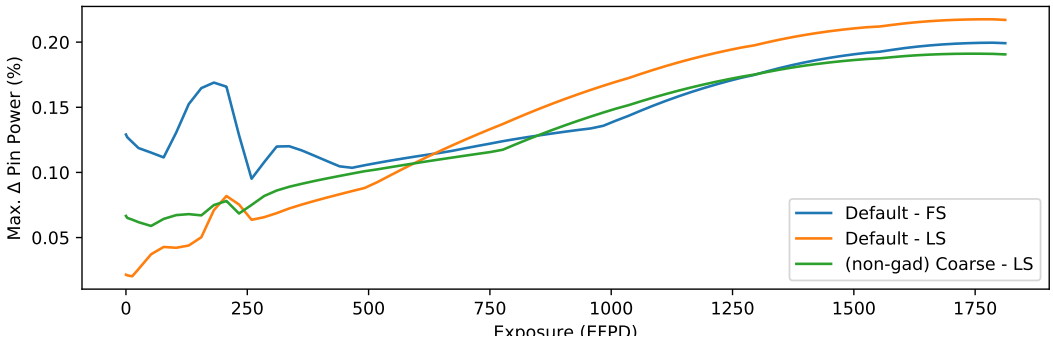

Figure 5.20: Pin power comparisons for VERA problem 2P with default mesh parameters and coarse mesh parameters for the fuel and guide-tube cells.

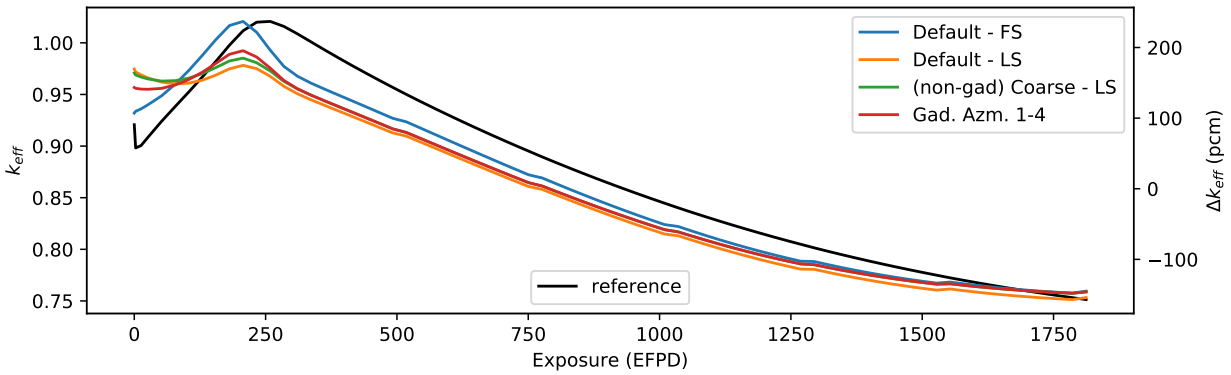

Figure 5.21: Eigenvalue comparisons for VERA problem 2P for the default mesh, previous coarse mesh, and gadolinia rods with fewer azimuthal divisions.

2P - Azimuthal Divisions It is not expected that the radial divisions in the gadolinia rods can be significantly coarsened. However, this is not true for the azimuthal divisions. We apply the same azimuthal divisions as we did for the fuel: 1 in the fuel, clad, and gap, and 4 in the surrounding moderator. Figure 5.21 shows the eigenvalue results are similar at all but the initial state to the previous coarse mesh parameters. Even at the initial state, the error is between the flat and linear source calculations on the default mesh. Thus, it is "acceptable" to coarsen the azimuthal divisions in the gadolinia pins.

2P - Radial Divisions While it is unexpected that significant radial coarsening can occur in these pins, it is best to test this assumption. Figure 5.22 shows the eigenvalue errors for several different numbers of equal volume radii in the gadolinia fuel rods. It is clear that the number of radii can significantly affect the accuracy. For 8 radial divisions, the error is higher near the reactivity peak, it is still between the flat and linear source calculation errors on the default mesh. The goal of these mesh reduction studies was not to preserve the accuracy of the linear source on the default mesh, but to nearly match the accuracy of the flat source calculation on the default mesh. For this goal, 8 radial divisions seems to be sufficient.

2P - Coarse Mesh Summary The coarse mesh parameters for the fuel and guide-tube cells previously found were also found to be sufficient for VERA problem 2P. For the gadolinia rods, it was found to be sufficient to

- have no additional moderator ring,
- use 8 equal volume fuel radial fuel divisions,
- a single azimuthal division in the fuel, clad, and gap regions,
- and four azimuthal divisions in the surrounding moderator.

Eigenvalue comparisons are shown in Fig. 5.24, and pin power comparisons are made in

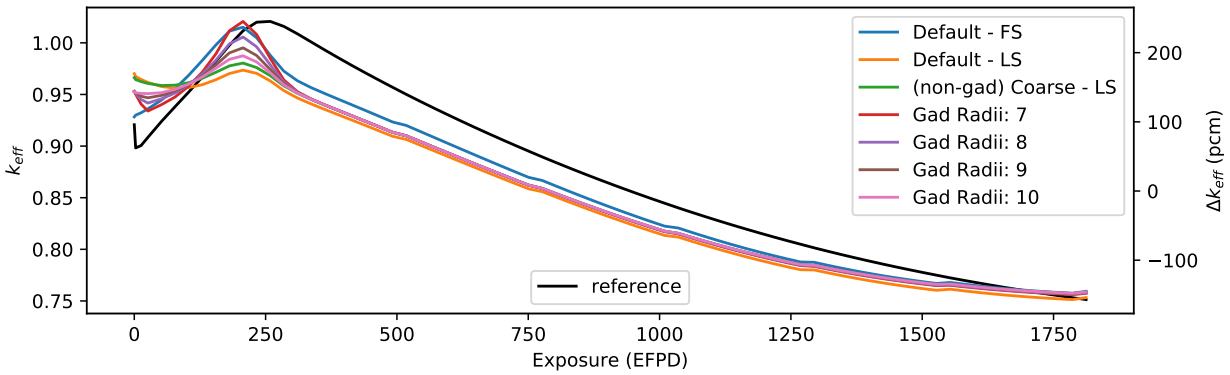

Figure 5.22: Eigenvalue comparisons for VERA problem 2P for varied number of radii in gadolinia rods.

Fig. 5.25. Using these coarse mesh parameters reduces the number of cells from 4282 to 621. The lattice meshes are visualized in Fig. 5.23.

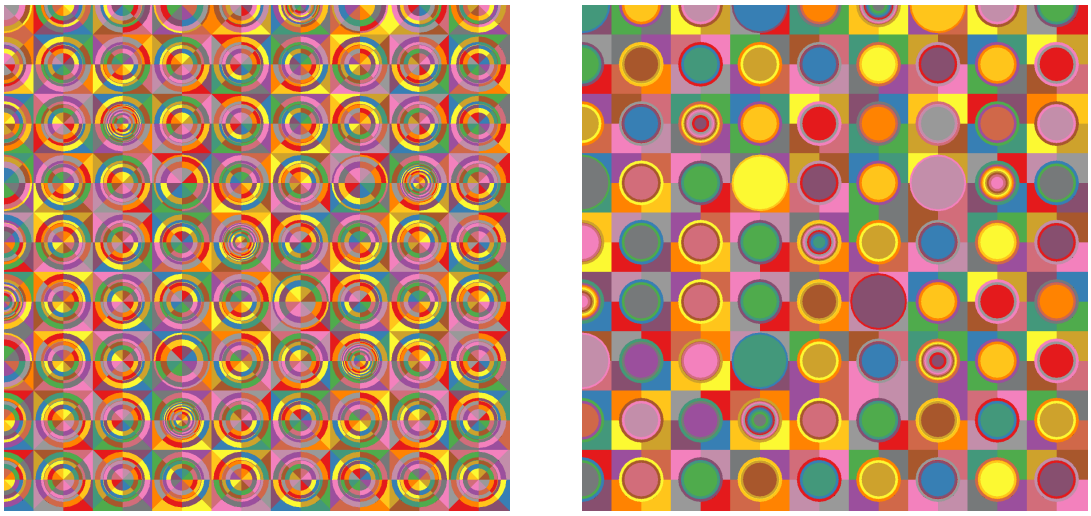

(a) default mesh (b) coarse mesh

Figure 5.23: VERA problem 2P (a) default and (b) coarse meshes.

5.3.3.3 Performance

[TIME/MEMORY RESULTS HERE]

5.3.4 2-D Lattices

In order to evaluate these coarse mesh parameters, they were applied to the VERA problem 2 lattice series. This series contains 17 common lattice configurations, and it is expected that if the meshing

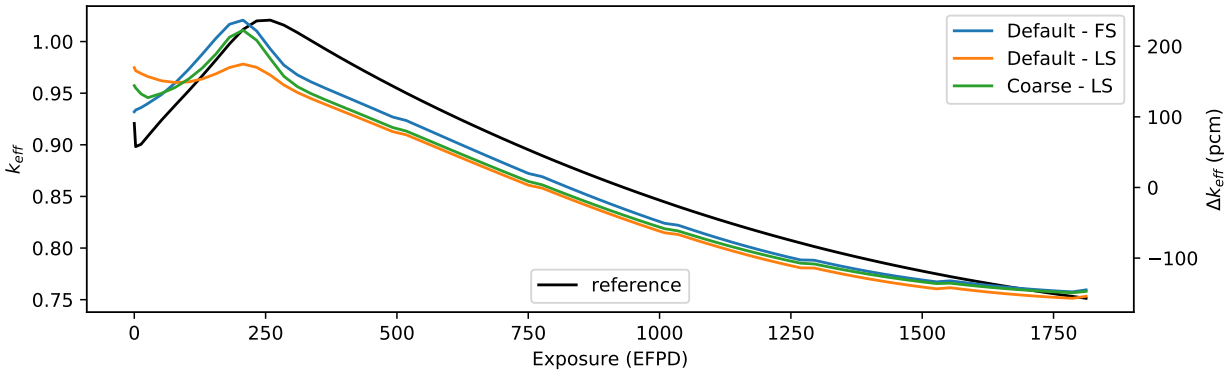

Figure 5.24: VERA Problem 2P coarse mesh eigenvalue comparison.

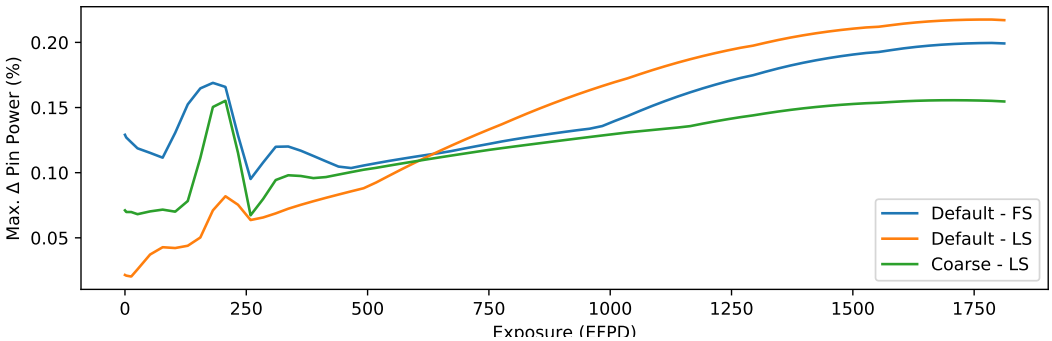

Figure 5.25: VERA Problem 2P coarse mesh pin power comparison.

Table 5.4: Results for VERA Problem 2 lattices for different mesh and source approximations.

Case	Δk_{eff} (pcm)				Max Pin Power Difference (%)			
	FS Default	LS Default	FS Coarse	LS Coarse	FS Default	LS Default	FS Coarse	LS Coarse
A	-17	-51	44	-36	0.07	0.05	0.24	0.08
B	-15	-49	46	-34	0.07	0.05	0.24	0.08
C	-17	-51	44	-36	0.07	0.05	0.24	0.08
D	-25	-59	39	-41	0.07	0.05	0.24	0.08
E	-49	-40	-52	-27	0.12	0.05	0.37	0.08
F	-74	-32	-120	-26	0.15	0.05	0.51	0.08
G	-98	-45	-210	-43	0.19	0.09	0.59	0.10
H	-78	17	-206	18	0.25	0.15	0.58	0.15
I	2	-43	82	-24	0.09	0.05	0.29	0.08
J	-74	-32	-119	-26	0.10	0.05	0.34	0.08
K	-61	-26	-97	-19	0.17	0.06	0.55	0.08
L	60	37	105	52	0.13	0.07	0.35	0.12
M	74	54	124	71	0.11	0.06	0.26	0.11
N	-1	31	-45	43	0.18	0.05	0.51	0.11
O	-21	9	-109	7	0.15	0.06	0.43	0.08
P	-115	-42	-311	-64	0.17	0.08	0.69	0.14
Q	-12	-48	54	-30	0.08	0.05	0.28	0.08
AVG	47	39	106	35	0.13	0.06	0.39	0.09
MAX	115	59	311	71	0.25	0.15	0.69	0.15

parameters are sufficient for these cases, they will be sufficient in most applications. The eigenvalue and pin-power results compared to a very finely meshed reference case are shown in Table 5.4. On average, the LS on the coarse mesh, using the parameters found in the previous sections, had accuracy comparable to the FS on the default mesh. Additionally, the worst case errors were lower for the LS on the coarse mesh. These results also show that the FS on the coarse mesh is not sufficient, with significantly worse eigenvalue and pin-power comparisons.

[ADD TABLE OF TIME (per iter?) / MEMORY][MAKE NOTE OF ITERATION NUMBERS]

5.3.4.1 Coarse Rays

In each of the these lattice calculations, the MoC calculation takes up the majority of the runtime. The MoC runtime is directly proportional to the number of track-segments that are generated during the ray-tracing. This number is reduced as the mesh becomes coarser; however, due to material and geometric limitations, the mesh can only be coarsened so much. Another parameter that affects the number of track-segments is the ray-spacing, or how far apart each ray is. The rays can be spaced more coarsely, but this may cause some regions to not be integrated as accurately, thus degrading overall accuracy.

In this section, the use of coarser ray-spacing is investigated for the VERA problem 2 series. Results were generated using a ray-spacing of 0.1 cm and 0.2 cm for the default mesh with the FS

Table 5.5: Results for VERA Problem 2 lattices for different mesh and source approximations and coarse ray-spacings.

Case	Δk_{eff} (pcm)				Max Pin Power Difference (%)			
	FS (0.1 cm)	FS (0.2 cm)	LS (0.1 cm)	LS (0.2cm)	FS (0.1 cm)	FS (0.2 cm)	LS (0.1 cm)	LS (0.2cm)
A	42	34	21	18	0.15	0.45	0.10	0.33
B	41	33	19	16	0.15	0.45	0.10	0.33
C	42	34	21	18	0.15	0.45	0.10	0.33
D	45	38	23	20	0.15	0.45	0.10	0.33
E	4	-59	25	-29	0.22	0.28	0.09	0.28
F	-22	-32	26	28	0.19	0.31	0.09	0.42
G	27	73	98	162	0.31	0.49	0.24	0.44
H	-37	71	59	180	0.35	0.52	0.24	0.51
I	54	45	25	22	0.16	0.47	0.10	0.32
J	-22	-31	26	28	0.19	0.31	0.08	0.42
K	-5	-15	37	38	0.20	0.33	0.10	0.43
L	-30	-171	70	-40	0.79	0.90	0.80	1.30
M	-140	-220	-43	-15	1.08	0.94	1.11	1.20
N	-95	-227	23	-103	0.91	0.85	0.98	0.98
O	4	-36	27	-21	0.25	0.62	0.14	0.43
P	-7	-35	39	-7	0.30	0.61	0.20	0.40
Q	43	35	22	19	0.15	0.46	0.11	0.32
AVG	39	70	36	45	0.34	0.52	0.28	0.52
MAX	140	227	98	180	1.08	0.94	1.11	1.30

solver, and for the coarse mesh with LS solver. Eigenvalue and pin power comparisons are shown in [].

[SHOW DIFFERENCE FROM PREVIOUS!? - i.e. show affect of ray-spacing]

5.3.5 Assembly with Feedback

5.3.6 Core Depletion with Feedback

[Rough outline: 1. P9 depletion and TH Feedback 2. Radial coupling affect? 3. Mesh is valid or no? w/o radial coupling? w/ radial coupling? 4. Mention coarse rays = NO because control rods]

5.4 Conclusions

[INSERT CONCLUSIONS HERE]

Bibliography

[1] Rodolfo M. Ferrer and Joel D. Rhodes. "A Linear Source Approximation Scheme for the Method of Characteristics". In: *Nuclear Science and Engineering* 182.2 (2016), pp. 151–165. ISSN: 0029-5639. DOI: 10.13182/NSE15-6.

[2] Andrew Fitzgerald and Brendan Kochunas. "Fast Exponential Function Approximations for the Method of Characteristics with Linear Source". In: *Transactions of the American Nuclear Society*. Orlando, USA, 2018, pp. 645–648.

[3] Andrew P Fitzgerald, Brendan Kochunas, and Thomas Downar. "Improved Formulation of the Method of Characteristics with Linear Source for 2D/1D and Multiphysics Calculations". In: *M&C*. Portland, OR, 2019, pp. 1093–1103.

[4] Akio Yamamoto, Yasunori Kitamura, and Yoshihiro Yamane. "Computational efficiencies of approximated exponential functions for transport calculations of the characteristics method". In: *Annals of Nuclear Energy* 31.9 (2004), pp. 1027–1037. DOI: 10.1016/j.anucene.2004.01.003.

[5] Brendan Matthew Kochunas. "A Hybrid Parallel Algorithm for the 3-D Method of Characteristics Solution of the Boltzmann Transport Equation on High Performance Compute Clusters". Doctoral. University of Michigan, 2013, pp. 1–194.

[6] Gilbert W. Stewart. "20. Lecture 20". In: *Afternotes on Numerical Analysis*. 1996, pp. 147–153. DOI: 10.1137/1.9781611971491.ch20.

[7] A. T. Godfrey. *VERA Core Physics Benchmark Progression Problem Specifications*. Tech. rep. 4. 2014, pp. 1–173. URL: https://www.casl.gov/sites/default/files/docs/CASL-U-2012-0131-004.pdf.

[8] Akio Yamamoto et al. "Non-Equidistant Ray Tracing for the Method of Characteristics". In: *M&C 2005* (2005), pp. 1–10.

[9] K Lassmann et al. "The radial distribution of plutonium in high burnup UO2 fuels". In: *Journal of Nuclear Materials* 208.3 (1994), pp. 223–231. ISSN: 00223115. DOI: 10.1016/0022-3115(94)90331-X.

CHAPTER 6

MacroRay Three-Dimensional Ray-tracing Technique

6.1 Macroray

The *macroray* method is a three-dimensional extension of the two-dimensional macroband method, and is a central contribution of this work. This method has been implemented as part of this work, and, to the best of the author's knowledge, has never been studied. The macroray is a extension of the macroband into three-dimensions, in which along each radial ray the macroband method is used to generate axial rays on the characteristic plane. This follows the general procedure used for three-dimensional ray-tracing, but a limitation of this approach is explained in more detail in Section 3.4.3.1. In three-dimensions, rays can more generally be separated into "parallel pipes", to simplify notation these are referred to as macrorays.

The motivation for investigating this method is for three primary reasons. The first, is that 2-D results [1–3] have indicated that the macroband method allows for coarser ray-spacing (thus fewer rays) while maintaining accuracy. This is expected to increase computational efficiency, and lead to faster MoC calculations. However, an extension to three-dimensions, if coarser ray-spacing can be used in both the axial and radial directions, the increase in computational efficiency is expected to be greater.

Second, MRT methods require adjustments to the directional quadrature, which is expected to decrease accuracy of numerical integrals over directions [4]. The macroband and macroray methods require no such adjustment. Typically, it is the polar angle that has a more advanced quadrature (Gauss-Legendre, or Tabuchi-Yamamoto [5]), and is thus more sensitive to perturbations than the azimuthal angles. Without the perturbation of the polar (and azimuthal) quadratures, it may be possible to maintain accuracy while using fewer directions than is possible with 3-D MRT methods.

Finally, MRT methods require that the same ray-spacing parameters are used throughout the entire problem domain. Problems which have strong absorbers typically require a very fine mesh [6], which then requires that finer ray-spacing be used. This finer ray-spacing, which may only be

required for a small percentage of the problem domain, is then used for the entire domain, leading to a significant increase in the number tracks. The macroband and macroray methods allow for use of different ray-spacing parameters in each subsystem; additionally, because macrobands are based on the computational mesh, an effectively finer ray-spacing will automatically be generated due to the fine spatial mesh. This allows for densely spaced tracks where they are necessary, but more coarsely spaced tracks where they are not; this is expected to lead to significant reduction in the number of tracks in such problems.

Another consideration in three-dimensional locally axial extruded geometries is the chord-classification method. In the macroray method, rays are separated into the macrorays, which are guaranteed to be of the same class in the chord-classification method; this macroray classification is depicted in Fig. 6.1

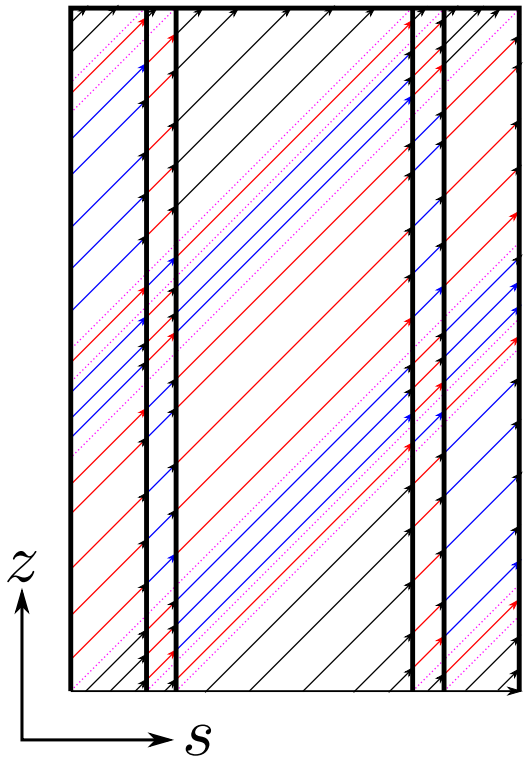

Figure 6.1: 3-D example of chord-classification with Macroray ray-tracing. Colored (red and blue) characteristic tracks represent groups of “V-chords”, rays between two vertical surfaces.

Bibliography

[1] Akio Yamamoto et al. “Non-Equidistant Ray Tracing for the Method of Characteristics”. In: *M&C 2005* (2005), pp. 1–10.

[2] François Févotte, Simone Santandrea, and Richard Sanchez. “Advanced Transverse Integration for the Method of Characteristics”. In: *M&C 2007*. 2007, pp. 1–12. ISBN: 0894480596.

[3] Akio Yamamoto. “Reduction in spatial discretization error in the method of characteristics by using the mobile-chord ray tracing method”. In: *Annals of Nuclear Energy* 35.5 (2008), pp. 783–789. ISSN: 03064549. DOI: 10.1016/j.anucene.2007.09.018.

[4] Brendan Matthew Kochunas. “A Hybrid Parallel Algorithm for the 3-D Method of Characteristics Solution of the Boltzmann Transport Equation on High Performance Compute Clusters”. Doctoral. University of Michigan, 2013, pp. 1–194.

[5] Akio Yamamoto et al. “Derivation of optimum polar angle quadrature set for the method of characteristics based on approximation error for the bickley function”. In: *Journal of Nuclear Science and Technology* 44.2 (2007), pp. 129–136. ISSN: 00223131. DOI: 10.1080/18811248.2007.9711266.

[6] Andrew P Fitzgerald, Brendan Kochunas, and Thomas Downar. “Improved Formulation of the Method of Characteristics with Linear Source for 2D/1D and Multiphysics Calculations”. In: *M&C*. Portland, OR, 2019, pp. 1093–1103.

CHAPTER 7

Results (Final)

Lorem ipsum dolor sit amet, consectetuer adipiscing elit. Etiam lobortis facilisis sem. Nullam nec mi et neque pharetra sollicitudin. Praesent imperdiet mi nec ante. Donec ullamcorper, felis non sodales commodo, lectus velit ultrices augue, a dignissim nibh lectus placerat pede. Vivamus nunc nunc, molestie ut, ultricies vel, semper in, velit. Ut porttitor. Praesent in sapien. Lorem ipsum dolor sit amet, consectetuer adipiscing elit. Duis fringilla tristique neque. Sed interdum libero ut metus. Pellentesque placerat. Nam rutrum augue a leo. Morbi sed elit sit amet ante lobortis sollicitudin. Praesent blandit blandit mauris. Praesent lectus tellus, aliquet aliquam, luctus a, egestas a, turpis. Mauris lacinia lorem sit amet ipsum. Nunc quis urna dictum turpis accumsan semper. Lorem ipsum dolor sit amet, consectetuer adipiscing elit. Etiam lobortis facilisis sem. Nullam nec mi et neque pharetra sollicitudin. Praesent imperdiet mi nec ante. Donec ullamcorper, felis non sodales commodo, lectus velit ultrices augue, a dignissim nibh lectus placerat pede. Vivamus nunc nunc, molestie ut, ultricies vel, semper in, velit. Ut porttitor. Praesent in sapien. Lorem ipsum dolor sit amet, consectetuer adipiscing elit. Duis fringilla tristique neque. Sed interdum libero ut metus. Pellentesque placerat. Nam rutrum augue a leo. Morbi sed elit sit amet ante lobortis sollicitudin. Praesent blandit blandit mauris. Praesent lectus tellus, aliquet aliquam, luctus a, egestas a, turpis. Mauris lacinia lorem sit amet ipsum. Nunc quis urna dictum turpis accumsan semper. Lorem ipsum dolor sit amet, consectetuer adipiscing elit. Etiam lobortis facilisis sem. Nullam nec mi et neque pharetra sollicitudin. Praesent imperdiet mi nec ante. Donec ullamcorper, felis non sodales commodo, lectus velit ultrices augue, a dignissim nibh lectus placerat pede. Vivamus nunc nunc, molestie ut, ultricies vel, semper in, velit. Ut porttitor. Praesent in sapien. Lorem ipsum dolor sit amet, consectetuer adipiscing elit. Duis fringilla tristique neque. Sed interdum libero ut metus. Pellentesque placerat. Nam rutrum augue a leo. Morbi sed elit sit amet ante lobortis sollicitudin. Praesent blandit blandit mauris. Praesent lectus tellus, aliquet aliquam, luctus a, egestas a, turpis. Mauris lacinia lorem sit amet ipsum. Nunc quis urna dictum turpis accumsan semper. Lorem ipsum dolor sit amet, consectetuer adipiscing elit. Etiam lobortis facilisis sem. Nullam nec mi et neque pharetra sollicitudin. Praesent imperdiet mi nec ante. Donec ullamcorper, felis non sodales commodo, lectus velit ultrices augue, a dignissim nibh lectus placerat pede. Vivamus nunc

nunc, molestie ut, ultricies vel, semper in, velit. Ut porttitor. Praesent in sapien. Lorem ipsum dolor sit amet, consectetuer adipiscing elit. Duis fringilla tristique neque. Sed interdum libero ut metus. Pellentesque placerat. Nam rutrum augue a leo. Morbi sed elit sit amet ante lobortis sollicitudin. Praesent blandit blandit mauris. Praesent lectus tellus, aliquet aliquam, luctus a, egestas a, turpis. Mauris lacinia lorem sit amet ipsum. Nunc quis urna dictum turpis accumsan semper. Lorem ipsum dolor sit amet, consectetuer adipiscing elit. Etiam lobortis facilisis sem. Nullam nec mi et neque pharetra sollicitudin. Praesent imperdiet mi nec ante. Donec ullamcorper, felis non sodales commodo, lectus velit ultrices augue, a dignissim nibh lectus placerat pede. Vivamus nunc nunc, molestie ut, ultricies vel, semper in, velit. Ut porttitor. Praesent in sapien. Lorem ipsum dolor sit amet, consectetuer adipiscing elit. Duis fringilla tristique neque. Sed interdum libero ut metus. Pellentesque placerat. Nam rutrum augue a leo. Morbi sed elit sit amet ante lobortis sollicitudin. Praesent blandit blandit mauris. Praesent lectus tellus, aliquet aliquam, luctus a, egestas a, turpis. Mauris lacinia lorem sit amet ipsum. Nunc quis urna dictum turpis accumsan semper. Lorem ipsum dolor sit amet, consectetuer adipiscing elit. Etiam lobortis facilisis sem. Nullam nec mi et neque pharetra sollicitudin. Praesent imperdiet mi nec ante. Donec ullamcorper, felis non sodales commodo, lectus velit ultrices augue, a dignissim nibh lectus placerat pede. Vivamus nunc nunc, molestie ut, ultricies vel, semper in, velit. Ut porttitor. Praesent in sapien. Lorem ipsum dolor sit amet, consectetuer adipiscing elit. Duis fringilla tristique neque. Sed interdum libero ut metus. Pellentesque placerat. Nam rutrum augue a leo. Morbi sed elit sit amet ante lobortis sollicitudin. Praesent blandit blandit mauris. Praesent lectus tellus, aliquet aliquam, luctus a, egestas a, turpis. Mauris lacinia lorem sit amet ipsum. Nunc quis urna dictum turpis accumsan semper. Lorem ipsum dolor sit amet, consectetuer adipiscing elit. Etiam lobortis facilisis sem. Nullam nec mi et neque pharetra sollicitudin. Praesent imperdiet mi nec ante. Donec ullamcorper, felis non sodales commodo, lectus velit ultrices augue, a dignissim nibh lectus placerat pede. Vivamus nunc nunc, molestie ut, ultricies vel, semper in, velit. Ut porttitor. Praesent in sapien. Lorem ipsum dolor sit amet, consectetuer adipiscing elit. Duis fringilla tristique neque. Sed interdum libero ut metus. Pellentesque placerat. Nam rutrum augue a leo. Morbi sed elit sit amet ante lobortis sollicitudin. Praesent blandit blandit mauris. Praesent lectus tellus, aliquet aliquam, luctus a, egestas a, turpis. Mauris lacinia lorem sit amet ipsum. Nunc quis urna dictum turpis accumsan semper. Lorem ipsum dolor sit amet, consectetuer adipiscing elit. Etiam lobortis facilisis sem. Nullam nec mi et neque pharetra sollicitudin. Praesent imperdiet mi nec ante. Donec ullamcorper, felis non sodales commodo, lectus velit ultrices augue, a dignissim nibh lectus placerat pede. Vivamus nunc nunc, molestie ut, ultricies vel, semper in, velit. Ut porttitor. Praesent in sapien. Lorem ipsum dolor sit amet, consectetuer adipiscing elit. Duis fringilla tristique neque. Sed interdum libero ut metus. Pellentesque placerat. Nam rutrum augue a leo. Morbi sed elit sit amet ante lobortis sollicitudin. Praesent blandit blandit mauris. Praesent lectus tellus, aliquet aliquam, luctus a, egestas

a, turpis. Mauris lacinia lorem sit amet ipsum. Nunc quis urna dictum turpis accumsan semper. Lorem ipsum dolor sit amet, consectetuer adipiscing elit. Etiam lobortis facilisis sem. Nullam nec mi et neque pharetra sollicitudin. Praesent imperdiet mi nec ante. Donec ullamcorper, felis non sodales commodo, lectus velit ultrices augue, a dignissim nibh lectus placerat pede. Vivamus nunc nunc, molestie ut, ultricies vel, semper in, velit. Ut porttitor. Praesent in sapien. Lorem ipsum dolor sit amet, consectetuer adipiscing elit. Duis fringilla tristique neque. Sed interdum libero ut metus. Pellentesque placerat. Nam rutrum augue a leo. Morbi sed elit sit amet ante lobortis sollicitudin. Praesent blandit blandit mauris. Praesent lectus tellus, aliquet aliquam, luctus a, egestas a, turpis. Mauris lacinia lorem sit amet ipsum. Nunc quis urna dictum turpis accumsan semper. Lorem ipsum dolor sit amet, consectetuer adipiscing elit. Etiam lobortis facilisis sem. Nullam nec mi et neque pharetra sollicitudin. Praesent imperdiet mi nec ante. Donec ullamcorper, felis non sodales commodo, lectus velit ultrices augue, a dignissim nibh lectus placerat pede. Vivamus nunc nunc, molestie ut, ultricies vel, semper in, velit. Ut porttitor. Praesent in sapien. Lorem ipsum dolor sit amet, consectetuer adipiscing elit. Duis fringilla tristique neque. Sed interdum libero ut metus. Pellentesque placerat. Nam rutrum augue a leo. Morbi sed elit sit amet ante lobortis sollicitudin. Praesent blandit blandit mauris. Praesent lectus tellus, aliquet aliquam, luctus a, egestas a, turpis. Mauris lacinia lorem sit amet ipsum. Nunc quis urna dictum turpis accumsan semper. Lorem ipsum dolor sit amet, consectetuer adipiscing elit. Etiam lobortis facilisis sem. Nullam nec mi et neque pharetra sollicitudin. Praesent imperdiet mi nec ante. Donec ullamcorper, felis non sodales commodo, lectus velit ultrices augue, a dignissim nibh lectus placerat pede. Vivamus nunc nunc, molestie ut, ultricies vel, semper in, velit. Ut porttitor. Praesent in sapien. Lorem ipsum dolor sit amet, consectetuer adipiscing elit. Duis fringilla tristique neque. Sed interdum libero ut metus. Pellentesque placerat. Nam rutrum augue a leo. Morbi sed elit sit amet ante lobortis sollicitudin. Praesent blandit blandit mauris. Praesent lectus tellus, aliquet aliquam, luctus a, egestas a, turpis. Mauris lacinia lorem sit amet ipsum. Nunc quis urna dictum turpis accumsan semper. Lorem ipsum dolor sit amet, consectetuer adipiscing elit. Etiam lobortis facilisis sem. Nullam nec mi et neque pharetra sollicitudin. Praesent imperdiet mi nec ante. Donec ullamcorper, felis non sodales commodo, lectus velit ultrices augue, a dignissim nibh lectus placerat pede. Vivamus nunc nunc, molestie ut, ultricies vel, semper in, velit. Ut porttitor. Praesent in sapien. Lorem ipsum dolor sit amet, consectetuer adipiscing elit. Duis fringilla tristique neque. Sed interdum libero ut metus. Pellentesque placerat. Nam rutrum augue a leo. Morbi sed elit sit amet ante lobortis sollicitudin. Praesent blandit blandit mauris. Praesent lectus tellus, aliquet aliquam, luctus a, egestas a, turpis. Mauris lacinia lorem sit amet ipsum. Nunc quis urna dictum turpis accumsan semper. Lorem ipsum dolor sit amet, consectetuer adipiscing elit. Etiam lobortis facilisis sem. Nullam nec mi et neque pharetra sollicitudin. Praesent imperdiet mi nec ante. Donec ullamcorper, felis non sodales commodo, lectus velit ultrices augue, a dignissim nibh lectus placerat pede. Vivamus nunc

nunc, molestie ut, ultricies vel, semper in, velit. Ut porttitor. Praesent in sapien. Lorem ipsum dolor sit amet, consectetuer adipiscing elit. Duis fringilla tristique neque. Sed interdum libero ut metus. Pellentesque placerat. Nam rutrum augue a leo. Morbi sed elit sit amet ante lobortis sollicitudin. Praesent blandit blandit mauris. Praesent lectus tellus, aliquet aliquam, luctus a, egestas a, turpis. Mauris lacinia lorem sit amet ipsum. Nunc quis urna dictum turpis accumsan semper. Lorem ipsum dolor sit amet, consectetuer adipiscing elit. Etiam lobortis facilisis sem. Nullam nec mi et neque pharetra sollicitudin. Praesent imperdiet mi nec ante. Donec ullamcorper, felis non sodales commodo, lectus velit ultrices augue, a dignissim nibh lectus placerat pede. Vivamus nunc nunc, molestie ut, ultricies vel, semper in, velit. Ut porttitor. Praesent in sapien. Lorem ipsum dolor sit amet, consectetuer adipiscing elit. Duis fringilla tristique neque. Sed interdum libero ut metus. Pellentesque placerat. Nam rutrum augue a leo. Morbi sed elit sit amet ante lobortis sollicitudin. Praesent blandit blandit mauris. Praesent lectus tellus, aliquet aliquam, luctus a, egestas a, turpis. Mauris lacinia lorem sit amet ipsum. Nunc quis urna dictum turpis accumsan semper. Lorem ipsum dolor sit amet, consectetuer adipiscing elit. Etiam lobortis facilisis sem. Nullam nec mi et neque pharetra sollicitudin. Praesent imperdiet mi nec ante. Donec ullamcorper, felis non sodales commodo, lectus velit ultrices augue, a dignissim nibh lectus placerat pede. Vivamus nunc nunc, molestie ut, ultricies vel, semper in, velit. Ut porttitor. Praesent in sapien. Lorem ipsum dolor sit amet, consectetuer adipiscing elit. Duis fringilla tristique neque. Sed interdum libero ut metus. Pellentesque placerat. Nam rutrum augue a leo. Morbi sed elit sit amet ante lobortis sollicitudin. Praesent blandit blandit mauris. Praesent lectus tellus, aliquet aliquam, luctus a, egestas a, turpis. Mauris lacinia lorem sit amet ipsum. Nunc quis urna dictum turpis accumsan semper. Lorem ipsum dolor sit amet, consectetuer adipiscing elit. Etiam lobortis facilisis sem. Nullam nec mi et neque pharetra sollicitudin. Praesent imperdiet mi nec ante. Donec ullamcorper, felis non sodales commodo, lectus velit ultrices augue, a dignissim nibh lectus placerat pede. Vivamus nunc nunc, molestie ut, ultricies vel, semper in, velit. Ut porttitor. Praesent in sapien. Lorem ipsum dolor sit amet, consectetuer adipiscing elit. Duis fringilla tristique neque. Sed interdum libero ut metus. Pellentesque placerat. Nam rutrum augue a leo. Morbi sed elit sit amet ante lobortis sollicitudin. Praesent blandit blandit mauris. Praesent lectus tellus, aliquet aliquam, luctus a, egestas a, turpis. Mauris lacinia lorem sit amet ipsum. Nunc quis urna dictum turpis accumsan semper.

CHAPTER 8

Conclusions

Lorem ipsum dolor sit amet, consectetuer adipiscing elit. Etiam lobortis facilisis sem. Nullam nec mi et neque pharetra sollicitudin. Praesent imperdiet mi nec ante. Donec ullamcorper, felis non sodales commodo, lectus velit ultrices augue, a dignissim nibh lectus placerat pede. Vivamus nunc nunc, molestie ut, ultricies vel, semper in, velit. Ut porttitor. Praesent in sapien. Lorem ipsum dolor sit amet, consectetuer adipiscing elit. Duis fringilla tristique neque. Sed interdum libero ut metus. Pellentesque placerat. Nam rutrum augue a leo. Morbi sed elit sit amet ante lobortis sollicitudin. Praesent blandit blandit mauris. Praesent lectus tellus, aliquet aliquam, luctus a, egestas a, turpis. Mauris lacinia lorem sit amet ipsum. Nunc quis urna dictum turpis accumsan semper. Lorem ipsum dolor sit amet, consectetuer adipiscing elit. Etiam lobortis facilisis sem. Nullam nec mi et neque pharetra sollicitudin. Praesent imperdiet mi nec ante. Donec ullamcorper, felis non sodales commodo, lectus velit ultrices augue, a dignissim nibh lectus placerat pede. Vivamus nunc nunc, molestie ut, ultricies vel, semper in, velit. Ut porttitor. Praesent in sapien. Lorem ipsum dolor sit amet, consectetuer adipiscing elit. Duis fringilla tristique neque. Sed interdum libero ut metus. Pellentesque placerat. Nam rutrum augue a leo. Morbi sed elit sit amet ante lobortis sollicitudin. Praesent blandit blandit mauris. Praesent lectus tellus, aliquet aliquam, luctus a, egestas a, turpis. Mauris lacinia lorem sit amet ipsum. Nunc quis urna dictum turpis accumsan semper. Lorem ipsum dolor sit amet, consectetuer adipiscing elit. Etiam lobortis facilisis sem. Nullam nec mi et neque pharetra sollicitudin. Praesent imperdiet mi nec ante. Donec ullamcorper, felis non sodales commodo, lectus velit ultrices augue, a dignissim nibh lectus placerat pede. Vivamus nunc nunc, molestie ut, ultricies vel, semper in, velit. Ut porttitor. Praesent in sapien. Lorem ipsum dolor sit amet, consectetuer adipiscing elit. Duis fringilla tristique neque. Sed interdum libero ut metus. Pellentesque placerat. Nam rutrum augue a leo. Morbi sed elit sit amet ante lobortis sollicitudin. Praesent blandit blandit mauris. Praesent lectus tellus, aliquet aliquam, luctus a, egestas a, turpis. Mauris lacinia lorem sit amet ipsum. Nunc quis urna dictum turpis accumsan semper. Lorem ipsum dolor sit amet, consectetuer adipiscing elit. Etiam lobortis facilisis sem. Nullam nec mi et neque pharetra sollicitudin. Praesent imperdiet mi nec ante. Donec ullamcorper, felis non sodales commodo, lectus velit ultrices augue, a dignissim nibh lectus placerat pede. Vivamus nunc

nunc, molestie ut, ultricies vel, semper in, velit. Ut porttitor. Praesent in sapien. Lorem ipsum dolor sit amet, consectetuer adipiscing elit. Duis fringilla tristique neque. Sed interdum libero ut metus. Pellentesque placerat. Nam rutrum augue a leo. Morbi sed elit sit amet ante lobortis sollicitudin. Praesent blandit blandit mauris. Praesent lectus tellus, aliquet aliquam, luctus a, egestas a, turpis. Mauris lacinia lorem sit amet ipsum. Nunc quis urna dictum turpis accumsan semper. Lorem ipsum dolor sit amet, consectetuer adipiscing elit. Etiam lobortis facilisis sem. Nullam nec mi et neque pharetra sollicitudin. Praesent imperdiet mi nec ante. Donec ullamcorper, felis non sodales commodo, lectus velit ultrices augue, a dignissim nibh lectus placerat pede. Vivamus nunc nunc, molestie ut, ultricies vel, semper in, velit. Ut porttitor. Praesent in sapien. Lorem ipsum dolor sit amet, consectetuer adipiscing elit. Duis fringilla tristique neque. Sed interdum libero ut metus. Pellentesque placerat. Nam rutrum augue a leo. Morbi sed elit sit amet ante lobortis sollicitudin. Praesent blandit blandit mauris. Praesent lectus tellus, aliquet aliquam, luctus a, egestas a, turpis. Mauris lacinia lorem sit amet ipsum. Nunc quis urna dictum turpis accumsan semper. Lorem ipsum dolor sit amet, consectetuer adipiscing elit. Etiam lobortis facilisis sem. Nullam nec mi et neque pharetra sollicitudin. Praesent imperdiet mi nec ante. Donec ullamcorper, felis non sodales commodo, lectus velit ultrices augue, a dignissim nibh lectus placerat pede. Vivamus nunc nunc, molestie ut, ultricies vel, semper in, velit. Ut porttitor. Praesent in sapien. Lorem ipsum dolor sit amet, consectetuer adipiscing elit. Duis fringilla tristique neque. Sed interdum libero ut metus. Pellentesque placerat. Nam rutrum augue a leo. Morbi sed elit sit amet ante lobortis sollicitudin. Praesent blandit blandit mauris. Praesent lectus tellus, aliquet aliquam, luctus a, egestas a, turpis. Mauris lacinia lorem sit amet ipsum. Nunc quis urna dictum turpis accumsan semper. Lorem ipsum dolor sit amet, consectetuer adipiscing elit. Etiam lobortis facilisis sem. Nullam nec mi et neque pharetra sollicitudin. Praesent imperdiet mi nec ante. Donec ullamcorper, felis non sodales commodo, lectus velit ultrices augue, a dignissim nibh lectus placerat pede. Vivamus nunc nunc, molestie ut, ultricies vel, semper in, velit. Ut porttitor. Praesent in sapien. Lorem ipsum dolor sit amet, consectetuer adipiscing elit. Duis fringilla tristique neque. Sed interdum libero ut metus. Pellentesque placerat. Nam rutrum augue a leo. Morbi sed elit sit amet ante lobortis sollicitudin. Praesent blandit blandit mauris. Praesent lectus tellus, aliquet aliquam, luctus a, egestas a, turpis. Mauris lacinia lorem sit amet ipsum. Nunc quis urna dictum turpis accumsan semper. Lorem ipsum dolor sit amet, consectetuer adipiscing elit. Etiam lobortis facilisis sem. Nullam nec mi et neque pharetra sollicitudin. Praesent imperdiet mi nec ante. Donec ullamcorper, felis non sodales commodo, lectus velit ultrices augue, a dignissim nibh lectus placerat pede. Vivamus nunc nunc, molestie ut, ultricies vel, semper in, velit. Ut porttitor. Praesent in sapien. Lorem ipsum dolor sit amet, consectetuer adipiscing elit. Duis fringilla tristique neque. Sed interdum libero ut metus. Pellentesque placerat. Nam rutrum augue a leo. Morbi sed elit sit amet ante lobortis sollicitudin. Praesent blandit blandit mauris. Praesent lectus tellus, aliquet aliquam, luctus a, egestas

a, turpis. Mauris lacinia lorem sit amet ipsum. Nunc quis urna dictum turpis accumsan semper. Lorem ipsum dolor sit amet, consectetuer adipiscing elit. Etiam lobortis facilisis sem. Nullam nec mi et neque pharetra sollicitudin. Praesent imperdiet mi nec ante. Donec ullamcorper, felis non sodales commodo, lectus velit ultrices augue, a dignissim nibh lectus placerat pede. Vivamus nunc nunc, molestie ut, ultricies vel, semper in, velit. Ut porttitor. Praesent in sapien. Lorem ipsum dolor sit amet, consectetuer adipiscing elit. Duis fringilla tristique neque. Sed interdum libero ut metus. Pellentesque placerat. Nam rutrum augue a leo. Morbi sed elit sit amet ante lobortis sollicitudin. Praesent blandit blandit mauris. Praesent lectus tellus, aliquet aliquam, luctus a, egestas a, turpis. Mauris lacinia lorem sit amet ipsum. Nunc quis urna dictum turpis accumsan semper. Lorem ipsum dolor sit amet, consectetuer adipiscing elit. Etiam lobortis facilisis sem. Nullam nec mi et neque pharetra sollicitudin. Praesent imperdiet mi nec ante. Donec ullamcorper, felis non sodales commodo, lectus velit ultrices augue, a dignissim nibh lectus placerat pede. Vivamus nunc nunc, molestie ut, ultricies vel, semper in, velit. Ut porttitor. Praesent in sapien. Lorem ipsum dolor sit amet, consectetuer adipiscing elit. Duis fringilla tristique neque. Sed interdum libero ut metus. Pellentesque placerat. Nam rutrum augue a leo. Morbi sed elit sit amet ante lobortis sollicitudin. Praesent blandit blandit mauris. Praesent lectus tellus, aliquet aliquam, luctus a, egestas a, turpis. Mauris lacinia lorem sit amet ipsum. Nunc quis urna dictum turpis accumsan semper. Lorem ipsum dolor sit amet, consectetuer adipiscing elit. Etiam lobortis facilisis sem. Nullam nec mi et neque pharetra sollicitudin. Praesent imperdiet mi nec ante. Donec ullamcorper, felis non sodales commodo, lectus velit ultrices augue, a dignissim nibh lectus placerat pede. Vivamus nunc nunc, molestie ut, ultricies vel, semper in, velit. Ut porttitor. Praesent in sapien. Lorem ipsum dolor sit amet, consectetuer adipiscing elit. Duis fringilla tristique neque. Sed interdum libero ut metus. Pellentesque placerat. Nam rutrum augue a leo. Morbi sed elit sit amet ante lobortis sollicitudin. Praesent blandit blandit mauris. Praesent lectus tellus, aliquet aliquam, luctus a, egestas a, turpis. Mauris lacinia lorem sit amet ipsum. Nunc quis urna dictum turpis accumsan semper. Lorem ipsum dolor sit amet, consectetuer adipiscing elit. Etiam lobortis facilisis sem. Nullam nec mi et neque pharetra sollicitudin. Praesent imperdiet mi nec ante. Donec ullamcorper, felis non sodales commodo, lectus velit ultrices augue, a dignissim nibh lectus placerat pede. Vivamus nunc nunc, molestie ut, ultricies vel, semper in, velit. Ut porttitor. Praesent in sapien. Lorem ipsum dolor sit amet, consectetuer adipiscing elit. Duis fringilla tristique neque. Sed interdum libero ut metus. Pellentesque placerat. Nam rutrum augue a leo. Morbi sed elit sit amet ante lobortis sollicitudin. Praesent blandit blandit mauris. Praesent lectus tellus, aliquet aliquam, luctus a, egestas a, turpis. Mauris lacinia lorem sit amet ipsum. Nunc quis urna dictum turpis accumsan semper. Lorem ipsum dolor sit amet, consectetuer adipiscing elit. Etiam lobortis facilisis sem. Nullam nec mi et neque pharetra sollicitudin. Praesent imperdiet mi nec ante. Donec ullamcorper, felis non sodales commodo, lectus velit ultrices augue, a dignissim nibh lectus placerat pede. Vivamus nunc

nunc, molestie ut, ultricies vel, semper in, velit. Ut porttitor. Praesent in sapien. Lorem ipsum dolor sit amet, consectetuer adipiscing elit. Duis fringilla tristique neque. Sed interdum libero ut metus. Pellentesque placerat. Nam rutrum augue a leo. Morbi sed elit sit amet ante lobortis sollicitudin. Praesent blandit blandit mauris. Praesent lectus tellus, aliquet aliquam, luctus a, egestas a, turpis. Mauris lacinia lorem sit amet ipsum. Nunc quis urna dictum turpis accumsan semper. Lorem ipsum dolor sit amet, consectetuer adipiscing elit. Etiam lobortis facilisis sem. Nullam nec mi et neque pharetra sollicitudin. Praesent imperdiet mi nec ante. Donec ullamcorper, felis non sodales commodo, lectus velit ultrices augue, a dignissim nibh lectus placerat pede. Vivamus nunc nunc, molestie ut, ultricies vel, semper in, velit. Ut porttitor. Praesent in sapien. Lorem ipsum dolor sit amet, consectetuer adipiscing elit. Duis fringilla tristique neque. Sed interdum libero ut metus. Pellentesque placerat. Nam rutrum augue a leo. Morbi sed elit sit amet ante lobortis sollicitudin. Praesent blandit blandit mauris. Praesent lectus tellus, aliquet aliquam, luctus a, egestas a, turpis. Mauris lacinia lorem sit amet ipsum. Nunc quis urna dictum turpis accumsan semper. Lorem ipsum dolor sit amet, consectetuer adipiscing elit. Etiam lobortis facilisis sem. Nullam nec mi et neque pharetra sollicitudin. Praesent imperdiet mi nec ante. Donec ullamcorper, felis non sodales commodo, lectus velit ultrices augue, a dignissim nibh lectus placerat pede. Vivamus nunc nunc, molestie ut, ultricies vel, semper in, velit. Ut porttitor. Praesent in sapien. Lorem ipsum dolor sit amet, consectetuer adipiscing elit. Duis fringilla tristique neque. Sed interdum libero ut metus. Pellentesque placerat. Nam rutrum augue a leo. Morbi sed elit sit amet ante lobortis sollicitudin. Praesent blandit blandit mauris. Praesent lectus tellus, aliquet aliquam, luctus a, egestas a, turpis. Mauris lacinia lorem sit amet ipsum. Nunc quis urna dictum turpis accumsan semper. Lorem ipsum dolor sit amet, consectetuer adipiscing elit. Etiam lobortis facilisis sem. Nullam nec mi et neque pharetra sollicitudin. Praesent imperdiet mi nec ante. Donec ullamcorper, felis non sodales commodo, lectus velit ultrices augue, a dignissim nibh lectus placerat pede. Vivamus nunc nunc, molestie ut, ultricies vel, semper in, velit. Ut porttitor. Praesent in sapien. Lorem ipsum dolor sit amet, consectetuer adipiscing elit. Duis fringilla tristique neque. Sed interdum libero ut metus. Pellentesque placerat. Nam rutrum augue a leo. Morbi sed elit sit amet ante lobortis sollicitudin. Praesent blandit blandit mauris. Praesent lectus tellus, aliquet aliquam, luctus a, egestas a, turpis. Mauris lacinia lorem sit amet ipsum. Nunc quis urna dictum turpis accumsan semper.